

## ABSTRACT

Title of Dissertation: HIGH POWER NONLINEAR PROPAGATION  
OF LASER PULSES IN TENUOUS GASES  
AND PLASMA CHANNELS

Jianzhou Wu, Doctor of Philosophy, 2005

Dissertation Directed By: Professor Thomas M. Antonsen, Jr.  
Department of Physics

The nonlinear propagation over long distances of moderate intensity laser pulses in tenuous gases is studied. The dynamics of these pulses will be affected by nonlinear focusing and dispersion due to the background gas, and by plasma induced refraction and dispersion. Laser propagation is studied numerically using the simulation code WAKE. Different phenomena are found for different regimes of peak input power. For powers near the critical power, temporal pulse narrowing and splitting due to phase modulation and group velocity dispersion is seen. For slightly higher powers, plasma generation and the formation of a trailing pulse, which is guided off axis by plasma refraction and nonlinear gas focusing, is observed. For even higher powers, the laser pulse is partially trapped by the plasma and then exhibits a form of self-interference.

The processes affecting the spectrum of the pulse is also studied. Among these are self-phase modulation, nonlinear self-focusing, plasma generation, and group velocity dispersion. The combination of these factors leads to an asymmetric

spectrum. If group velocity dispersion cannot arrest nonlinear self-focusing, self-phase modulation, coupled with nonlinear self-focusing, gives rise to a red shifted spectrum. In case plasma is generated, large blue shifted components are observed. The maximum blue shift is determined by both the maximum value of the electron density, and the distance over which the plasma extends.

Finally, the injection of laser pulses into hydrodynamically preformed plasma channels is investigated. The injection of laser pulses into hydrodynamically preformed plasma channels can be hindered by the conditions at the entrance of the channel. In particular, neutral gas and narrowing of the channel prevent efficient coupling of laser pulse entering into the channel. To solve this problem, a funnel shaped plasma lens can be grafted onto the channel using an auxiliary formation pulse. Simulations of channel formation show that such a funnel can be made in the density ramp of a gas jet. Simulations of laser pulse propagation show that such a funnel efficiently couples pulse energy into the channel. For a backfill target with a funnel, the coupling efficiency is lower and required funnel parameters are more restrictive than for the gas jet case.

# HIGH POWER NONLINEAR PROPAGATION OF LASER PULSES IN TENUOUS GASES AND PLASMA CHANNELS

By

Jianzhou Wu

Dissertation submitted to the Faculty of the Graduate School of the  
University of Maryland, College Park, in partial fulfillment  
of the requirements for the degree of  
Doctor of Philosophy  
2005

## Advisory Committee:

Professor Thomas M. Antonsen, Jr. Chair  
Professor Howard M. Milchberg  
Professor Julius Goldhar  
Professor Adil Hassam  
Professor Rajarshi Roy

© Copyright by  
Jianzhou Wu  
2005

## **Dedication**

To my wife, parents and in-laws.

## **Acknowledgements**

I would like to express my special gratitude to my advisor Dr. Thomas M. Antonsen, Jr., without his careful guidance, constant encouragement, and inexorable support, this dissertation work would not have been possible. I am also grateful to Dr. Howard M. Milchberg for giving me valuable knowledge and discussions of my research and the experiments. I would also like to thank Dr. Julius Goldhar, Dr. Edward Ott, and Dr. Rajarshi Roy for serving on my dissertation committee.

During my years at the University of Maryland I was very fortunate to have received invaluable assistance and discussion from many talented friends and fellow students, especially, Dr. Zhigang Bian, Dr. James H. Cooley, Mr. Ayush Gupta, and the graduate students from Dr. Howard M. Milchberg's laboratory.

My greatest gratitude shall always go to my parents and in-laws for their continuous love, encouragement, and support of my education. I am definitely grateful to my lovely wife for her understanding and patience during the past few years. Her invaluable encouragement and help was the true support behind everything.

# Table of Contents

Dedication.....	ii
Acknowledgements.....	iii
Table of Contents.....	iv
List of Tables .....	vi
List of Figures.....	vii
Chapter 1: Introduction.....	1
1.1 Overview.....	1
1.2 Purpose of the Dissertation.....	7
1.3 Organization of the Dissertation.....	10
Chapter 2: Laser Pulse Splitting and Trapping in Tenuous Gases.....	11
2.1 Introduction.....	11
2.2 Model.....	14
2.3 Numerical Simulation.....	23
2.3.1 Phenomena corresponding to various input powers.....	25
2.3.1.1 Pulse splitting in the critical power regime.....	26
2.3.1.2 Transient ionization.....	30
2.3.1.3 Off axis guiding in the slightly higher power regime.....	32
2.3.1.4 Outgoing waves in the much higher power regime.....	34
2.3.2 Time delayed Raman response.....	36
2.4 Chapter Summary.....	39
Chapter 3: Spectrum Broadening of Laser Pulses Propagating in Tenuous Gases.....	59

3.1 Introduction.....	59
3.2 Theoretical Model.....	62
3.3 Nonlinearity Induced Red Shift .....	65
3.4 Plasma Induced Blue Shift.....	69
3.5 Chapter Summary .....	71
Chapter 4: Effective coupling of ultra-intense laser pulse to funnel-mouthed plasma waveguides.....	86
4.1 Introduction.....	86
4.2 Laser Parameters And Funnel-Mouthed Channel Profiles .....	89
4.3 Gas Jet Target .....	94
4.4 Backfill Target .....	99
4.5 Chapter Summary .....	102
Chapter 5: Conclusion.....	121
Bibliography: .....	124
Chapter 1:.....	124
Chapter 2:.....	128
Chapter 3:.....	130
Chapter 4:.....	131



## List of Tables

Table 2.1: Critical intensities for ionization and critical powers for self-focusing.....	40
---	----

## List of Figures

- Figure 2.1: Time evolution of the normalized laser intensity. The peak input power  $P_{\max} = 1.14 \times 10^{11}$  W, spot size  $r_0 = 0.21$  cm, and pulse length  $Z_L = 135$  cm. .... 41
- Figure 2.2: Plots of the on axis intensity as function of  $\xi$  for the case of Fig. 2.1. .... 42
- Figure 2.3: Distribution of the radially integrated power for the case of Fig. 2.1. .... 43
- Figure 2.4: Plots of the peak intensity on axis, normalized to the initial peak intensity, as a function of normalized time  $t/T_R$  for various initial parameters. The peak input powers associated with the solid, dashed, and dotted lines are  $1.14 \times 10^{11}$  W,  $1.322 \times 10^{11}$  W, and  $1.057 \times 10^{11}$  W respectively. The normalized coefficient,  $\beta_N$ , for the solid lines with diamond, circle, square, and triangle, are 0.011, 0.014, 0.017 and 0.021, for the dashed lines with the same marks in order, are 0.074, 0.084, 0.112 and 0.126, and for the dotted lines in the same order, are  $8.76 \times 10^{-4}$ ,  $1.17 \times 10^{-3}$ ,  $1.56 \times 10^{-3}$  and  $2.0 \times 10^{-3}$  respectively..... 44
- Figure 2.5: Plots of the axial intensity versus  $\xi$  at the given time. The peak input power  $P_{\max}$ , normalized coefficient  $\beta_N$ , and normalized time  $t/T_R$ , are  $1.14 \times 10^{11}$ , 0.011, and 3.2 for the solid line,  $1.322 \times 10^{11}$  W, 0.074, and 1.82 for the dashed line,  $1.057 \times 10^{11}$ ,  $8.76 \times 10^{-4}$ , and 5.08 for the dotted line respectively. .... 45
- Figure 2.6: Plots of the normalized spectral intensity on axis. Parameters correspond to those of Fig. 2.5. The dash-dotted line is the initial spectrum ( $t/T_R = 0$ ) with the same parameters as the solid line. .... 46

Figure 2.7: Time evolution of the on axis intensity for $P_{\max} = 1.19 \times 10^{11}$ W, $r_0 = 0.21$ cm, and $Z_L = 135$ cm. ....	47
Figure 2.8: Distribution of the radially integrated power as function of $\xi$ (same case as Fig. 2.7).....	48
Figure 2.9: On-axis maximal electron density as function of time (same case as Fig. 2.7). ....	49
Figure 2.10: Contour plots of the laser intensity over time with the peak input power $P_{\max} = 2.28 \times 10^{11}$ W. The spot size and pulse length are of the same as Fig. 2.1. .....	50
Figure 2.11: Radial profiles of the electron density and index coefficient $\chi$ at $t/T_R = 0.7$ and $\xi = 0.0113$ cm (same case as Fig. 2.10). ....	51
Figure 2.12: Evolution of the on axis intensity (same case as Fig. 2.10). ....	52
Figure 2.13: Distribution of the radially integrated power as function of $\xi$ for the case of Fig. 2.10. ....	53
Figure 2.14: Contour plots of the laser intensity over time with the peak input power $P_{\max} = 1.5 \times 10^{12}$ W, spot size $r_0 = 0.21$ cm, and pulse length $Z_L = 135$ cm. ....	54
Figure 2.15: Radial profiles of the real and imaginary parts of the complex amplitude of the vector potential $a$ at $t/T_R = 0.2$ and $\xi = 0.0066$ cm for the case of Fig. 2.14. ....	55
Figure 2.16: Evolution of the radii containing specified fractions of the pulse energy as function of time (same case as Fig. 2.13). The percentage numbers are of the	

total pulse energy contained within that radius. The average radius is defined by

$$\left[ \frac{\int |a(r, \xi, t)|^2 r^3 dr d\xi}{\int |a(r, \xi, t)|^2 r dr d\xi} \right]^{1/2} \dots\dots\dots 56$$

Figure 2.17: Contour plots of the laser intensity in air at  $t/T_R = 0.5$  after considering time delayed Raman response. The input parameters are  $P_{\max} = 3.87 \times 10^{11}$  W,  $r_0 = 0.21$  cm, and  $Z_L = 67.5$  cm. .... 57

Figure 2.18: Contour plot of the laser intensity in air at  $t/T_R = 0.15$  after considering time delayed Raman response with the initial peak power  $P_{\max} = 1.85 \times 10^{12}$  W, spot size  $r_0 = 0.21$  cm, and pulse length  $Z_L = 67.5$  cm. .... 58

Figure 3.1: Evolution of the average radius versus the propagation distance  $z$ , where  $z_0$  and  $r_0$  are the vacuum focusing location and the corresponding waist. The average radius is defined by  $\left[ \frac{\int |a(r, \xi, t)|^2 r^3 dr d\xi}{\int |a(r, \xi, t)|^2 r dr d\xi} \right]^{1/2}$  ..... 72

Figure 3.2: Evolution of the on-axis maximum electron density..... 73

Figure 3.3: On-axis intensity distribution in the laser frame at  $z = 27.71$  m. .... 74

Figure. 3.4 (a): Nonlinearity-induced phase changes at  $z = 27.71$  m. The dashed, solid, and dotted lines correspond to the case  $z_0 = 0.00$  m,  $r_0 = 0.21$  cm, the case  $z_0 = 6.93$  m,  $r_0 = 0.1878$  cm, and the case  $z_0 = 6.93$  m,  $r_0 = 0.0939$  cm respectively. .... 75

Figure. 3.4 (b): Plasma-induced phase changes at  $z = 27.71$  m. The dashed, solid, and dotted lines correspond to the case  $z_0 = 0.00$  m,  $r_0 = 0.21$  cm, the case  $z_0 = 6.93$  m,  $r_0 = 0.1878$  cm, and the case  $z_0 = 6.93$  m,  $r_0 = 0.0939$  cm respectively. .... 76

Figure. 3.4 (c): The sum of the nonlinearity-induced and the plasma-induced phase changes at  $z = 27.71$  m. The dashed, solid, and dotted lines correspond to the case  $z_0 = 0.00$  m,  $r_0 = 0.21$  cm, the case  $z_0 = 6.93$  m,  $r_0 = 0.1878$  cm, and the case  $z_0 = 6.93$  m,  $r_0 = 0.0939$  cm respectively. .... 77

Figure 3.5: Normalized nonlinearity-induced (circle), plasma-induced (square) instantaneous frequencies and their sum (diamond) at  $z = 27.71$  m for the case  $z_0 = 6.93$  m,  $r_0 = 0.1878$  cm. .... 78

Figure 3.6: On-axis spectral intensity for the previous three cases at  $z = 27.71$  m. The slight focusing case (solid line) has the most broadening spectrum compared with the tight focusing case (dotted line) and non-focusing case (dashed line). 79

Figure 3.7: Evolutions of the maximum on-axis electron density when the input power increases to  $2.28P_{cr}$ . .... 80

Figure 3.8: Contour of the laser intensity at  $z = 27.71$  m for the case  $r_0 = 0.21$  cm with input power  $P_{in} = 2.28P_{cr}$ . Pulse refocus at the trailing edge..... 81

Figure 3.9: Distributions of the nonlinear phase change (dashed line), plasma induced phase change (dotted line), and the summation of them (solid line) at  $z = 27.71$  m for the case  $r_0 = 0.21$  cm with  $P_{in} = 2.28P_{cr}$ . .... 82

Figure 3.10: Distributions of local nonlinear frequency (dashed line), plasma induced frequency (dotted line), and the summation of them (solid line) according to Fig. 3.9..... 83

Figure 3.11: Local frequency changes at  $z = 27.71$  m when input power is  $2.28P_{cr}$ .84

Figure 3.12: Image of spectral intensity at  $z = 27.71$  m for the case  $r_0 = 0.21$  cm  
when input power is  $2.28 P_{cr}$ . ..... 85

Figure 4.1: Channel density profiles at  $t = 0.7$  ns from the 1D hydrodynamic  
formation code. The formation pulse is focused into longitudinally uniform 550  
torr Helium with duration 150 ps (FWHM) and peak intensity  $1 \times 10^{14}$  W/cm<sup>2</sup>  
through an axicon at an approach angle of 15°. The solid lines are densities  
output by the 1D hydrodynamic formation code. The dashed lines are densities  
used in the propagation simulation. In simulation, two radii determine the  
electron distribution. From the on-axis to the half of the inner radius (15 μm),  
electron density is constant. Then it parabolicly increases until reaching the inner  
radius (30 μm). Afterward, it linearly decreases to zero at the outer radius (34  
μm). The density of He<sup>+2</sup> is constant up to  $r = 25$  μm, then parabolicly  
decreases to zero at the inner radius. The density of He<sup>+</sup> is extracted by using  
the particle number conservation law. .... 104

Figure 4.2: Tapered channel profiles produced at the half way of the gas density ramp  
(275 torr Helium) using the same formation pulse and at the same time as in Fig.  
4.1. The solid lines are densities output by the 1D hydrodynamic formation  
code. The dashed lines are densities used in the propagation simulation. .... 105

Figure 4.3: The funnel profiles produced at the half way of the gas density ramp (275  
torr Helium). The auxiliary funnel formation pulse (Gaussian) leads the channel  
formation pulse by 0.7 ns with a duration 100 ps and peak intensity  
 $2.5 \times 10^{14}$  W/cm<sup>2</sup>. The solid lines are densities output by the 1D hydrodynamic

formation code. The dashed lines are densities used in the propagation simulation..... 106

Figure 4.4: Schematic plots of the inner and outer funnel and channel radii. The inner funnel radius parabolically decreases from an inner mouth radius ( $60 \mu\text{m}$ ) at  $z = -0.1 \text{ cm}$  to a constant inner channel radius ( $30 \mu\text{m}$ ) at the channel entrance  $z = 0.0 \text{ cm}$ . This parabolic curve is determined by the inner channel radius at the channel entrance, the inner funnel radius at the half way of the density ramp, and the adjustable inner funnel mouth radius. The outer funnel radius has a similar variation from  $61 \mu\text{m}$  to  $34 \mu\text{m}$ . ..... 107

Figure 4.5: On-axis densities by jointing Fig.4.1 and Fig. 4.3. The electron density curve is selected so that it reaches the on-axis density at the half way of the ramp shown in Fig. 4.3, and reaches on-axis density at the channel entrance shown in Fig. 4.1. The  $\text{He}^{+2}$  density parabolically increases from zero to the half way density in Fig. 4.3 and finally reaches the channel  $\text{He}^{+2}$  density in Fig. 4.1. The  $\text{He}^+$  density is extracted by obeying the particle number conservation law. The gas density ramp starts at  $z = -0.1 \text{ cm}$ , ends at  $z = 0.0 \text{ cm}$  with a length of  $0.1 \text{ cm}$ . ..... 108

Figure 4.6: Surface plot of a funnel mouthed channel by jointing Fig. 4.1 and 4.3 using method stated in Fig. 4.4 and 4.5. .... 109

Figure 4.7: Surface plot of a tapered channel by jointing Fig. 4.1 and 4.2 using similar method stated in Fig. 4.4 and 4.5. .... 110

Figure 4.8: The evolution of the total laser energy and radius of percentage energy confined for a laser pulse propagation in the tapered channel shown in Fig. 4.7.

The injected pulse has a vacuum spot size of 15 $\mu\text{m}$ , duration of 100 fs, and energy of 70 mJ.....	111
Figure 4.9: The evolution of the total laser energy and radius of percentage energy confined for a laser pulse propagation in the funnel mouthed channel shown in Fig. 4.6. Same injected pulse is used as in Fig. 4.8. The solid line with squares demonstrates the evolution of pulse energy when the plasma wave is turned off. The solid line with circles is that when the plasma wave is on. ....	112
Figure 4.10: The fine dependences of the on-axis intensity and electron density perturbation at $z = 0.5 \text{ cm}$ . The bottom figure shows the on-axis intensity with the plasma wave off. The upper figure shows both the on-axis intensity (solid line) and electron density perturbation (dashed line).....	113
Figure 4.11: The evolution of the on-axis peak intensity in the funnel and channel. The same channel and laser pulse are used as those in Fig. 4.9. ....	114
Figure 4.12: The evolution of the total laser energy and radius of percentage energy confined for a laser pulse propagation in an ideal optimal low density channel, which has a similar profile shown in Fig. 4.6, but has a low on-axis electron density of $5 \times 10^{17} \text{ cm}^{-3}$ . The injected pulse has a vacuum spot size of 20 $\mu\text{m}$ , duration of 100 fs, and energy of 120 mJ. ....	115
Figure 4.13: The variation in the peak intensity on-axis for the pulse propagation in Fig. 4.12. A $\pm 10\%$ variation of the on-axis peak intensity is observed (solid line with circles) even when the input energy is doubled (solid line with squares). ....	116



Figure 4.14: The evolution of the total laser energy and radius of percentage energy confined for backfill. The funnel mouth radius is 10 times the channel radius. The laser pump enters the funnel at  $z = -2.0$  cm and the channel at  $z = 0.0$  cm. The vacuum focus is located at channel entrance..... 117

Figure 4.15: The dependence of the averaged on-axis peak intensity inside the channel on the location of the vacuum focus for backfill. The funnel mouth radius is fixed to ten times the channel radius, and funnel length fixed to two centimeters..... 118

Figure 4.16: The relation between the averaged on-axis peak intensity inside the channel and the normalized funnel mouth radius for backfill. The funnel length is fixed to two centimeters, and the vacuum focus is located at the channel entrance..... 119

Figure 4.17: Varying of the averaged on-axis peak intensity inside the channel with the funnel length for backfill. The funnel mouth radius is fixed to 10 times the channel radius, the vacuum focus is always located the connection of the funnel and the channel. .... 120

# Chapter 1: Introduction

## 1.1 Overview

Nonlinear propagation of laser pulses in gases, fluids and solids has been extensively studied over the past decade [1-11]. Propagation in gases undergoing ionization is relevant to applications, such as laser plasma accelerators [12], x-ray lasers [13], harmonic generation [14], and supercontinuum generation [15]. For these applications, the pulse should have high peak power and propagate stably for long distances. The propagation is affected by diffraction and refraction. Moreover, in nonlinear media, the strong field distorts the orbits of bound electrons in atoms and perturbs their eigen energy levels and wave functions. This perturbation translates to a classically intensity dependent refractive index change, characterized by the nonlinear refractive index  $n_2$ . The increase in the refractive index causes the pulse to nonlinearly focus. The minimum power required for Gaussian pulse to nonlinearly focus is given by the critical power [16],  $P_{cr} = \lambda^2 / (2\pi n_0 n_2)$ , where  $\lambda$  is the wavelength,  $n_0$  is the linear index of refraction. The self-focused laser pulse is eventually limited by some effect or combination of effects, such as ionization, plasma refraction, group velocity dispersion (GVD). Tunneling and multi-photon ionization by the high intensity pulse generates plasma [2,17]. The decrease in the refractive index, which is proportional to the plasma density, pushes the pulse off the axis. This phenomenon is known as plasma induced spatial defocusing or ionization induced refraction [2-4]. Nonlinear self-focusing can also be arrested by normal

GVD for powers that are not too large. By normal GVD we mean  $d^2k(\omega)/d\omega^2 > 0$ , where  $k(\omega)$  is the frequency dependent wave number of a linear plane wave propagating in the neutral gas medium. As the pulse focuses, the nonlinear response of the gas (assuming the nonlinear modification to the index is positive) causes the leading edge of the pulse to frequency down shift and the trailing edge to frequency up shift. For normal GVD the group velocity decreases with frequency. Thus, the leading edge moves faster than the trailing edge does, the pulse spreads and splits in time, which reduces the peak power and weakens the self-focusing.

The dynamic balance among these effects may lead to pulse self-guiding, where high power lasers are hoped to propagate over great distance. Experiments have indicated that pulses can be propagated for many meters with a large intensity confined to a small radial region [18,19]. However, there has been considerable controversy as to whether the observed effect is stable guiding [18], the so-called moving focus effect [7], or a more dynamic balance of gas self-focusing and ionization induced refraction [20]. Moreover, self-guided pulses are subject to ionization and modulation instabilities [21, 22], which limit the propagation distance. Thus the basic study of every aspect of these effects is crucial to the fully understanding of laser propagation in ionizing gases.

When an ultra short, high intensity, high power laser pulse passing through nonlinear media, a super-broadening spectrum can be observed [15, 23-30]. This super broadening spectrum covers the visible range and may even extend to the near

infrared and ultraviolet bands [25]. This phenomenon is well known as supercontinuum generation. It was first observed in condensed media when a powerful picosecond pulse was focused into glass samples [15]. Similar observations in high-pressure gases were reported later [27-29]. Supercontinuum is used to generate tunable ultrafast light pulses, which is needed in ultrafast spectroscopic studies [31], optical parametric amplification [32], dynamic characterization of laser induced structural transitions [33], and optical pulse compression [31]. Various mechanisms have been suggested to explain this phenomenon. Among them are commonly accepted self-phase modulation (SPM) [15,25,26], four wave mixing [23], ionization enhanced SPM [24], and self-steeping [26]. Even though self-steeping enhanced SPM is the commonly accepted main mechanism for supercontinuum generation, its theoretical prediction of a narrower continuum contradicts the experiment observation of a much broader continuum in the low nonlinearity of water [31]. Since by far none of these mechanisms alone can give us a complete understanding, supercontinuum generation remains an active research area today.

In nonlinear media, self-focusing enhanced SPM plays an important role in continuum generation. In the high power laser fields, the nonlinear response of the gases increases the refractive index of the media, which is proportional to the laser intensity. The index-modified media reacts back on the laser pulse, introduces a nonlinear phase change, known as self-phase modulation, which generally depends on the spatial and temporal profile of the intensity. The time derivative of this nonlinear phase change contributes new frequency components to the laser pulse. The

instantaneous frequency is Stokes shifted (i.e. red shifted) at the leading edge of the pulse and anti-Stokes shifted (i.e. blue shifted) at the trailing edge of the pulse. The transverse profile of the intensity results in a spatially dependent phase modulation, which distorts the wave front, and is responsible for the phenomena of nonlinear self-focusing. On focusing, the pulse shrinks in both spatial and temporal dimensions, and the peak intensity increases quickly. SPM is enhanced by this positive feedback. Therefore, it is not surprising that the power threshold for continuum generation coincides with the critical power for self-focusing, as demonstrated by experiments [6,27,29,34].

Self-focusing stops when peak intensity is greater than the threshold for ionization. In case ionization occurs, plasma induces a negative change in the refractive index at the trailing edge of the pulse, which is proportional to the electron density. The decrease in refractive index due to ionization cancels or even overwhelms the increase in refractive index caused by nonlinear response of the gases, thus plasma generation can arrest self-focusing. The asymmetric reduction in refractive index enhances SPM, which results in the blue shifted continuum. Media dispersion is another important factor for continuum generation. Group velocity dispersion rearranges the temporal distribution of pulse intensity, such that peak intensity and SPM are reduced. Thus for the study of continuum generation of high power laser pulses in gases, self-phase modulation, nonlinear self-focusing, ionization, and group velocity dispersion are coupled factors for consideration. To

fully understand spectrum super broadening, it is necessary to include all of these factors in the simulation model, which we attempt to do.

As an application of optical guiding of an intense laser pulses in plasma, laser wakefield accelerators (LWFA) aroused tremendous interest in the past two decades [35-39]. Three basic concepts have been proposed for the acceleration of charged particles by plasma waves: the plasma wakefield accelerator [37], the plasma beat-wave accelerator [38], and the laser wakefield accelerator [39]. These three plasma-based accelerators can provide extremely large acceleration gradient, such that GeV electron energies can be acquired in centimeters [39], and it is hoped that they will be more compact than existing accelerators. In comparison, the traditional radio frequency linear accelerators have an accelerating gradient limit of about 100 MeV/m, and consequently their length is measured in miles. The advantage over traditional accelerators goes without saying, and it is not surprising that plasma-based accelerators are very hot research topics.

Among these three most widely investigated schemes, the laser wakefield accelerator uses a very short ( $\sim 100$  fs), ultra intense ( $\geq 10^{18}$  W/cm<sup>2</sup>) laser pulse to drive a plasma wave. A strong plasma wave is excited when the laser pulse duration is about the plasma period, which is about 100 fs in time for a typical plasma density of  $1.24 \times 10^{18}$  cm<sup>-3</sup>. Due to the short required pulse length, LWFA appeared feasible only after chirped-pulse amplification technology was demonstrated [40]. Laser wake field accelerators work in either the self-modulation regime or the resonant

regime. The resonant regime corresponds to the case discussed above the pulse duration matches the plasma period. The self-modulation regime corresponds to a pulse of several or more plasma waves in duration. In this case the pulse spontaneously develops modulations on the plasma wave time scale due to Raman instability. The modulated pulse then drives a laser plasma wave. The advantage in self-modulation regime is that a larger accelerating field can be achieved for a given pulse duration, because a higher density plasma is employed. Difficulty in control is its main disadvantage, since it relies on an instability to excite plasma waves. In comparison, a LWFA working in the resonant regime is operated in a low plasma density regime. The resulting plasma wave is more stable, because it has less influence on the laser pulse.

Guiding of laser pulses prolongs the interaction of the laser with the propagation medium, so it is a key issue for LWFA. Several approaches to guiding have been studied. One approach is to use the natural self-focusing that occurs in a nonlinear medium. Such a nonlinearity can arise from the response of bound electrons in the atoms of a neutral gas, or from free electrons that are quivering relativistically. A second approach is to create some sort of guiding structure that confines radiation within the interaction region. Examples include capillary discharges [41], gas filled capillaries [42], and plasma channels created by thermally driven plasma expansions [43-49]. In the last approach, a waveguide formation pulse is line-focused into backfill [43-45] or gas jet [46-48] targets. Channels formed this way have been investigated extensively and found to be effective in guiding radiation

over many Rayleigh lengths. Waveguide propagation of a pulse at  $\sim 10^{17}$  W/cm<sup>2</sup> has been reported in a channel preformed in jet clustered gas [48]. Injection of pump pulses with intensity  $> 10^{17}$  W/cm<sup>2</sup> into axicon formed waveguides is hindered by the poor coupling of the laser to the waveguide entrance in both gas jet and backfill cases [44,48]. The poor coupling is a result of both waveguide taper at the entrance (the channel radius decreases as the end of the channel is approached) and ionization induced refraction of the laser pulse there. Improving the coupling efficiency will determine the operational success of LWFA, and remain an issue of intense study.

## 1.2 Purpose of the Dissertation

Recent theoretical studies show that [1, 9-11], under certain conditions, group velocity dispersion is an important factor in nonlinear laser pulse propagation. The combination of nonlinear self-phase modulation and group velocity dispersion leads to pulse splitting. Pulse splitting is observed in many different materials [1, 6, 9-11], and observation of multiple splitting has also been reported [11]. In all of the above references, in both theory and experiment, the media are dense gases, liquids or even solids, where the coefficient of GVD is considerably large. The importance of GVD to pulse propagation in tenuous gases, where the corresponding coefficient of GVD is very small, remains unknown.

In this thesis, we study the propagation behavior of moderate power laser pulses in tenuous gases at different power levels, around  $10^{11} \sim 10^{12}$  W. For low input power just above the critical value for self-focusing, the pulse produces almost no plasma due to its initially large laser spot size and low laser intensity. Nonlinear self-



focusing causes the laser pulse to collapse very quickly. We must consider the effect of group velocity dispersion, which arrests the self-focusing by splitting and spreading the temporal intensity profile. A heuristic argument shows that, in this power region, what is important is the normalized coefficient of GVD, which is proportional to the coefficient of GVD and spot size squared, and inverse to the pulse length squared. Also of importance is the value of the excess power factor  $\varepsilon = (P_{\max} - P_{cr})/P_{cr}$ , where  $P_{\max}$  is the maximum power. We find similar propagation behavior for laser pulses with different characteristic parameters but equal values of normalized coefficient of GVD divided by  $\varepsilon^3$ . For moderate power, plasma is generated and plasma defocusing overwhelms GVD. The peak region of the pulse is refracted due to the high gradient of plasma, but the trailing part of the pulse is off axis guided just outside the plasma region, which is resulted from the balance between the nonlinear self-focusing and plasma defocusing. For high input power, the pulse behavior is dominated by plasma defocusing. Part of the pulse is trapped in the plasma and then decays due to the generation of outgoing waves, which interfere with other portions of the pulse.

Our simulation model also applies to situations in which super continuum radiation is generated [30]. In this thesis we study the dependence of supercontinuum on the details of pulse propagation. Self-phase modulation, coupling with nonlinear self-focusing and GVD, generates new asymmetric frequency components that are red-shifted near the leading edge and blue-shifted near the trailing edge [13]. Tunneling and multi-photon ionization and plasma generation induce a blue shift at

the pulse center [3,8]. The goal of this research is to study these competing effects and determine the laser parameters for which each effect is dominant. Particular attention is focused on the regime in which the pulse propagates for many meters in gas under the influence of nonlinear self-focusing and ionization induced refraction.

Guiding of pulse in preformed plasma channels is needed in a number of applications. However, coupling of a high intensity pulse into a plasma channel can be difficult due to the presence of gas at the entrance of the channel or due to the channel having a closed entrance. To overcome these effects, we consider “grafting” a plasma funnel onto the preformed waveguide using an auxiliary formation pulse [48]. This funnel formation pulse can precede or follow the waveguide generation pulse such that different funnel shapes can be selected. This “grafted” funnel eliminates the neutral gas near the channel entrance and provides a focusing element to funnel the high intensity laser pulse into the channel [48]. In this thesis, we study the coupling process by examining the coupling efficiency of laser pulses to the funnel-mouthed channels of a variety of shapes in both backfill and gas jet Helium. The initial profiles for the waveguide are generated using the waveguide formation code developed by H. M. Milchberg [49]. This code determines time dependent radial profiles of electron and ion density and temperature. Parameters of the funnel and channel are obtained by varying the gas density, the intensities of the funnel formation pulse and the channel formation pulse, the time delay between the formation pulses, and the time between channel formation pulse and the injected pulse. The electron and ion densities are then modeled with simple formulas that

captured their essential features by allowing the parameters to vary with axial distance. This information is imported to our model, which then simulates the propagation of the short pulse laser. The effective coupling can be most easily achieved in gas jet targets. This is because ionization induced refraction is so strong, that unreasonably long entrance funnels (1~2 cm) are required in backfill targets. In gas jet targets the entrance funnel only needs to extend the short distance (1~2 mm) between the channel and edge of the gas jet, and high coupling efficiencies can be achieved.

### 1.3 Organization of the Dissertation

The remainder of this thesis is organized as follows. Chapter 2 presents the basic study of the propagation behavior of ultra-short, high intensity laser pulses in tenuous gases undergoing ionization. Chapter 3 discusses the dependence of supercontinuum on the laser geometry. In chapter 4, we study the coupling efficiency between the injected pulse and the preformed funnel-mouthed plasma channel for both gas jet and backfill cases. Finally, in chapter 5, a conclusion is briefly discussed.

## Chapter 2: Laser Pulse Splitting and Trapping in Tenuous Gases

### 2.1 Introduction

Nonlinear propagation of laser pulses in gases, fluids and solids has been extensively studied over the past decade [1-10]. Propagation in gases undergoing ionization is relevant to applications, such as laser plasma accelerators [11], x-ray lasers [12] and harmonic generation [13]. For these applications, the pulse should have high peak power and propagate stably for long distances. The propagation is affected by diffraction and refraction, moreover, if the peak power is large enough, that is, greater than a certain critical power [14],  $P_{cr} = \lambda^2 / (2\pi n_0 n_2)$ , where  $\lambda$  is the wave length,  $n_0$  is the linear index of refraction and  $n_2$  is the second order coefficient of the nonlinear index of refraction, the nonlinear response of the gas causes the pulse to focus. Eventually self-focusing is limited by some effect or combination of effects. In our studies we include ionization of the gas and group velocity dispersion. Ionization by the high intensity pulse generates plasma. The decrease in the refraction index then pushes the pulse off the axis, which is known as plasma induced spatial defocusing or ionization induced refraction [2, 3]. Group velocity dispersion (GVD) spreads the pulse in time. The parameter regions in which these effects compete will be explored.

Recent theoretical studies show that [1, 8-10], under certain conditions, group velocity dispersion is an important factor in laser pulse propagation. As mentioned

above, nonlinear self-focusing can be halted by plasma defocusing in space; it can also be arrested by normal GVD for powers that are not too large. By normal GVD we mean  $d^2k(\omega)/d\omega^2 > 0$ , where  $k(\omega)$  is the frequency dependent wave number of a linear plane wave propagating in the neutral gas medium. As the pulse focuses, the nonlinear response of the gas (assuming the nonlinear modification to the index is positive) causes the leading edge of the pulse to frequency down shift and the trailing edge to frequency up shift. For normal GVD the group velocity decreases with frequency. Thus, normal GVD spreads and splits the pulse in time and reduces the peak power, thus weakening the self-focusing. Pulse splitting is observed in many different materials [1, 5, 8-10], and observation of multiple splitting has also been reported [10]. In all of the above references, in both theory and experiment, the media are dense gases, liquids or even solids, where the coefficient of GVD is considerably large.

In this chapter, we focus on the propagation of moderate power, around  $10^{11} \sim 10^{12}$  W, laser pulses in tenuous gases, where the corresponding coefficient of GVD is very small. We study the pulse behavior at different power levels. For low input power, that is power levels just above the critical value for self-focusing, the pulse produces almost no plasma due to its initially large laser spot size and low laser intensity. Nonlinear self-focusing causes the laser pulse to collapse very quickly. During the collapse the pulse acquires a sharp peak and we must consider the effect of group velocity dispersion (GVD), which spreads the pulse, lowers the power, and arrests the self-focusing. For moderate power, plasma is generated and plasma

defocusing overwhelms GVD. The peak region of the pulse is refracted due to the high gradient of plasma, but the trailing part of the pulse can still be trapped just outside the plasma region. Thus, in the moderate power regime, the pulse is guided off axis. For high power, the pulse behavior is dominated by plasma defocusing. However, part of the pulse is trapped in the plasma and then decays due to the generation of outgoing waves, which interfere with other portions of the pulse.

Our calculations are relevant to a form of guiding that has been discussed in the literature. It is achieved due to the balance between the nonlinear self-focusing of a background gas and refraction due to the creation of plasma near the axis by tunneling and multi-photon ionization of the gas. Experiments have indicated that pulses can be propagated for many meters with a large intensity confined to a small radial region [15]. However, there has been considerable controversy as to whether the observed effect is stable guiding [15], the so-called moving focus effect [6], or a more dynamic balance of gas self focusing and ionization induced refraction [16]. Our calculations also apply to situations in which super continuum radiation is generated [17]. Here, broad spectra are generated which depend on details of pulse propagation.

The remainder of this chapter is organized as follows. In section 2.2 we give the basic equations for our theoretical model. In section 2.3 we analyze the numerical simulations in different regions of input power. Section 2.4 contains a brief summary and conclusion.

## 2.2 Model

The laser field is determined by Maxwell's equations, which in the Lorenz gauge become

$$\left( \frac{1}{c^2} \frac{\partial^2}{\partial t^2} - \nabla^2 \right) \mathbf{A} = \frac{4\pi}{c} \mathbf{J} + \frac{4\pi}{c} \frac{\partial \mathbf{P}}{\partial t}, \quad (2.1)$$

where  $\mathbf{A}$ ,  $\mathbf{J}$  and  $\mathbf{P}$  are the vector potential, the current density of free charges and the polarization of the medium respectively. We now assume the laser field is nearly monochromatic with a narrow spectrum centered on frequency  $\omega_0$ , the Fourier expansions of  $\mathbf{A}$  and  $\mathbf{P}$  are

$$\mathbf{A} = \mathbf{e} \frac{1}{2\pi} \int \bar{A}(\omega) e^{-i\omega t} d\omega, \quad (2.2)$$

and

$$\mathbf{P} = \mathbf{e} \frac{1}{2\pi} \int \bar{P}(\omega) e^{-i\omega t} d\omega, \quad (2.3)$$

where  $\mathbf{e}$  is the polarization direction, and  $\bar{A}(\omega)$  and  $\bar{P}(\omega)$  will be peaked about  $\omega_0$ .

We insert (2.2) and (2.3) in Eq. (2.1), which gives

$$-\frac{\omega^2}{c^2} \bar{A} - \nabla^2 \bar{A} = \frac{4\pi}{c} \bar{J} - \frac{4\pi i \omega}{c} \bar{P}. \quad (2.4)$$

The polarization density will contain both the linear and nonlinear response of the gas in which the pulse propagates. At this point, in the derivation we assume the response is dominantly linear in which case the constitutive relation  $\bar{P}(\omega) = \chi(\omega) \bar{E}(\omega)$  and the relation  $\bar{E}(\omega) = i\omega \bar{A}(\omega)/c$  give

$$\bar{P}(\omega) = \frac{i\omega}{c} \chi(\omega) \bar{A}(\omega) . \quad (2.5)$$

Corrections to this will be added later. Combining Eqs. (2.4) and (2.5) yields

$$-\frac{\omega^2}{c^2} \varepsilon(\omega) \bar{A}(\omega) - \nabla^2 \bar{A}(\omega) = \frac{4\pi}{c} \bar{J}(\omega) , \quad (2.6)$$

where the dielectric constant  $\varepsilon(\omega) = 1 + 4\pi\chi(\omega)$  and  $\chi(\omega)$  is the electric susceptibility of the gas medium. The free electron response of the plasma will be treated separately.

To obtain equations in the time domain we must take the inverse Fourier transform of (2.6). Before doing this we first expand  $\varepsilon(\omega)$  around the laser frequency,  $\omega_0$ ,

$$\frac{\omega^2}{c^2} \varepsilon(\omega) = \alpha_0 + \alpha_1 (\omega - \omega_0) + \alpha_2 (\omega - \omega_0)^2 , \quad (2.7)$$

where the constants are defined as,

$$\alpha_0 = \frac{\omega_0^2}{c^2} \varepsilon(\omega_0) ,$$

$$\alpha_1 = \left. \frac{\partial}{\partial \omega} \left( \frac{\omega^2}{c^2} \varepsilon(\omega) \right) \right|_{\omega=\omega_0} ,$$

and

$$\alpha_2 = \left. \frac{1}{2} \frac{\partial^2}{\partial \omega^2} \left( \frac{\omega^2}{c^2} \varepsilon(\omega) \right) \right|_{\omega=\omega_0} .$$

Next we substitute expansion (2.7) into Eq. (2.6), and take the inverse Fourier transform to obtain,



$$-\alpha_0 \hat{A} - i\alpha_1 \frac{\partial \hat{A}}{\partial t} + \alpha_2 \frac{\partial^2 \hat{A}}{\partial t^2} - \nabla^2 \hat{A} = \frac{4\pi}{c} \hat{J} , \quad (2.8)$$

where  $\hat{A}(x, y, z, t) = (1/2\pi) \int_0^\infty \bar{A}(x, y, z, \omega) e^{i(\omega_0 - \omega)t} d\omega$  is the complex amplitude of the vector potential and  $\hat{J}$  is the similarly defined complex amplitude of the current density.

In the laser frame, that is, a frame moving near the speed of light, the field varies slowly, which makes it easier for us to analyze its properties. So the next step is to transform from the lab frame to the laser frame by introducing the variable  $\xi = v_f t - z$ , where  $v_f$  is the frame velocity. The frame velocity can be chosen arbitrarily, for example, it could be the speed of light in vacuum or it could be the group velocity  $v_g$  based on linear propagation in the gas. A suitable frame velocity  $v_f$  is the one for which the field varies slowly. Thus, in our new coordinates the dependence of  $\hat{A}(t, \xi, \mathbf{x}_\perp)$  on  $t$  will be weak and we will drop the second order derivative in  $t$ . Introducing the frame velocity and assuming the field has the general form of a plane wave multiplied by a complex envelope, we write,

$$\hat{A}(t, z, \mathbf{x}_\perp) = A(t, \xi = v_f t - z, \mathbf{x}_\perp) e^{ik_0 z} , \quad (2.9)$$

where  $k_0 = \omega_0/c$  is the laser wave number in vacuum. Further, the contribution to the current density  $\hat{J}$  from the plasma is  $\hat{J} = -(q/mc) \langle n_e / \gamma \rangle A e^{ik_0 z}$  [7], where  $n_e$  is the electron density,  $\gamma = (1 - v^2/c^2)^{-1/2}$  is the relativistic factor, and the angular bracket denotes average over one period of the laser. Inserting (2.9) into Eq. (2.8),

dropping the small term  $\partial^2 A/\partial t^2$ , and inserting the expression for the current density then gives,

$$\begin{aligned}
& -\left(k_0^2 - \alpha_0\right) A + \left(i\alpha_1 - 2\alpha_2 v_f \frac{\partial}{\partial \xi}\right) \frac{\partial A}{\partial t} + i\left(\alpha_1 v_f - 2k_0\right) \frac{\partial A}{\partial \xi} \\
& -\left(\alpha_2 v_f^2 - 1\right) \frac{\partial^2 A}{\partial \xi^2} + \nabla_{\perp}^2 A = \frac{4\pi q^2}{mc^2} \left\langle \frac{n_e}{\gamma} \right\rangle A. \quad (2.10)
\end{aligned}$$

To simply matters we introduce the following normalized field:  $\tilde{a} = qA/mc^2$ , and we express the coefficients  $\alpha_0, \alpha_1$  and  $\alpha_2$ , writing  $\varepsilon(\omega) = 1 + \delta\varepsilon(\omega)$ , where we will assume  $\delta\varepsilon(\omega) \ll 1$ . We denote  $\delta\varepsilon(\omega_0)$  as  $\delta\varepsilon_0$ , then we have

$$\begin{aligned}
\alpha_0 &= \frac{\omega_0^2}{c^2} \varepsilon(\omega_0) = k_0^2 (1 + \delta\varepsilon_0), \\
\alpha_1 &= \left. \frac{\partial}{\partial \omega} \left( \frac{\omega^2}{c^2} \varepsilon(\omega) \right) \right|_{\omega=\omega_0} = \frac{2\omega_0}{c^2} (1 + \delta\varepsilon_0) + k_0^2 \left. \frac{\partial \delta\varepsilon(\omega)}{\partial \omega} \right|_{\omega=\omega_0}, \\
\alpha_2 &= \left. \frac{1}{2} \frac{\partial^2}{\partial \omega^2} \left( \frac{\omega^2}{c^2} \varepsilon(\omega) \right) \right|_{\omega=\omega_0} = \frac{1}{c^2} (1 + \delta\varepsilon_0) + \frac{2\omega_0}{c^2} \left. \frac{\partial \delta\varepsilon(\omega)}{\partial \omega} \right|_{\omega=\omega_0} + \frac{1}{2} k_0^2 \left. \frac{\partial^2 \delta\varepsilon}{\partial \omega^2} \right|_{\omega=\omega_0}.
\end{aligned}$$

We insert the expansions into Eq. (2.10). Then, the first term becomes

$$\left(k_0^2 - \alpha_0\right) \tilde{a} = -k_0^2 \delta\varepsilon_0 \tilde{a}.$$

The second term becomes

$$\left(i\alpha_1 - 2\alpha_2 v_f \frac{\partial}{\partial \xi}\right) \frac{\partial}{\partial t} \tilde{a} \simeq \frac{2}{c} \left(ik_0 - \frac{\partial}{\partial \xi}\right) \frac{\partial}{\partial t} \tilde{a},$$

where we have used the lowest order approximations to  $\alpha_1$  and  $\alpha_2$ , because the time derivative appearing in this term is already very small. That is,  $\alpha_1 \simeq 2\omega_0/c^2$  and  $\alpha_2 \simeq 1/c^2$ , and we assume  $v_f/c \simeq 1$ . The third term becomes

$$i(\alpha_1 v_f - 2k_0) \frac{\partial \tilde{a}}{\partial \xi} \simeq ik_0 \left[ 2 \left( \frac{v_f}{c} - 1 \right) + 2\delta\varepsilon_0 + \omega_0 \left. \frac{\partial \delta\varepsilon}{\partial \omega} \right|_{\omega=\omega_0} \right] \frac{\partial \tilde{a}}{\partial \xi} = ik_0 \beta_1 \frac{\partial \tilde{a}}{\partial \xi},$$

with the coefficient

$$\beta_1 = 2 \left( \frac{v_f}{c} - 1 \right) + 2\delta\varepsilon_0 + \omega_0 \left. \frac{\partial \delta\varepsilon}{\partial \omega} \right|_{\omega=\omega_0} = \delta\varepsilon_0 + 2 \frac{v_f - v_g}{c},$$

and the group velocity in the gas is given by

$$v_g = \left. \frac{d\omega}{dk} \right|_{\omega=\omega_0} \simeq c \left[ 1 - \frac{1}{2} \left( \delta\varepsilon_0 + \omega_0 \left. \frac{\partial \delta\varepsilon}{\partial \omega} \right|_{\omega=\omega_0} \right) \right].$$

The fourth term becomes,

$$(\alpha_2 v_f^2 - 1) \frac{\partial^2 \tilde{a}}{\partial \xi^2} = \left[ \frac{v_f^2}{c^2} - 1 + \delta\varepsilon_0 + 2\omega_0 \left. \frac{\partial \delta\varepsilon}{\partial \omega} \right|_{\omega=\omega_0} + \frac{1}{2} \omega_0^2 \left. \frac{\partial^2 \delta\varepsilon}{\partial \omega^2} \right|_{\omega=\omega_0} \right] \frac{\partial^2 \tilde{a}}{\partial \xi^2} = \beta_2 \frac{\partial^2 \tilde{a}}{\partial \xi^2},$$

with coefficient

$$\beta_2 = \frac{v_f^2}{c^2} - 1 + \delta\varepsilon_0 + 2\omega_0 \left. \frac{\partial \delta\varepsilon}{\partial \omega} \right|_{\omega=\omega_0} + \frac{1}{2} \omega_0^2 \left. \frac{\partial^2 \delta\varepsilon}{\partial \omega^2} \right|_{\omega=\omega_0}.$$

After considering the above approximations, Eq. (2.10) can be rewritten

$$\frac{2}{c} \frac{\partial}{\partial t} \left( ik_0 - \frac{\partial}{\partial \xi} \right) \tilde{a} + ik_0 \beta_1 \frac{\partial \tilde{a}}{\partial \xi} - \beta_2 \frac{\partial^2 \tilde{a}}{\partial \xi^2} + \nabla_{\perp}^2 \tilde{a} = \left( \frac{4\pi q^2}{mc^2} \left\langle \frac{n_e}{\gamma} \right\rangle - k_0^2 \delta\varepsilon_0 \right) \tilde{a}. \quad (2.11)$$

Generally we should also consider the contribution to the refractive index from the non-linear response of the gas. We will simply add this effect to the right hand side of (2.11). That is, we replace  $\delta\varepsilon_0$  as follows

$$\delta\varepsilon_0 \Rightarrow \delta\varepsilon_0 + 2n_2 \otimes I,$$

where  $I = (c/2\pi)|\omega mc\tilde{a}/q|^2$  is the laser intensity in units of  $\text{erg}/(\text{sec}\cdot\text{cm}^2)$  and  $n_2 \otimes I$  is a convolution giving the nonlinear dielectric response of the gas. For the simplest model the gas responds instantly and  $n_2 \otimes I = n_2 I(t)$ , where  $n_2$  is the second order nonlinearity coefficient. We will consider the effect of a delayed component of the response later in this paper.

Equation (2.11) can be further simplified if coefficients  $\delta\varepsilon_0$ ,  $\beta_1$  and  $\beta_2$  are constants. We introduce a frequency shift by assuming  $\tilde{a} = a(x_\perp, \xi, t)e^{-i\delta\omega t}$ , and substitute it into Eq. (2.11), we then have

$$\begin{aligned} \frac{2}{c} \frac{\partial}{\partial t} \left( ik_0 - \frac{\partial}{\partial \xi} \right) a + i \left( k_0 \beta_1 + \frac{2\delta\omega}{c} \right) \frac{\partial a}{\partial \xi} - \beta_2 \frac{\partial^2 a}{\partial \xi^2} + \nabla_\perp^2 a \\ = \left( \frac{4\pi q^2}{mc^2} \left\langle \frac{n_e}{\gamma} \right\rangle - 2k_0^2 n_2 \otimes I - k_0^2 \delta\varepsilon_0 - \frac{2k_0 \delta\omega}{c} \right) a. \end{aligned}$$

Since  $\delta\omega$  is arbitrary, we can choose it such that  $-k_0^2 \delta\varepsilon_0 - 2k_0 \delta\omega/c = 0$ , that is,  $2\delta\omega/c = -k_0 \delta\varepsilon_0$ . Inserting this into the above equation, we get the simplified equation

$$\begin{aligned} \frac{2}{c} \frac{\partial}{\partial t} \left( ik_0 - \frac{\partial}{\partial \xi} \right) a + ik_0 (\beta_1 - \delta\varepsilon_0) \frac{\partial a}{\partial \xi} - \beta_2 \frac{\partial^2 a}{\partial \xi^2} + \nabla_\perp^2 a \\ = \left( \frac{4\pi q^2}{mc^2} \left\langle \frac{n_e}{\gamma} \right\rangle - 2k_0^2 n_2 \otimes I \right) a, \quad (2.12) \end{aligned}$$

where  $\beta_1 - \delta\varepsilon_0 = 2(\mathbf{v}_f - \mathbf{v}_g)/c$ . It is obvious that Eq. (2.12) will be concise if we choose the frame velocity to be the group velocity,  $\mathbf{v}_f = \mathbf{v}_g$ . In this special case, we have

$$\frac{2}{c} \frac{\partial}{\partial t} \left( ik_0 - \frac{\partial}{\partial \xi} \right) a - \beta_2 \frac{\partial^2 a}{\partial \xi^2} + \nabla_{\perp}^2 a = k_p^2 \chi a, \quad (2.13)$$

where  $k_p^2 = \omega_p^2 / c^2 = 4\pi q^2 n_0 / (mc^2)$ ,  $n_0$  is the ambient electron density. The coefficients are

$$\beta_2 = \frac{v_g^2}{c^2} - 1 + \delta\epsilon_0 + 2\omega_0 \left. \frac{\partial \delta\epsilon}{\partial \omega} \right|_{\omega=\omega_0} + \frac{1}{2} \omega_0^2 \left. \frac{\partial^2 \delta\epsilon}{\partial \omega^2} \right|_{\omega=\omega_0} = \omega_0 c \left. \frac{d^2 k}{d\omega^2} \right|_{\omega=\omega_0}, \quad (2.14)$$

and

$$\chi = \left\langle \frac{n_e}{n_0 \gamma} \right\rangle - 2 \frac{k_0^2}{k_p^2} n_2 \otimes I. \quad (2.15)$$

Equation (2.13) accounts for the second order GVD, axial flow of laser power, transverse diffraction, ionization, plasma defocusing, relativistic self-focusing and nonlinear self focusing.

We now discuss the model of the plasma response. The electron density and relativistic factor will be calculated to second order in the laser intensity. Thus, we write the electron density

$$n_e = n_0 + \delta n,$$

where  $\delta n$  is the perturbation which is the first order in the laser intensity.

The electron density is determined by the rate of ionization of the gas atoms in the laser field. In the laser frame coordinates, the evolution of the electron density as well as the density of the various ionization stages of the gas atoms is given by [18],

$$c \frac{\partial}{\partial \xi} n_{g,i} = v_i(a) n_{g,i-1} - v_{i+1}(a) n_{g,i}, \quad (2.16)$$

$$c \frac{\partial}{\partial \xi} n_e = \sum_{i=1}^Z \nu_i(a) n_{g,i-1}. \quad (2.17)$$

where  $n_{g,i}$  is the density of gas atoms which have been ionized  $i$  times, and  $\nu_i(a)$  is the rate at which the  $i$ th electron is ionized. This rate is given by [2]

$$\nu_i(a) = \frac{\Omega}{2} C_n^2 \frac{\chi_i}{\chi_h} \frac{(2l+1)(l+|m|)!}{2^{|m|}(|m|)!(l-|m|)!} \left[ 2 \left( \frac{\chi_i}{\chi_h} \right)^{3/2} \frac{a_h}{a} \right]^{2n^* - |m| - 1} \exp \left[ -\frac{2}{3} \left( \frac{\chi_i}{\chi_h} \right)^{3/2} \frac{a_h}{a} \right]. \quad (2.18)$$

where  $\Omega = mq^4/\hbar^3$  is the atomic frequency,  $\hbar$  is Planck's constant,  $a_h = r_e \lambda / 4\pi a_0^2$  is a normalization factor for the vector potential such that  $a/a_h$  measures the electric field of the laser in units of the atomic electric field,  $a_0 = \hbar^2/(mq^2)$  is the Bohr radius,  $r_e = q^2/mc^2$  is the classical electron radius,  $\chi_h$  is the ionization potential of hydrogen,  $\chi_i$  is the ionization potential of the ion of interest,  $n^* = Z\sqrt{\chi_h/\chi_i}$ ,  $Z$  is the total number of electrons per atom, for  $n^* \gg 1$ ,  $C_n^* \approx (2q/n^*)/\sqrt{2\pi n^*}$ , and  $l, m$  are angular momentum and magnetic quantum number respectively. This model describes tunneling ionization when the laser frequency is lower than the resonant frequency for single photon ionization of the gas. At low intensity the ionization rate is exponentially small. In this case we replace the tunneling rate by one designed to model multi-photon ionization [19, 20]

$$\nu_i(a) = \nu_{0i} a^\beta, \quad (2.19)$$

where  $\nu_{0i}$  is picked to match smoothly to the tunneling rate, and  $\beta = 7.5$  represents the order of the process in electric field strength.

The perturbed electron density is determined by the quasi-static, weakly relativistic fluid equations. The continuity and momentum equations in the laser frame are given by [2]

$$c \frac{\partial}{\partial \xi} \delta n - \frac{\partial}{\partial \xi} n_0 v_z + \frac{1}{r} \frac{\partial}{\partial r} r n_0 v_r = 0, \quad (2.20)$$

$$mc \frac{\partial}{\partial \xi} n_0 v_r = n_0 \left( -q \frac{\partial}{\partial r} \phi - \frac{mc^2}{2} \frac{\partial}{\partial r} |a|^2 \right), \quad (2.21)$$

and

$$mc \frac{\partial}{\partial \xi} n_0 v_z = n_0 \left( q \frac{\partial}{\partial \xi} (\phi - A_z) + \frac{mc^2}{2} \frac{\partial}{\partial \xi} |a|^2 \right). \quad (2.22)$$

where  $v_r$  and  $v_z$  are the radial and axial fluid velocities, which are assumed to be first order in the laser intensity. The electromagnetic field of the wake is generated by the scalar potential  $\phi$  and magnetic vector potential  $A_z$ . In principle, vector potential must be included because of the spatially inhomogeneous ambient density  $n_0(r, \xi, t)$ . Finally, the wake fields are determined by the axial and radial components of Ampere's law

$$-\frac{1}{r} \frac{\partial}{\partial r} r \frac{\partial A_z}{\partial r} = \frac{4\pi}{c} q n_0 v_z + \frac{\partial^2}{\partial \xi^2} (\phi - A_z), \quad (2.23)$$

and

$$-\frac{\partial^2 A_z}{\partial r \partial \xi} = \frac{4\pi}{c} q n_0 v_r - \frac{\partial^2 \phi}{\partial r \partial \xi}. \quad (2.24)$$

Using the electron density perturbation and assuming that the nonlinear response of the gas is instant, we can rewrite Eq. (2.15) as,

$$\chi = 1 + \frac{\delta n}{n_0} - \frac{1}{2}|a|^2 - 2\frac{k_0^2}{k_p^2}n_2I. \quad (2.25)$$

This completes our description of the analytical model used in our studies.

## 2.3 Numerical Simulation

We wish to find a stable numerical approach to solve Eq. (2.13). Generally implicit schemes are the most robust and allow for the largest time steps. However, an implicit scheme applied directly to Eq. (2.13) requires inversion of an operator with second derivatives in both the transverse coordinate ( $\nabla_{\perp}^2$ ) and time ( $\partial^2/\partial\xi^2$ ). Such an inversion is possible if one were working in Fourier space. We however wish to carry out all steps in real space because the nonlinear and spatially varying terms can be evaluated directly in physical space. For this reason we consider a split step algorithm [21] which we now describe. For a general differential equation with operators  $L_0$  and  $L_1$ ,

$$\left(\frac{\partial}{\partial t} + L_0 + L_1\right)a = 0, \quad (2.26)$$

we can numerically integrate it in two steps. First, we apply the operator  $L_0$  for every  $dt$  step

$$\frac{a^{t+dt} - a^t}{dt} + L_0 \frac{a^{t+dt} + a^t}{2} = 0, \quad (2.27)$$

then apply  $L_1$  every two  $dt$  steps with a double step size  $2dt$

$$\frac{a^{t+2dt} - a^t}{2dt} + L_1 \frac{a^{t+2dt} + a^t}{2} = 0. \quad (2.28)$$



These two steps operate alternately, and this method is stable as long as the two operators can be inverted individually. Returning to our Eq. (2.13), we solve it by defining

$$L_0 = \frac{ic}{2k_0} \left( \frac{2}{c} \frac{\partial^2}{\partial t \partial \xi} - \nabla_{\perp}^2 + k_p^2 \chi \right), \quad (2.29)$$

and

$$L_1 = \frac{ic}{2k_0} \beta_2 \frac{\partial^2}{\partial \xi^2}. \quad (2.30)$$

The finite differencing of Eqs. (2.27) and (2.28), after inserting operators (2.29) and (2.30), yields two tri-diagonal matrix equations. These equations are solved by the standard double sweep recursion algorithm [21]. The radial boundary condition is discussed in detail in the appendix of Ref. [4], which allows outgoing waves at the radially outmost points. The boundary conditions imposed on the inversion of Eq. (2.28) are as follows. We suppose that  $a(0) = 0$ . That is, we do not allow pulse energy to run ahead of the laser frame. At the maximum value  $\xi_{\max}$ , we assume that the inversion of Eq. (2.28) includes no change in the value of  $a(\xi_{\max})$ , that is,  $a^{t+2dt}(\xi_{\max}) = a^t(\xi_{\max})$ . This allows pulse energy to fall behind the laser frame as described by Eq. (2.27). Generally, the simulation region is large enough so that there are no visible reflections of waves at either boundary.

In our simulation, the initial laser profile is chosen as,

$$a(r, \xi, t = 0) = \frac{a_{\max}}{(1 - it_0/T_R)} \exp\left(-\frac{r^2}{r_0^2 (1 - it_0/T_R)}\right) \sin\left(\frac{\pi \xi}{Z_L}\right), \quad (2.31)$$

where  $a_{\max}$  is the maximum amplitude, and  $r_0$  is the spot size that would be achieved in vacuum at the focus,  $t_0$  is the time at which the vacuum focus would occur, and  $T_R = Z_R / c$  where  $Z_R = k_0 r_0^2 / 2$  is the Rayleigh length. The temporal profile of the pulse envelope is taken to be a half sine wave with full width at half maximum of the intensity equal to  $Z_L / 2c$ . The typical parameters we consider are as follows. The laser wavelength  $\lambda$  is 800 nm and the spot size  $r_0$  is fixed at 0.21 cm, which corresponds to a Rayleigh range of 17.3 m. The pulse duration  $Z_L / c$  is chosen to be either 450 fs or 225 fs, the corresponding full widths at half maxima (FWHM) are about 225 fs and 112.5 fs respectively. The medium is uniformly distributed 0.41 atmosphere of Argon, with nonlinear coefficient  $n_2 = 2.275 \times 10^{-20} \text{ cm}^2/\text{W}$  for one atm of Argon. For  $\lambda = 800$  nm, the quantities in Eq. (2.14) are  $k'' = \partial^2 k / \partial \omega^2 = 0.083 \text{ fs}^2/\text{cm}$ , and  $\beta_2 = 5.87 \times 10^{-6}$ . Therefore, the corresponding GVD is normal. The constant  $a_{\max}$  will be varied so that phenomena corresponding to different input powers can be studied.

### 2.3.1 Phenomena corresponding to various input powers

In this subsection, we study self-focusing phenomena in several regimes of peak input power. We initialize the pulse with a spot size that is sufficiently large so that the initial peak intensity is below the threshold for ionization. We then allow the pulse to focus, either linearly or nonlinearly, and examine the evolution of various pulse characteristics.

### 2.3.1.1 Pulse splitting in the critical power regime

The laser pulse will self-focus when the input power is greater than the critical power  $P_{cr}$ . In media such as dense gases, liquids or solids, the coefficient of GVD is relatively large and can be expected to affect the pulse as it focuses. However, in tenuous gases, the coefficient of GVD is much smaller and we would not expect it to have much effect. A case when GVD is important in tenuous gases is when the peak power of the pulse is just above the critical power for self-focusing. In this case only the central portion of the pulse is above critical power and will focus. This has the effect of substantially shortening the pulse intensity on axis and as a consequence GVD will be more effective. Further, the dispersion only needs to make a small change to the pulse power to halt the nonlinear focusing.

This case is illustrated in the following example, where a laser pulse propagates in 0.41 atm of argon. Figure 2.1 shows the time evolution of the normalized laser intensity. In this case, the peak input power  $P_{max} = 1.14 \times 10^{11}$  W, is above the critical power for nonlinear self-focusing, which we estimate by a series of simulations to be about  $1.0 \times 10^{11}$  W in our model. The critical power given by the analytic formula  $P_{cr} = \lambda^2 / (2\pi n_0 n_2)$  is  $1.09 \times 10^{11}$  W, which is about nine percent higher than our estimated one. The difference arises because the value of critical power is radial-profile dependent. The central portion of the pulse focuses and the intensity on axis increases dramatically. This is illustrated in Fig. 2.2, where the on axis intensity is plotted as a function of  $\xi = v_g t - z$  (time in the pulse) for the same

four propagation distances. The initial formation of a central peak and the subsequent splitting are clearly evident. The forward spike remains for more than six Rayleigh times, with its peak intensity slowly dropping down due to diffraction. Figure 2.3 shows the evolution of the radially integrated power over the same propagation distance. The power has been redistributed in time ( $\xi = v_g t - z$ ) due to the combined effects of nonlinearity and dispersion. Power from the central peak has been shifted forward and backward in the pulse. The front to back asymmetry is the result of including the mixed derivative in Eq. (2.13).

We now address the issue of determining the range of parameters that GVD can be expected to arrest self-focusing before the intensity has reached a level sufficient to produce ionization of the gas. If we neglect the mixed derivative term appearing in Eq. (2.13) and assume that no plasma has been generated, then we can rescale variables by normalizing radius to the initial radius of the pulse  $r_0$ , time,  $t$ , to the Rayleigh time  $T_R = k_0 r_0^2 / (2c)$ , and time within the pulse ( $\xi / v_g = t - z / v_g$ ) to the pulse duration  $Z_L / c$ . This leaves two dimensionless parameters on which the solution depends, the normalized coefficient of GVD,  $\beta_N = \pi^2 \beta_2 r_0^2 / Z_L^2$ , and the excess peak power normalized to the critical power,  $\varepsilon \equiv P_{\max} / P_{cr} - 1$ . There is also an implicit dependence on the initial shape of the pulse and the location of the vacuum focus. In our studies, we consider Gaussian pulses which are unfocused ( $t_0 = 0$  in Eq. (2.31)). Since the coefficient of the normalized GVD is small, we expect it to be

effective in arresting focusing only for peak powers slightly above the critical power  $\varepsilon \ll 1$ .

Plots of the peak intensity on axis, normalized to the initial peak intensity, as a function of normalized time  $t/T_R$  are shown in Fig. 2.4 for various initial parameters. The parameters correspond to three different choices of peak power ( $\varepsilon$ ),  $P_{\max} = 1.322 \times 10^{11}$ ,  $1.14 \times 10^{11}$  and  $1.057 \times 10^{11}$  W. For each power several choices of normalized dispersion ( $\beta_N$ ) are considered. For  $P_{\max} = 1.322 \times 10^{11}$  W,  $\beta_N = 0.074$ , 0.084, 0.112 and 0.126. For  $P_{\max} = 1.14 \times 10^{11}$  W,  $\beta_N = 0.011$ , 0.014, 0.017, and 0.021. And for  $P_{\max} = 1.057 \times 10^{11}$  W,  $\beta_N = 8.76 \times 10^{-4}$ ,  $1.17 \times 10^{-3}$ ,  $1.56 \times 10^{-3}$  and  $2.0 \times 10^{-3}$ . What is clear from the plot is that for small values of excess power ( $\varepsilon \ll 1$ ) only very small values of normalized dispersion are required to arrest focusing.

A heuristic argument can be made that the required value of GVD should scale as the third power of  $\varepsilon$  ( $\beta_N \sim \varepsilon^3$ ) for small  $\varepsilon$ . First, we note that for small values of  $\varepsilon$  only the central time slice with width  $\Delta\xi \sim \sqrt{\varepsilon} Z_L$  will be above the critical power and start to focus. This enhances the dispersion term by a factor  $\varepsilon^{-1}$ . Second, in order to arrest focusing, the laser amplitude only has to be reduced by a factor of order  $\varepsilon$ . This enhances the dispersion term by an additional factor of  $\varepsilon$ . Finally, for small values of  $\varepsilon$  the self-focusing proceeds slowly giving the dispersive term longer time to operate. The self-focusing time scales as  $\varepsilon^{-1/2}$ . Thus, the degree

of phase modulation will scale in the same way and the modification of the power over the longer period of time will contribute an additional factor  $\varepsilon^{-1/2}$ .

It is not easy to discern from the Fig. 2.4 whether the scaling  $\beta_N \sim \varepsilon^3$  is followed. This is because the value of  $\varepsilon$  depends sensitively on the determination of the value of the critical power. Further, the scaling of the focusing time ( $\sim \varepsilon^{-1/2}$ ) is only true asymptotically. However, if we consider the three cases producing the largest peak intensity ( $P=1.322 \times 10^{11}$  W,  $\beta_N = 7.4 \times 10^{-2}$ ,  $P=1.14 \times 10^{11}$  W,  $\beta_N = 1.13 \times 10^{-2}$ , and  $P=1.057 \times 10^{11}$  W,  $\beta_N = 8.76 \times 10^{-4}$ ), we note that the peak intensity is reached in normalized times  $t_p/T_R = 1.65$ , 3.0 and 4.75 respectively. If we assume  $t_p/T_R \sim \varepsilon^{-1/2}$  and extrapolate the two lowest power cases, we estimate  $P_{cr} = 1.0019 \times 10^{11}$  W. Based on this critical power, the values of  $\varepsilon$  and scaled values of dispersion  $\beta_N/\varepsilon^3$  are  $\varepsilon = 0.32$ , 0.14 and 0.055 and  $\beta_N/\varepsilon^3 = 2.27$ , 4.28 and 5.26 respectively. Thus, the critical value of dispersion needed to arrest self focusing scales roughly as  $\varepsilon^3$ .

Figure 2.5 shows the intensity on axis as a function of  $\xi$  for the three cases just discussed. The intensity is plotted at the times  $t/T_R = 1.82$ , 3.2 and 5.08 respectively. We note that the shapes of the pulses are similar, all showing splitting. The features of the pulse become more narrow as  $\varepsilon$  decreases as expected from the  $\xi/Z_L \sim \varepsilon^{1/2}$  scaling.

An important consequence of nonlinear focusing is the resulting self-phase modulation and broadening of the pulse spectrum. Figure 2.6 shows the power spectrum of the pulse amplitude on axis for the three cases of Fig. 2.5 and for the initial pulse amplitude. As can be seen, there is significant spectral broadening in each case. As seen in the nominal case of Fig. 2.1, the pulse nonlinearly focuses to a sharp intensity spike at  $t/T_R = 2.0$ , which, in frequency space, corresponds to a broadened spectrum distribution. At  $t/T_R = 2.4$ , the pulse splits due to GVD, the two intensity spikes are coherent. Consequently in the frequency domain the pulse spectrum has modulations spaced by the time separation,  $T_s$ , between the spikes,  $\Delta\omega = 2\pi/T_s$ .

The spectral width is enhanced for pulses just above the critical power. According to the scaling argument only the central portion of the pulse, corresponding to a time duration  $\varepsilon^{1/2}Z_L/c$ , self-focuses. This effective pulse shortening leads to a broadening of the spectrum. The amount of pulse energy that experiences this shortening is a fraction  $\varepsilon^{1/2}$  of the total pulse energy. This results in a power spectrum which is broader than would be achieved if the pulse were focused (by a lens) to the same spot size.

### 2.3.1.2 Transient ionization

Figure 2.4 predicts the increase in intensity on axis a pulse will undergo as a function of the various parameters. Depending on these parameters, this predicted intensity may exceed that level required to produce significant ionization. The

critical intensity for ionizing a gas is generally in the range  $10^{14}$  W/cm<sup>2</sup> to  $10^{16}$  W/cm<sup>2</sup>. For example, table 2.1 gives the intensities at which the rate of ionization due to tunneling is equal to the laser frequency for various gases and assuming the laser wavelength is 800 nm. Table 2.1 also shows the critical power for self focusing in one atmosphere of gas.

When the gas is ionized a plasma is created which will refract the laser pulse. This refraction usually becomes a dominant effect. Refraction is dominant for the following reason. Let us estimate the spot size  $r_c$  over which at least the first electron is ionized from the gas according to the formula  $r_c^2 = P/(\pi I_c)$ , where  $I_c$  is the critical intensity given by the first row of table I. The resulting plasma density will be roughly equal to the gas density or greater over this region. The size of the plasma region measured in collisionless skin depths is  $r_c^2/\delta^2$ , where  $\delta = c/\omega_p$ . This measure of size gives the relative importance of the transverse Laplacian on the left of Eq. (2.13) to the plasma density on the right of (2.13). The expression for the normalized spot size becomes  $r_c^2/\delta^2 = P/P_{ci}$  where  $P_{ci}$  is a power given by

$$P_{ci} = \pi I_c \delta^2 = 8.4 \times 10^{11} I_c [\text{W/cm}^2] / n_g [\text{cm}^{-3}],$$

where  $n_g$  is the gas density. Values of  $P_{ci}$  for the various gases are also shown in table I. In general  $P_{ci}$  is much less than the critical power for self-focusing due to gas nonlinearity (Note that both  $P_{ci}$  and  $P_{cr}$  scale inversely with gas density). Thus, self-focused pulses which reach sufficient intensity will generally generate plasma over a large spatial region and plasma refraction will be a dominant effect.



For our parameters (Argon at 0.41 atm) ionization occurs when the peak intensity exceeds  $5.8 \times 10^{14} \text{ W/cm}^2$ . We now consider the case of our nominal parameters with peak power equal to  $1.19 \times 10^{11} \text{ W}$  (This is only about 20% above the critical power). Figure 2.7 shows the time evolution of the on axis laser intensity. The radially integrated powers are plotted in Fig. 2.8. Figure 2.9 shows the on axis maximal electron density  $n_e$ . As shown in Fig. 2.7, after  $t/T_R = 2.0$ , the pulse nonlinearly focuses to a sharp intensity peak, at which time the gas is ionized according to Fig. 2.9. However, GVD spreads and splits the pulse, the on axis peak intensity drops very quickly. Consequently, the plasma generation is stopped.

### **2.3.1.3 Off axis guiding in the slightly higher power regime**

If the input power is increased further, different phenomena appear. Figure 2.10 shows the contour plots of the intensity when the peak input power equal  $2.28 \times 10^{11} \text{ W}$  (or about 2.3 times the critical power), where we still use the same parameters as those in Fig. 2.1. As in the previous cases, the nonlinear response of the gas induces the time slices of the pulse above the critical power to self-focus. The peak intensity increases quickly to a significant value at which time plasma is generated. Plasma is generated by the portion of the pulse in the rising edge which is just above the critical power. The high gradient plasma then refracts the body and trailing part of the pulse, as shown in Fig. 2.10(b). This refracted portion then propagates just outside the plasma region for an extended period of time. This phenomenon is a form of off axis self-guiding. The off axis guided laser pulse

propagates more than 10 m before it comes back to the axis (Fig. 2.10(c)). At that time, the laser intensity in the rising edge has become too weak to generate plasma. The pulse then splits and diffracts out of the simulation box (Fig. 2.10(d)).

The physics behind the off axis guiding phenomenon is explained in the next figure. Figure 2.11 shows the profiles of the electron density and index coefficient  $\chi$ , which is defined in Eq. (2.25), at time  $t/T_R = 0.7$  and position  $\xi = 0.0113$  cm. In this figure, just outside the plasma region, there is a potential well in the spatial distribution of  $\chi$ . The contributions to variations in  $\chi$  come from the plasma electrons and the nonlinear response of the gas. The former refracts the pulse from the axis, while the latter focuses the pulse at larger  $r$ . In the plasma region, the contribution from the plasma dominates the value of  $\chi$ , and  $\chi$  is positive. The pulse is refracted. Outside the plasma region, the contribution only comes from the nonlinear response of the gas, and  $\chi$  is negative. The pulse tends to nonlinearly focus. The balance between these two factors traps the trailing part of the pulse and it is guided in the well. The trailing part also slips slowly back in the laser frame, which is accounted for by the fact that the group velocity in the weakly ionized gas is slightly smaller than in the neutral gas. A key feature of this regime of propagation is that the central plasma region is created by ionization occurring in the leading edge of the pulse. The ionization occurs in a narrow portion of the pulse where the power is just at or slightly above the critical power for self-focusing. This portion neither diffracts nor self-focuses, propagating stably over an extended distance. The portion of the pulse which is guided off axis does not generate plasma on axis.

The evolution of the on axis intensity is plotted in Fig. 2.12. The on axis intensity exhibits two peaks. The first peak is attributable to the rising portion of the pulse which was at the critical power. The second peak is attributable to the portion of the pulse which was off axis guided, but has returned to the axis at later times when the first peak has decayed to level below which there is insufficient ionization. This trailing portion exhibits pulse splitting arrested by GVD as evidenced by Fig. 2.12. Figure 2.13 shows the radially integrated powers. The radially integrated power shows a spike on the leading edge where phase modulation and group velocity dispersion have pushed power forward in the pulse. Additionally, due to refraction some power has escaped the simulation volume. The power in the body of the pulse has not changed significantly, remaining above the critical level, until the pulse escapes at later time. However, due to refraction the pulse energy has been deflected and acquired a large radial momentum. This energy does not return to the axis.

#### **2.3.1.4 Outgoing waves in the much higher power regime**

As the input power increases further, pulse splitting and off axis guiding do not occur. The pulse behavior is dominated by plasma defocusing. Figure 2.14 shows the contour plots of laser intensity evolution for a case in which the initial profile and parameters are the same as those in the previous parts, while the peak input power is  $15.0 P_{cr}$  ( $P_{max} = 1.50 \times 10^{12}$  W). Figure 2.14 (a) shows the initial contour of the laser pulse intensity. The high intensity laser pulse collapses radially and generates a high gradient plasma column around the axis. This plasma column

then refracts the trailing part of the pulse, as shown in Fig. 2.14 (b). Shortly after (Fig. 2.14 (c)), the pulse exhibits radial striations, which in fact are outgoing waves, as we will discuss next. Figure 2.14 (d) shows the pulse energy refocusing on axis.

The radial striations of Fig. 2.14 (c) can be explained as follows. As the pulse focuses the critical intensity for ionization is exceeded over the central portion of the spatial extent of the pulse. If the ionization occurs rapidly, then this results in a frequency upshift with small change in axial wave number for the central portion of the pulse [22]. Thus, if  $\omega_0$  and  $k_0 = \omega_0/c$  are the initial frequency and wave number, the upshifted wave number  $\omega'_0$  satisfies  $\omega'_0 = \sqrt{k_0^2 c^2 + \omega_p^2} = \sqrt{\omega_0^2 + \omega_p^2}$ . The pulse energy then diffracts radially into a region of unionized gas. On encountering this radial transition in plasma density, the axial wave number and frequency do not change. Thus, the pulse acquires a radial wave number to maintain the dispersion relation with the upshifted frequency,  $k_{\perp}^2 c^2 = \omega_0'^2 - k_0^2 c^2 = \omega_p^2$ . Therefore the striations have a spatial scale of the collisionless skin depth,  $c/\omega_p$ , of the plasma region.

Figure 2.15 shows the radial profiles of the real and imaginary parts of the complex amplitude of the vector potential  $a$  at time  $t/T_R = 0.2$  and  $\xi = 0.0066$  cm. Both parts oscillate sinusoidally with radius and are out of phase by  $90^\circ$  indicating outgoing waves. The wavelength of the striations is 0.05 cm and the skin depth based

on the peak electron density ( $n_e = 4.4 \times 10^{15} \text{ cm}^{-3}$ ) is  $8.0 \times 10^{-3} \text{ cm}$  satisfying the relation  $\lambda_{\perp} = 2\pi\delta$ .

Closer examination of the process of generation of striations reveals that the electron density does not rise so fast that the frequency up-shift occurs at constant wave number. Consequently the preceding explanation is only qualitative. A consideration not treated here is the generation of a static magnetic field that can occur when electrons are ionized rapidly at all phases of laser cycle. This effect would not modify the laser propagation studied here.

The pulse refocusing  $t/T_R = 0.4$  can be clearly seen from Fig. 2.16, which shows the evolution of the radius, which contains a given percentage of the pulse energy. The average radius is defined by  $\left[ \int |a(r, \xi, t)|^2 r^3 dr d\xi / \int |a(r, \xi, t)|^2 r dr d\xi \right]^{1/2}$ . The outer curve shows that a portion of the pulse energy is lost due to refraction, while the inner portion of the pulse periodically focuses and defocuses.

### 2.3.2 Time delayed Raman response

The self-focusing studied in the previous section is due to the second order nonlinear electric susceptibility of the gas medium. There are two kinds of physical contributions to the second order nonlinear electric susceptibility. One is the essentially instantaneous nonlinear electronic response due to the distortion of the atomic electron orbits. The other is the time-delayed ( $\sim 100 \text{ fs}$ ) response to the

electric field, which accounts for the relative motion and rotation of atoms in non-spherical molecules [23], such as Nitrogen, Oxygen. The spherically symmetric atom gases, such as Argon, and Xenon, respond instantaneously to the field. For short pulses, where the time scale can be of the order of 100 fs, the time delayed Raman portion of the response should be considered in more detail.

The modified nonlinear refractive index describing both portions is given by [9]

$$\delta\varepsilon_{NL} \approx n_2 \frac{ck_0^2}{\pi} \left( \frac{mc^2}{q} \right)^2 \left[ (1-\alpha)|a(t)|^2 + \alpha \int_{-\infty}^t d\tau G(t-\tau)|a(\tau)|^2 \right], \quad (2.32)$$

where  $\alpha$  is the fractional amount of the nonlinearity due to the delayed Raman effect.

The normalized kernel function is given by

$$G(t) = \theta(t)\Omega^2 e^{-t/t_0} \frac{\sin(\Lambda t)}{\Lambda}, \quad (2.33)$$

where  $\theta(t)$  is the unit step function and  $\Lambda = \sqrt{\Omega^2 - 1/t_0^2}$ . This kernel describes a delayed response which is analogous to that of a damped harmonic oscillator. Here the parameters  $\Omega$  and  $t_0$  describe the oscillation frequency and damping time of the oscillator, and are presumably determined by properties of the gas molecules. The area under the kernel is unity. Thus, the response to a constant intensity is  $\alpha|a|^2$ , which cancels the corresponding term in the instantaneous response.

In the study of the effect of the time delayed Raman response, air is used as the propagation medium. The parameters in our simulation are selected as

$n_2 = 2.04 \times 10^{-20} \text{ cm}^2/\text{W}$ ,  $k'' = 0.2 \text{ fs}^2/\text{cm}$  at  $\lambda = 800 \text{ nm}$ , corresponding to the dimensionless parameter  $\beta_2 = 1.42 \times 10^{-5}$ . Parameters for the kernel function of Raman response are  $\alpha = 1/2$ ,  $\Omega = 20.6 \text{ THz}$ , and  $t_0 = 77 \text{ fs}$  [9]. The initial pulse profile has a duration (FWHM) of 112.5 fs, and spot size  $r_0 = 0.21 \text{ cm}$ . The important features that occur in the intensity frequently are of much shorter duration (See Figs. 2.5, 2.7, and 2.12). Thus, we can anticipate that the primary effect of the delayed response will be to decrease the nonlinearity by a factor  $(1 - \alpha)$ . That is, the delayed response can be ignored. With the given value of  $\alpha \cong 1/2$ , the net effect is to double the critical power. For our parameters the critical power including the delayed response (long pulses) is  $P_{cr} = 4.99 \times 10^{10} \text{ W}$ . If we neglect the delayed response (short pulse)  $P_{cr} \cong 1.0 \times 10^{11} \text{ W}$ .

As an example, we consider a case where the peak input power is  $P_{\max} = 3.87 \times 10^{11} \text{ W}$ . This is about 3.87 times the short pulse critical power. Figure 2.17 shows the contour plots of the laser intensity at time  $t/T_R = 0.5$ , where the initial laser profile is Gaussian. The Phenomena of off axis guiding and pulse splitting, similar to those seen in Figs. 2.10-2.13 are observed. The same feature is also observed at half the input power when  $\alpha = 0$ . When the peak input power increases further, as before, radial filaments are observed. Figure 2.18 shows the contours of laser intensity at  $t/T_R = 0.15$ . The initial Gaussian pulse has a peak input power of

$1.85 \times 10^{12}$  W. If we do not consider the Raman response ( $\alpha = 0$ ), the same feature, outgoing waves, is observed at half the input power.

## 2.4 Chapter Summary

In this chapter, we have numerically studied the propagation of high power, initially large spot size, laser pulses in tenuous gases. Propagation is affected by gas ionization, plasma defocusing, nonlinear self-focusing and group velocity dispersion (GVD). The instantaneous electronic response and time delayed Raman response of the gas are also considered. The propagation properties have been studied at different input power levels. For peak input power near the critical power for nonlinear self-focusing, the pulse behavior is dominated by nonlinear self-focusing and GVD. No plasma or very tenuous plasma is generated in this regime. The nonlinear response of the gas makes the pulse self-focus very quickly, however, it is effectively stopped by GVD. Group velocity dispersion spreads the pulse, lowers the power, and arrests the self-focusing collapse. For moderate input power, plasma is generated and plasma defocusing overwhelms GVD. The peak region of the pulse is refracted due to the high gradient of plasma. The trailing part of the pulse is then trapped just outside the plasma region, and it can be off axis guided for a remarkably long distance. For higher input power, the pulse behavior is dominated by plasma defocusing. However, part of the pulse is initially trapped in the plasma. Filaments then appear as pulse energy is refracted from the plasma and interference with the part of the laser pulse not trapped occurs. At higher levels of power we can expect three dimensional effects [24] to be important. These will be studied in more detail in the future.



Table 2.1: Critical intensities for ionization and critical powers for self focusing

	Helium	Nitrogen	Argon	Xenon
$I_1(\text{W}/\text{cm}^2)$	$4.67 \times 10^{15}$	$5.07 \times 10^{14}$	$5.79 \times 10^{14}$	$2.15 \times 10^{14}$
$I_2(\text{W}/\text{cm}^2)$	$2.76 \times 10^{16}$	$1.82 \times 10^{15}$	$1.23 \times 10^{15}$	$5.05 \times 10^{14}$
$I_3(\text{W}/\text{cm}^2)$		$4.91 \times 10^{15}$	$2.36 \times 10^{15}$	$1.29 \times 10^{15}$
$I_4(\text{W}/\text{cm}^2)$		$1.90 \times 10^{16}$	$5.81 \times 10^{15}$	$2.84 \times 10^{15}$
$I_5(\text{W}/\text{cm}^2)$		$3.25 \times 10^{16}$	$8.90 \times 10^{15}$	$3.60 \times 10^{15}$
$I_6(\text{W}/\text{cm}^2)$			$1.32 \times 10^{16}$	$5.34 \times 10^{15}$
$I_7(\text{W}/\text{cm}^2)$			$3.41 \times 10^{16}$	$1.40 \times 10^{16}$
$I_8(\text{W}/\text{cm}^2)$			$4.82 \times 10^{16}$	$1.05 \times 10^{16}$
$P_{ci}(\text{W})$	$1.47 \times 10^8$	$1.59 \times 10^7$	$1.82 \times 10^7$	$6.75 \times 10^6$
$P_{cr}(\text{W})$	$1.05 \times 10^{12}$	$4.24 \times 10^{10}$	$4.48 \times 10^{10}$	$5.60 \times 10^9$

Remark:

1. The critical intensity  $I_j (j = 1, 2, \dots)$  is the intensity at which the ionization rate of the  $j$ th electron due to tunneling equals the laser frequency.
2.  $P_{ci} = \pi I_1 \delta^2$  where  $\delta$  is the skin depth for singly ionized gas.
3. Calculation of the critical intensity and powers is based on 1 atm of gases and wavelength  $\lambda = 0.8 \text{ cm}$ .

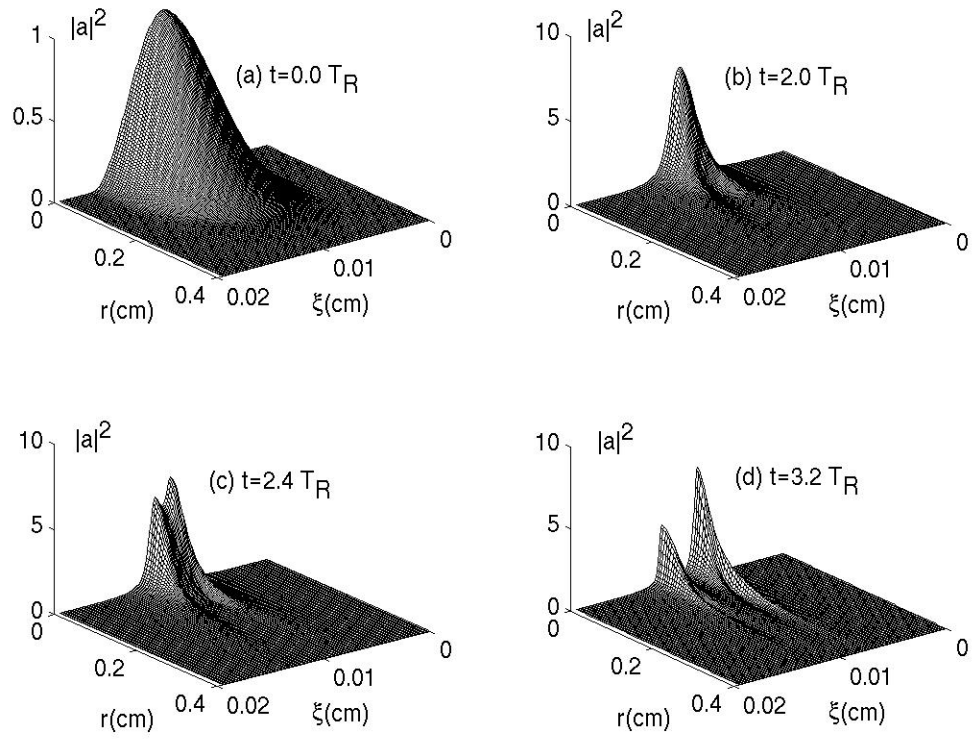


Figure 2.1: Time evolution of the normalized laser intensity. The peak input power

$P_{\max} = 1.14 \times 10^{11}$  W, spot size  $r_0 = 0.21$  cm, and pulse length  $Z_L = 135$  cm.

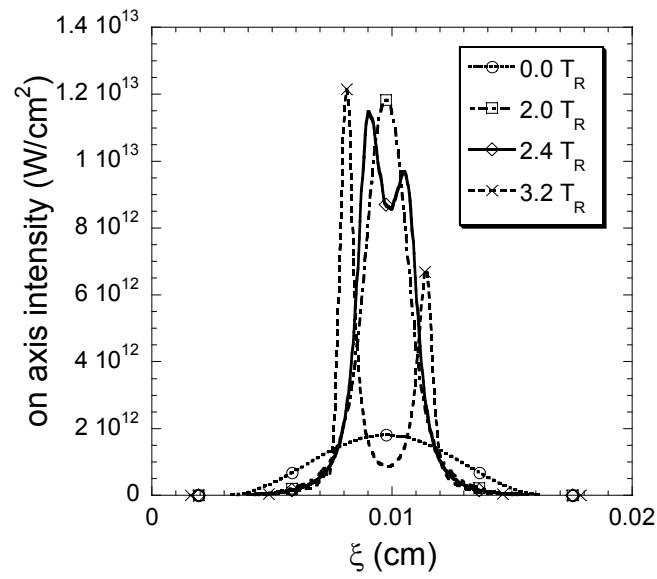


Figure 2.2: Plots of the on axis intensity as function of  $\xi$  for the case of Fig. 2.1.

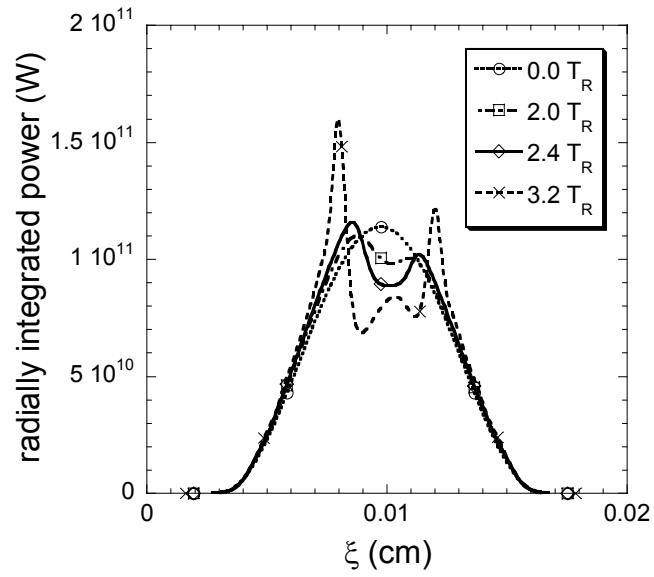


Figure 2.3: Distribution of the radially integrated power for the case of Fig. 2.1.

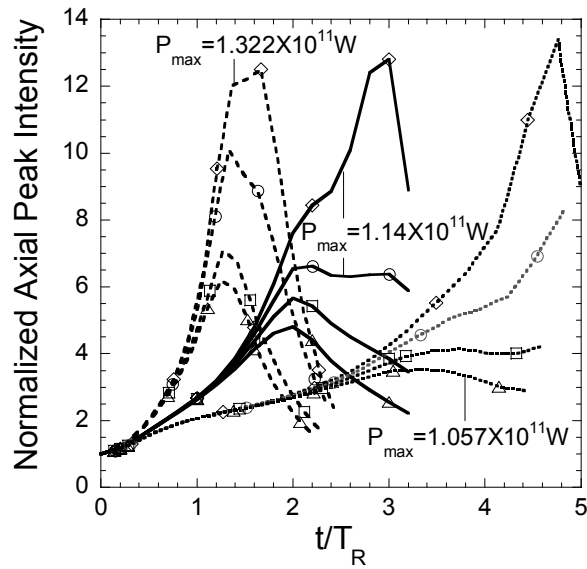


Figure 2.4: Plots of the peak intensity on axis, normalized to the initial peak intensity, as a function of normalized time  $t/T_R$  for various initial parameters. The peak input powers associated with the solid, dashed, and dotted lines are  $1.14 \times 10^{11}$  W,  $1.322 \times 10^{11}$  W, and  $1.057 \times 10^{11}$  W respectively. The normalized coefficient,  $\beta_N$ , for the solid lines with diamond, circle, square, and triangle, are 0.011, 0.014, 0.017 and 0.021, for the dashed lines with the same marks in order, are 0.074, 0.084, 0.112 and 0.126, and for the dotted lines in the same order, are  $8.76 \times 10^{-4}$ ,  $1.17 \times 10^{-3}$ ,  $1.56 \times 10^{-3}$  and  $2.0 \times 10^{-3}$  respectively.

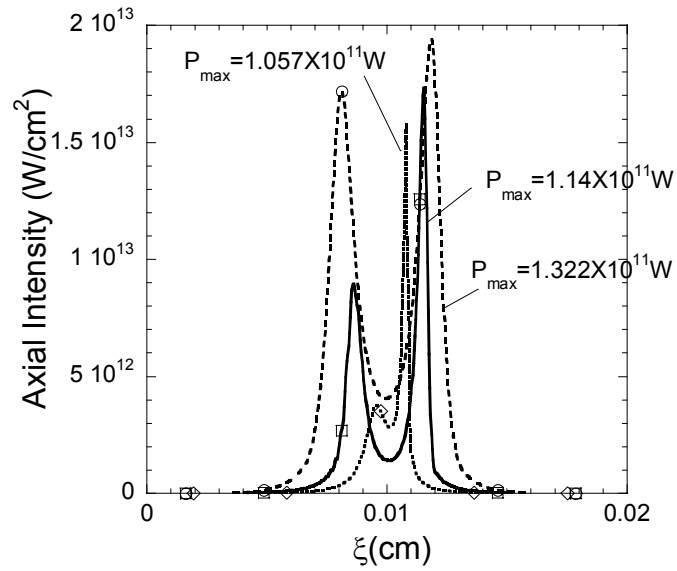


Figure 2.5: Plots of the axial intensity versus  $\xi$  at the given time. The peak input power  $P_{\max}$ , normalized coefficient  $\beta_N$ , and normalized time  $t/T_R$ , are  $1.14 \times 10^{11}$ , 0.011, and 3.2 for the solid line,  $1.322 \times 10^{11}$  W, 0.074, and 1.82 for the dashed line,  $1.057 \times 10^{11}$ ,  $8.76 \times 10^{-4}$ , and 5.08 for the dotted line respectively.

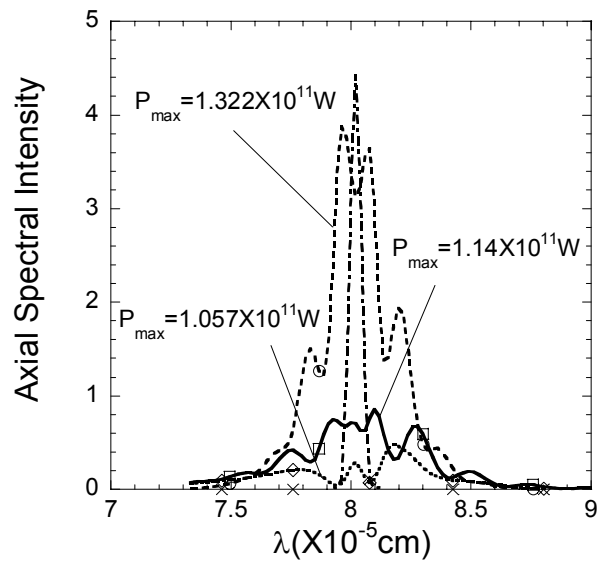


Figure 2.6: Plots of the normalized spectral intensity on axis. Parameters correspond to those of Fig. 2.5. The dash-dotted line is the initial spectrum ( $t/T_R = 0$ ) with the same parameters as the solid line.

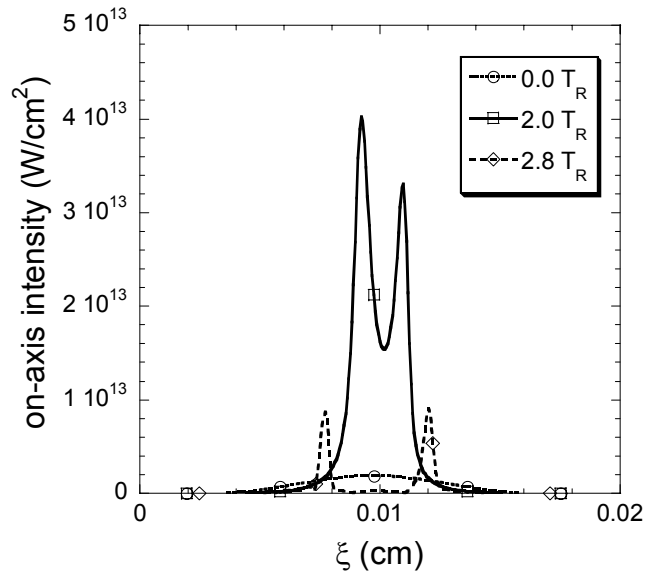


Figure 2.7: Time evolution of the on axis intensity for  $P_{\max} = 1.19 \times 10^{11}$  W,  $r_0 = 0.21$  cm, and  $Z_L = 135$  cm.



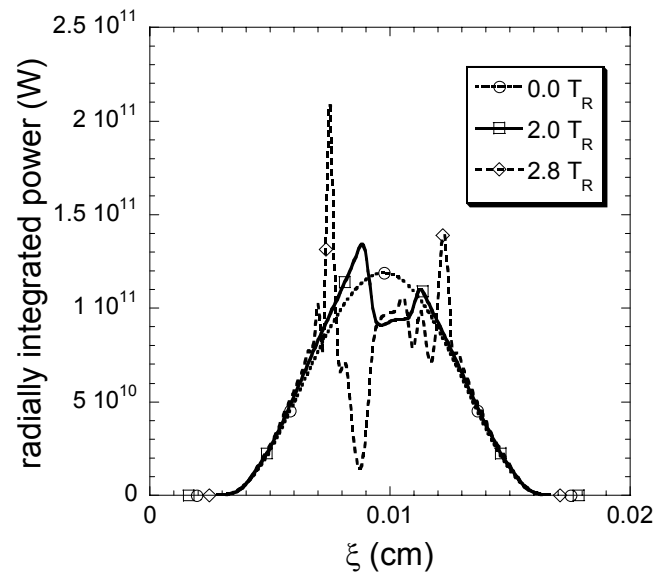


Figure 2.8: Distribution of the radially integrated power as function of  $\xi$  (same case as Fig. 2.7).

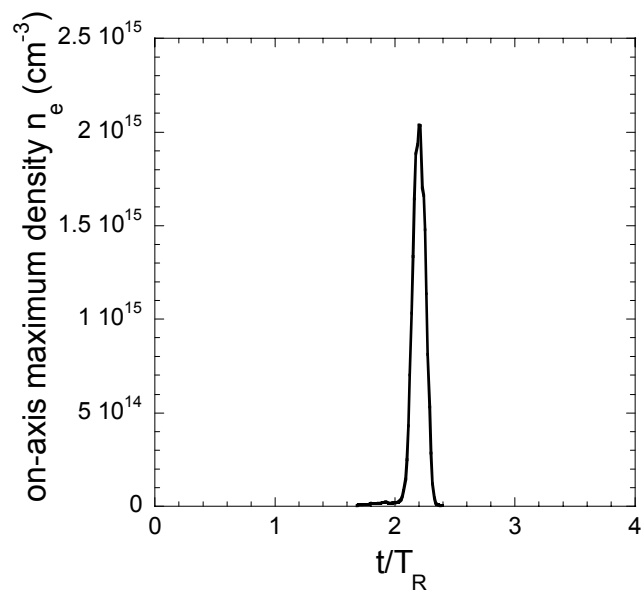


Figure 2.9: On-axis maximal electron density as function of time (same case as Fig. 2.7).

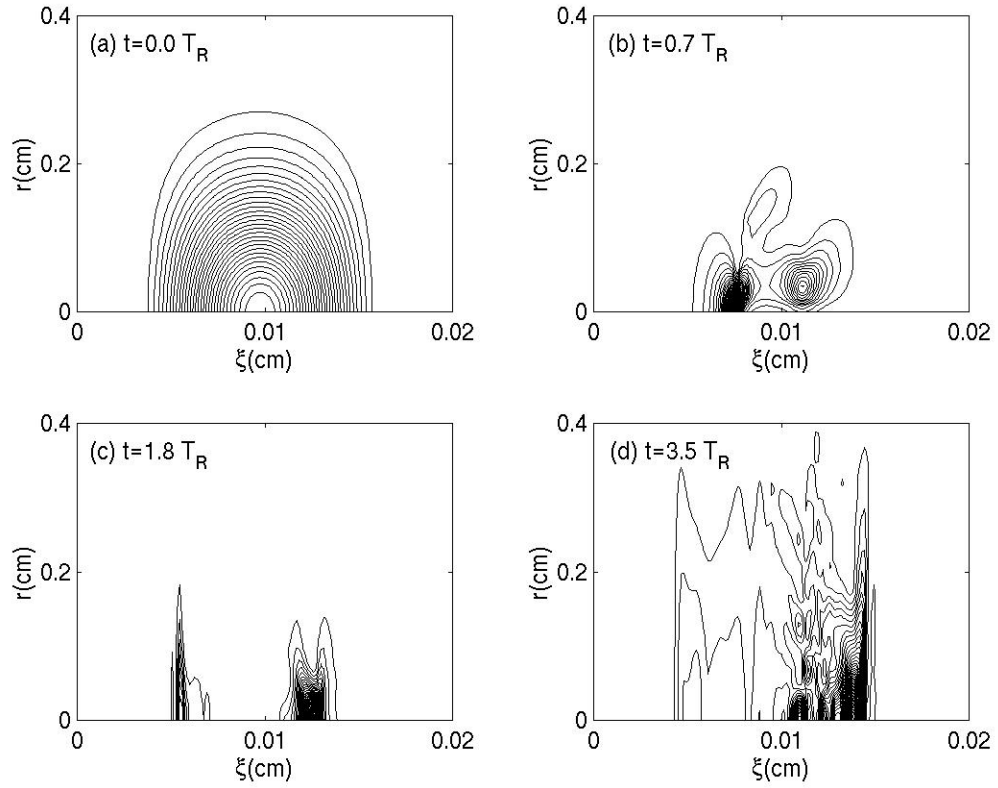


Figure 2.10: Contour plots of the laser intensity over time with the peak input power

$P_{\max} = 2.28 \times 10^{11}$  W. The spot size and pulse length are of the same as Fig. 2.1.

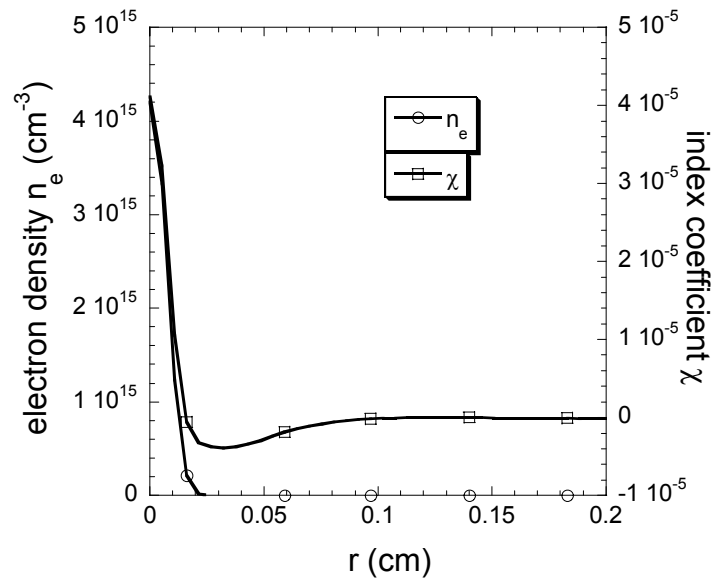


Figure 2.11: Radial profiles of the electron density and index coefficient  $\chi$  at

$t/T_R = 0.7$  and  $\xi = 0.0113$  cm (same case as Fig. 2.10).

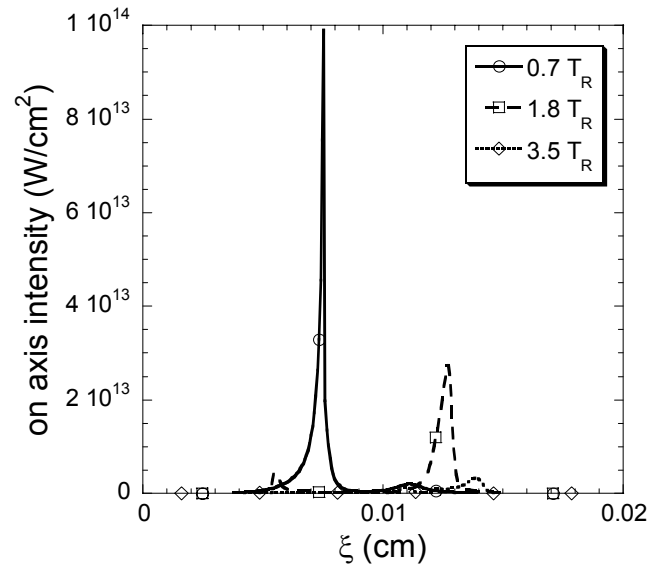


Figure 2.12: Evolution of the on axis intensity (same case as Fig. 2.10).

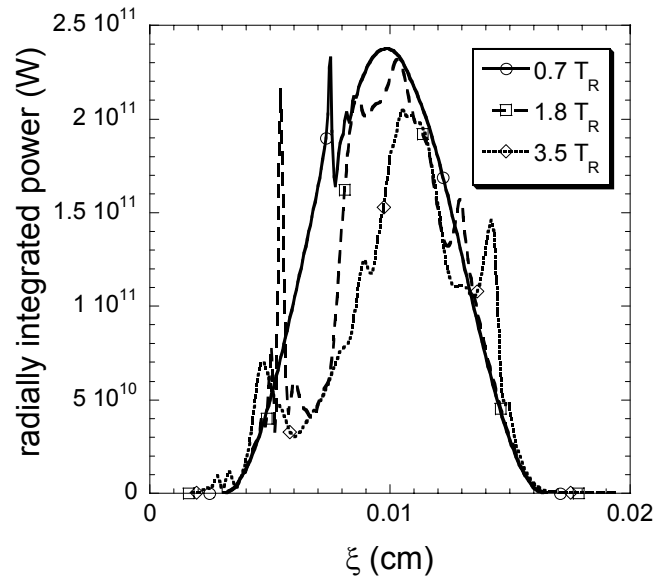


Figure 2.13: Distribution of the radially integrated power as function of  $\xi$  for the case of Fig. 2.10.

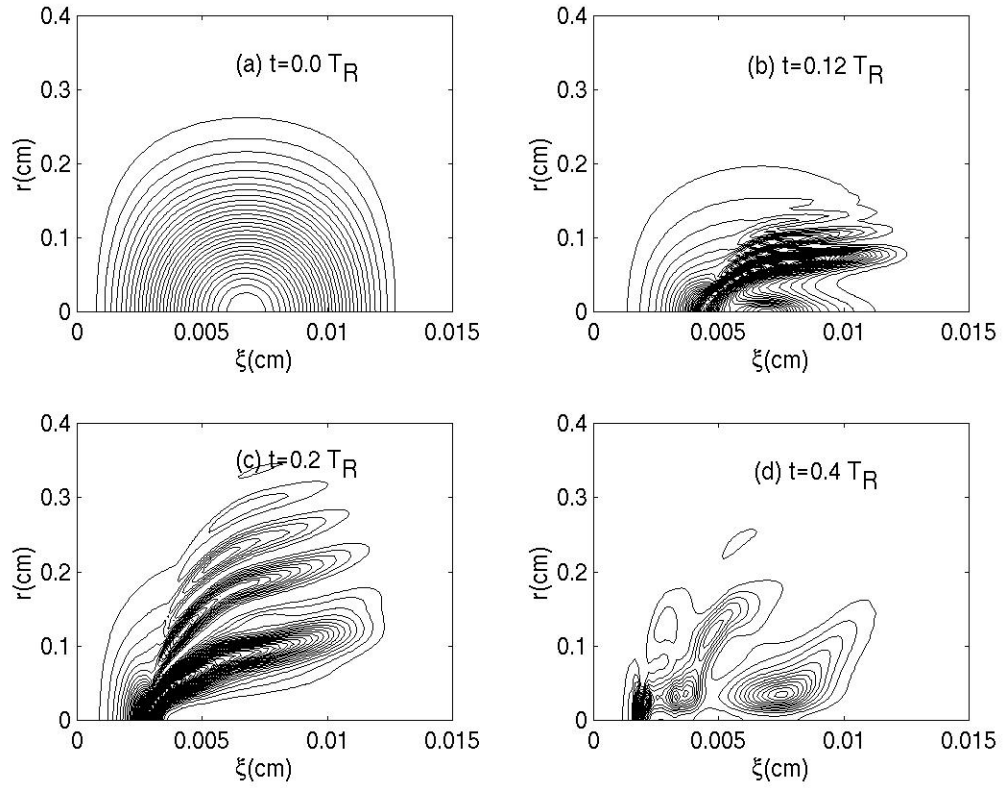


Figure 2.14: Contour plots of the laser intensity over time with the peak input power

$P_{\max} = 1.5 \times 10^{12}$  W, spot size  $r_0 = 0.21$  cm, and pulse length  $Z_L = 135$  cm.

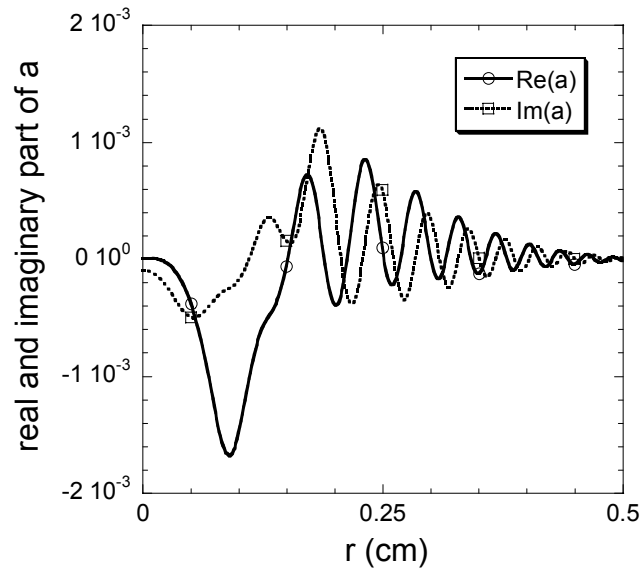


Figure 2.15: Radial profiles of the real and imaginary parts of the complex amplitude of the vector potential  $a$  at  $t/T_R = 0.2$  and  $\xi = 0.0066$  cm for the case of Fig. 2.14.



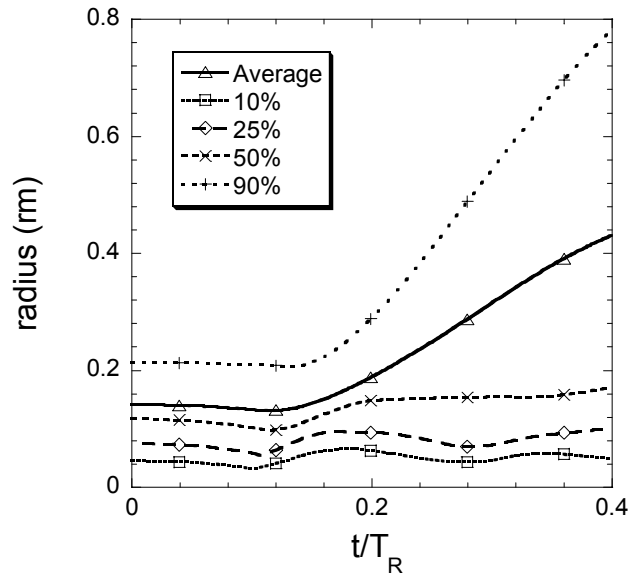


Figure 2.16: Evolution of the radii containing specified fractions of the pulse energy as function of time (same case as Fig. 2.13). The percentage numbers are of the total pulse energy contained within that radius. The average radius is defined by

$$\left[ \frac{\int |a(r, \xi, t)|^2 r^3 dr d\xi}{\int |a(r, \xi, t)|^2 r dr d\xi} \right]^{1/2}.$$

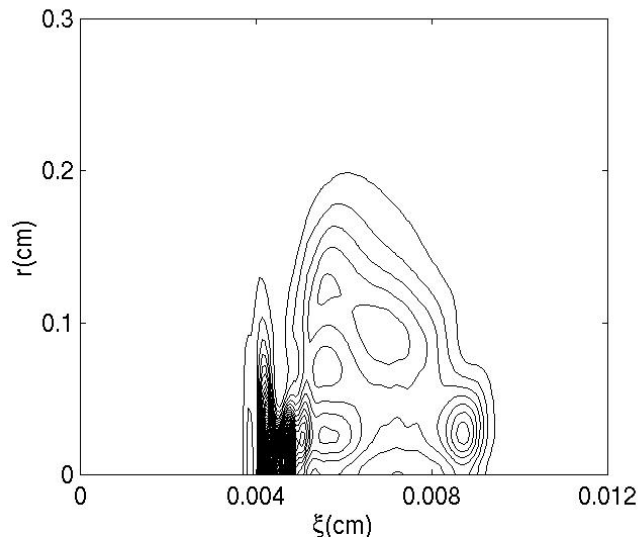


Figure 2.17: Contour plots of the laser intensity in air at  $t/T_R = 0.5$  after considering time delayed Raman response. The input parameters are  $P_{\max} = 3.87 \times 10^{11}$  W,  $r_0 = 0.21$  cm, and  $Z_L = 67.5$  cm.

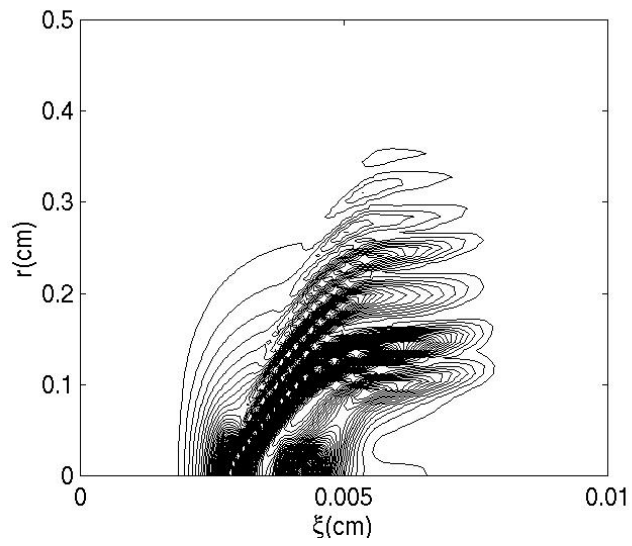


Figure 2.18: Contour plot of the laser intensity in air at  $t/T_R = 0.15$  after considering time delayed Raman response with the initial peak power  $P_{\max} = 1.85 \times 10^{12}$  W, spot size  $r_0 = 0.21$  cm, and pulse length  $Z_L = 67.5$  cm.

# Chapter 3: Spectrum Broadening of Laser Pulses Propagating in Tenuous Gases

## 3.1 Introduction

Propagation of an ultra short, high intensity, high power laser pulse in a nonlinear medium can lead to a super-broadened pulse spectrum [1-10]. This broadening, known as supercontinuum generation, covers the visible range and may even extend to the near infrared and ultraviolet bands [4]. It was first observed in dense media [1]. Similar observations in high-pressure gases were reported later [6,7,9]. Supercontinuum radiation is used to generate tunable ultrafast light pulses, which are needed in ultrafast spectroscopic studies [1], optical pulse compression [1], and optical parametric amplification [11]. Various mechanisms have been suggested to explain this phenomenon. Among them are nonlinear self-phase modulation (SPM) [1,4,5], four wave mixing [2], and plasma generation [3,8]. But none of these factors alone gives a complete description of the evolution of the spectrum. In fact, these mechanisms are strongly coupled.

A laser pulse propagating through a medium induces a time dependent polarization of the atoms or molecules in the medium. At sufficiently low intensity the polarization is proportional to the laser field and is described by the relative dielectric constant  $\epsilon$  which may depend on laser frequency. At higher intensity the polarization becomes a nonlinear function of the laser field. When the medium

responds rapidly on the time scale of the envelope of the laser field, the response can be characterized by a nonlinear dielectric constant  $\epsilon_{NL} = \epsilon(1 + 2n_2I)$ , where  $n_2$  is the coefficient of the nonlinear refractive index and  $I$  is the laser intensity. The nonlinearity in the medium's response modifies the laser pulse characteristics. One effect is that the phase of the laser pulse is modified in a time and space dependent way by the profile of the laser intensity. This is known as self-phase modulation. Since the modulation of the phase is time dependent, new frequency components are generated in the pulse and the spectrum is broadened. The transverse profile of the intensity results in a spatially dependent phase modulation, which distorts the wave fronts, and is responsible for the phenomena of nonlinear self-focusing. On focusing, the pulse shrinks in both spatial and temporal dimensions [12], and the peak intensity increases quickly. This leads to further SPM. Thus, it is not surprising that the threshold power for spectral super broadening coincides with the critical power for nonlinear self-focusing [10].

When the peak intensity increases over the ionization threshold, plasma is generated. Plasma contributes phase changes in two ways. First, it introduces an index change, which is proportional to the free electron density. Secondly, by refracting the pulse, plasma modifies the transverse intensity profile, and affects the intensity-dependent refractive index. Self-phase modulation introduces a chirp. For  $n_2 > 0$  the front of the pulse is red shifted and the back is blue shifted. If group velocity dispersion (GVD) is present, the pulse shape will then change. In the case of positive GVD, the red shifted portions run ahead and the blue shifted portions fall

behind. This spreads and splits the pulse in time and modifies the intensity-dependent refractive index. Generally, all of these factors are intensively coupled for high power laser beams. To have a complete understanding of super broadening, we should consider these mechanisms simultaneously.

In this chapter we study the effect of the initial pulse parameters on the spectral broadening. Pulse propagation is studied numerically using the simulation code WAKE [13], which solves the two dimensional, cylindrically symmetric, envelope wave equation for the laser pulse. The propagation model includes group velocity dispersion (GVD), self-phase modulation, self-focusing due to the second order nonlinear response of the gas, and plasma generation due to multi-photon and tunneling ionization [8,14]. The goal of this research is to study these competing effects and determine the laser parameters for which each effect is dominant.

This chapter is organized as following. Section 3.2 gives our theoretical model describing the envelope equation for laser propagation. The effective refractive index is also discussed in this section. In section 3.3, we discuss the asymmetric spectrum broadening in the regime of critical power for nonlinear self-focusing. Plasma induced blue shift in higher input power regime is discussed in section 3.4. And finally a conclusion is given in section 3.5.

### 3.2 Theoretical Model

In the frame moving with group velocity  $v_g$ , the envelope wave equation describing the laser pulse propagation is [15]

$$2\frac{\partial}{\partial z}\left(ik_0 - \frac{\partial}{\partial \xi}\right)a - \beta_2 \frac{\partial^2 a}{\partial \xi^2} + \nabla_{\perp}^2 a = -k_0^2 \delta \varepsilon a, \quad (3.1)$$

where  $a$  is the dimensionless complex amplitude of the vector potential, which is normalized to  $mc^2/q$ . To obtain Eq. (3.1), we assume that the high frequency part of the vector potential varies as  $e^{i(k_0 z - \omega_0 t)}$ ,  $k_0$  is the laser wavenumber, and  $\omega_0 = k_0 c$ . The quantity  $\xi = v_g t - z$  is the distance back from the head of the pulse. Group velocity dispersion is described by the dimensionless coefficient  $\beta_2 = \omega_0 c k''$ , which is evaluated at the central frequency  $\omega_0$ . The perturbation of the dielectric constant on the right hand side of Eq. (3.1) is given by

$$\delta \varepsilon = -\frac{k_p^2}{k_0^2} \left( 1 + \frac{\delta n}{n_0} - \frac{1}{2} |a|^2 \right) + 2n_2 I, \quad (3.2)$$

which describes the contributions from the time and space varying plasma density ( $n_e = n_0 + \delta n$ ), relativistic self focusing ( $-|a|^2/2$ ) and nonlinear self focusing due to the neutral gases ( $2n_2 I$ ). Here  $n_2$  is the second order nonlinearity coefficient of the gas. The plasma wave number is given by  $k_p^2 = \omega_p^2 / c^2 = 4\pi q^2 n_0 / (mc^2)$ , where  $n_0$  is the ambient electron density.  $I = (c/2\pi) |\omega m c a / q|^2$  is the laser intensity. The ambient electron density  $n_0$  is determined by the rate of ionization of the gas atoms in

the laser field. In the laser frame, the evolution of the electron density as well as the density of the various ionization stages of the gas atoms is given by [15],

$$c \frac{\partial}{\partial \xi} n_{g,i} = v_i(a) n_{g,i-1} - v_{i+1}(a) n_{g,i}, \quad (3.3)$$

$$c \frac{\partial}{\partial \xi} n_e = \sum_{i=1}^Z v_i(a) n_{g,i-1}. \quad (3.4)$$

where  $n_{g,i}$  is the density of gas atoms which have been ionized  $i$  times, and  $v_i(a)$  is the rate at which the  $i$ th electron is ionized. Both multi-photon [14] and tunneling [8] ionization are considered in our model. The perturbed density due to the excitation of plasma waves is given by [15]

$$c \frac{\partial}{\partial \xi} \delta n - \frac{\partial}{\partial \xi} n_0 v_z + \frac{1}{r} \frac{\partial}{\partial r} r n_0 v_r = 0, \quad (3.5)$$

$$mc \frac{\partial}{\partial \xi} n_0 v_r = n_0 \left( -q \frac{\partial}{\partial r} \phi - \frac{mc^2}{2} \frac{\partial}{\partial r} |a|^2 \right), \quad (3.6)$$

and

$$mc \frac{\partial}{\partial \xi} n_0 v_z = n_0 \left( q \frac{\partial}{\partial \xi} (\phi - A_z) + \frac{mc^2}{2} \frac{\partial}{\partial \xi} |a|^2 \right). \quad (3.7)$$

where  $v_r$  and  $v_z$  are the radial and axial fluid velocities, which are assumed to be first order in the laser intensity. The electromagnetic field of the wake is generated by the scalar potential  $\phi$  and magnetic vector potential  $A_z$ . The wake fields are determined by the axial and radial components of Ampere's law

$$-\frac{1}{r} \frac{\partial}{\partial r} r \frac{\partial A_z}{\partial r} = \frac{4\pi}{c} q n_0 v_z + \frac{\partial^2}{\partial \xi^2} (\phi - A_z), \quad (3.8)$$

and



$$-\frac{\partial^2 A_z}{\partial r \partial \xi} = \frac{4\pi}{c} q n_0 v_r - \frac{\partial^2 \phi}{\partial r \partial \xi}. \quad (3.9)$$

Equation (3.1) accounts for second order GVD, axial flow of laser power, transverse diffraction, ionization, plasma defocusing, relativistic self-focusing and nonlinear self-focusing. In the case the input power is greater than the critical power for nonlinear self-focusing ( $P_{cr} = \lambda^2 / (2\pi n_0 n_2)$ , where  $n_0$  is the linear index of refraction) [16], the unlimited focusing can lead the pulse to a singularity. It can be overcome by the group velocity dispersion, which spreads and splits the pulse in time, thus reduces the peak intensity, or by the plasma defocusing in space, if the intensity is high enough for ionization.

In the following sections, the initial laser profile is chosen as,

$$a(r, \xi, z=0) = \frac{a_{\max}}{(1-i z_0/Z_R)} \exp\left(-\frac{r^2}{r_0^2(1-i z_0/Z_R)}\right) \sin\left(\frac{\pi \xi}{Z_L}\right), \quad (3.10)$$

where  $a_{\max}$  is the maximum amplitude, and  $r_0$  is the spot size that would be achieved in vacuum at the focus,  $z_0$  is the distance to the vacuum focus, and  $Z_R = k_0 r_0^2 / 2$  is the Rayleigh length. The temporal profile of the pulse envelope is taken to be a half sine wave with full width at half maximum of the intensity equal to  $Z_L/2c$ . The typical parameters we consider are as follows. The laser wavelength  $\lambda$  is 800 nm and the spot size at incidence is fixed at 0.21 cm. The pulse duration  $Z_L/c$  is chosen to be 450 fs, the corresponding full widths at half maxima (FWHM) is 225 fs. The medium is uniformly distributed 311.6 torr of Argon, with nonlinear coefficient

$n_2 = 2.275 \times 10^{-20} \text{ cm}^2/\text{W}$  for 760 torr of Argon. For  $\lambda = 800 \text{ nm}$ , the quantities in Eq. (3.1) are  $k'' = \partial^2 k / \partial \omega^2 = 0.083 \text{ fs}^2/\text{cm}$ , and  $\beta_2 = 5.87 \times 10^{-6}$ . Therefore, the corresponding GVD is normal. The constant  $a_{\text{max}}$  will be varied so that phenomena corresponding to different input powers can be studied.

### 3.3 Nonlinearity Induced Red Shift

To study the effect of the initial pulse parameters on the spectral broadening, we fix the initial laser spot size to be 0.21 cm, and vary the distance to focus  $z_0$  and the vacuum spot size  $r_0$  in Eq. (3.10). The peak input power is fixed and the laser pulses propagate the same distance for all the cases. Figure 3.1 shows the evolution of the average radius, defined by  $\left[ \int |a(r, \xi, t)|^2 r^3 dr d\xi / \int |a(r, \xi, t)|^2 r dr d\xi \right]^{1/2}$ , versus the propagation distance  $z$  for three cases, where  $z_0$  is the distance the pulse travels until vacuum focus reached,  $r_0$  is the corresponding waist. In each case, the input power is fixed at  $1.14 \times 10^{11} \text{ W}$ , which is about 14 percent higher than the critical power for nonlinear self-focusing in 311.6 torr of Argon [15]. In the case  $r_0 = 0.21 \text{ cm}$ , self-focusing is arrested by the positive GVD [15]. For the other two cases with smaller waists at vacuum focus, higher peak intensities are obtained due to the focusing, which leads to ionization, as shown in Fig. 3.2, where the evolution of the on axis maximum electron density is plotted for these three cases. There is no plasma generation for the case  $r_0 = 0.21 \text{ cm}$ , but there is weak ionization and plasma

generation for the other two cases, in which the focusing is stopped by plasma refraction.

The on axis intensity at  $z = 27.71$  m for the three cases is shown in Fig. 3.3. For the case  $r_0 = 0.21$  cm, there is no linear focusing of the pulse. However, the nonlinear response of the gas causes the pulse to self-focus initially, the pulse then spreads and splits due to GVD (see Ref [15]). Its intensity has a rather smooth profile in time. For the other two cases, the combination of the nonlinear response of the gas and the linear focusing causes the pulse to form a sharp intensity spike. Group velocity dispersion has little effect due to the rather small value of the coefficient  $\beta_2$ . This is in contrast to the  $r_0 = 0.21$  cm case where the focusing is due just to the nonlinearity, and because the power is only slightly above the critical power the focusing is arrested by GVD. The sharp increase in intensity eventually ionizes the gas in the two linearly focusing cases. Plasma then refracts the pulse following the spike. The peak intensity for the case  $r_0 = 0.0939$  cm is already very small at  $z = 27.71$  m, this is because the pulse has focused and experienced plasma defocusing at an earlier time, as can be seen in Fig. 3.1. Comparatively, the peak intensity for the case  $r_0 = 0.1878$  cm is still high at  $z = 27.71$  m.

Due to the intensity redistribution in time and space, both the intensity induced phase change  $\delta\phi_{NL}$ , and plasma induced phase change  $\delta\phi_{plasma}$  are modified from what would be predicted based on linear propagation. These quantities, along

with their sum  $\delta\phi$ , evaluated at  $z = 27.71$  m are plotted in Fig. 3.4(a), Fig. 3.4(b) and Fig. 3.4(c) respectively. The dashed, solid, and dotted lines correspond to the case  $z_0 = 0.0$  m,  $r_0 = 0.21$  cm, the case  $z_0 = 6.93$  m,  $r_0 = 0.1878$  cm, and the case  $z_0 = 6.93$  m,  $r_0 = 0.0939$  cm respectively. In Fig. 3.4(a), the non-focusing case ( $r_0 = 0.21$  cm) has a very smooth phase distribution, since GVD arrests the nonlinear self-focusing before the pulse can focus to a sharp spike, the nonlinear refractive change has a rather smooth profile. On the other hand, the other two cases exhibit sharp intensity spikes. The corresponding refractive index changes have similar rough profiles, and hence the phase changes have larger gradients. The phase change is accumulated over propagation distance. The sharp spike for the strong focusing case ( $r_0 = 0.0939$  cm) occurs earlier and lasts a short time, while the intensity spike for the weak focusing case ( $r_0 = 0.1878$  cm) increases relatively slowly, so that the refractive index change is maintained over a longer distance. That is why the weak focusing case has stronger phase shift variation compared with the strong focusing case. No ionization occurs in the case  $r_0 = 0.21$  cm. So in Fig. 3.4(b), there is no plasma induced phase change. The plasma induced phase change for the weak focusing case has a stronger variation in  $\xi$  than for the strong focusing case, because the strong focusing case has a shorter plasma duration, as shown in Fig. 3.2. The sum of the intensity induced and plasma induced phase change is plotted in Fig. 3.4(c). The non-focused case has a rather smooth profile. Therefore, its frequency shift will be the smallest among these three cases. The slight focusing case ( $r_0 = 0.1878$  cm),

on the other hand, has the largest variation on both the leading and trailing edges of its phase change profile, and this will result in the largest frequency shifts.

Figure 3.5 shows the normalized intensity induced and plasma induced frequency shift, and their sum, for the case of weak focusing ( $r_0 = 0.1878$  cm). Since the ionization front occurs after the intensity spike, in the leading edge of the pulse, we observed red shifted components early. The maximum is about  $0.7\omega_0$ . Following the spike, both the nonlinearity and the plasma contribute blue shifted components. The combination yields a net blue shift with a maximum about  $1.2\omega_0$ .

The on axis spectral intensity, obtained by Fourier transforming the complex envelope of the laser pulse, at  $z = 27.71$  m is plotted in Fig. 3.6. The weak focusing case has the broadest spectrum. For positive GVD ( $k'' > 0$ ), it is red shift at the leading edge and blue shift at the trailing edge [17]. Figure 3.6 considers all of the aforementioned contributions.

Generally, supercontinuum generation is associated with an input power higher than the critical power for nonlinear self-focusing. However, if the power is only slightly above the critical power and the coefficient of GVD is large enough to arrest self-focusing, the pulse maintains a smooth profile, and the frequency shift will not be prominent. If the coefficient of GVD is so small that it cannot stop nonlinear self-focusing, the pulse exhibits a sharp intensity spike, followed by ionization and plasma refraction. The corresponding frequency shift has large red and blue

components. The most broadening occurs when the initial intensity spike grows most slowly. For fixed spot size and pulse energy, varying the focusing angle can dramatically affect the output spectrum.

### 3.4 Plasma Induced Blue Shift

When the input power increases to a higher level ( $=2.28P_{cr}$ ), the nonlinear response of the gas causes the pulse to focus to a sharp spike in its leading edge. This leads to ionization for all of the three cases of focusing angle discussed previously. Figure 3.7 shows the evolution of the on-axis maximum electron density for the three cases. The strong focusing case experiences ionization earlier compared with the other two cases. Upon ionization, the plasma density increases quickly, and ionization induced plasma defocusing dominates the propagation. As a result, the on-axis laser intensity decreases, which in turn weakens the ionization process, as shown by the first density wedge in each case of Fig. 3.7. Since the central portion of the pulse still has a power higher than the critical power, the laser pulse refocuses on-axis after the ionization stops, as indicated by the second peak in the electron density. This is further demonstrated by Fig. 3.8, which shows the contours of laser intensity at  $z = 27.71$  m for the case  $r_0 = 0.21$  cm. The trailing edge of the pulse has an intensity spike high enough to trigger ionization, which leads to the second density wedge associated with each curve in Fig. 3.7.

Figure 3.9 plots the on-axis nonlinear phase change (dashed line), plasma induced phase change (dotted line), and their sum (solid line) at  $z = 27.71$  m for the case  $r_0 = 0.21$  cm. The trailing intensity spikes in Fig. 3.8 account for the second bump in the dashed line. The dotted line has two steps. The first step is associated with ionization at the leading edge, as shown by the first density wedge in Fig. 3.7. When the pulse refocuses at later time, only the trailing spike reaches intensity high enough to generate plasma. So the second downward step is located in the trailing edge, and is associated with the second electron density wedge in Fig. 3.7. The step depth is proportional to the area under the electron density curve of Fig. 3.7. The time derivative of the phase change yields the local frequency shift, as shown in Fig. 3.10. The sharp second downward step in plasma induced phase change in Fig. 3.9 corresponds to a large blue shift in Fig. 3.10, as shown by the highest peak of the dotted line. The largest blue shift of the pulse, peaked at  $1.74 \omega_0$ , is a contribution of both the peak of the plasma induced blue shift and the peak of the nonlinear blue shift. The nonlinear response of the gas makes a contribution to the red components, peaked at both the leading and trailing intensity spikes.

Figure 3.11 compares the local frequency shifts for these three cases. They have similar distributions. However, the case  $r_0 = 0.0939$  cm has a smaller peak blue shift than the other two cases. This is partially due to the relatively smaller area under its density curve in Fig. 3.7, compared with the areas of the other two cases. The image of the spectral intensity as a function of radius at  $z = 27.71$  m is shown in Fig. 3.12 for the most broadened case  $r_0 = 0.21$  cm. The striations in the wavelength

are the result of the coherence between the intensity spikes in time domain. The spectrum extends from the near infrared to the ultraviolet bands. The maximum blue shift is determined not only by the maximum value of the electron density, but also the distance over which the plasma extends. The higher the value the electron density can reach, and the greater the distance the plasma extends, the larger the value the plasma induced phase.

### 3.5 Chapter Summary

In this chapter, we have numerically studied the spectral broadening of laser pulses propagating in tenuous gases. Several factors affect the spectral broadening. Among them are self-phase modulation, nonlinear self-focusing, plasma generation, and group velocity dispersion. In tenuous gases, self-phase modulation, coupled with nonlinear self-focusing, accounts for the near infrared spectrum in the critical power regime. However, if group velocity dispersion arrests the nonlinear self-focusing at an earlier time, spectrum broadening will be limited. At higher input power, plasma generation introduces blue shifted components. The maximum blue shift is determined by both the maximum value of the electron density, and the distance over which the plasma extends.



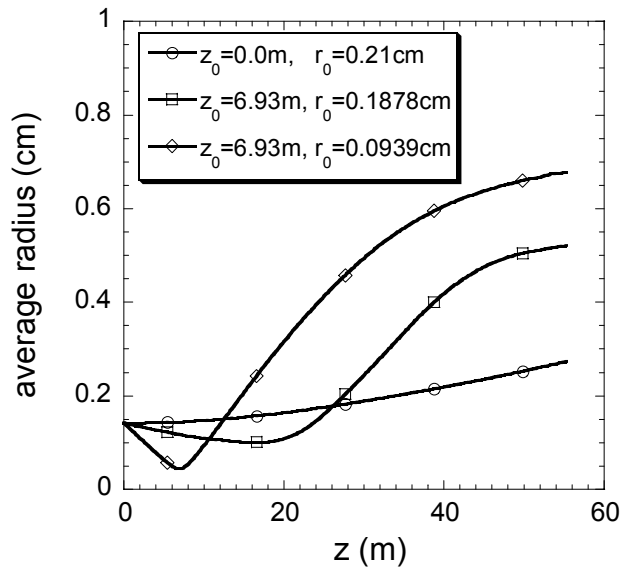


Figure 3.1: Evolution of the average radius versus the propagation distance  $z$ , where  $z_0$  and  $r_0$  are the vacuum focusing location and the corresponding waist. The

average radius is defined by  $\left[ \frac{\int |a(r, \xi, t)|^2 r^3 dr d\xi}{\int |a(r, \xi, t)|^2 r dr d\xi} \right]^{1/2}$ .

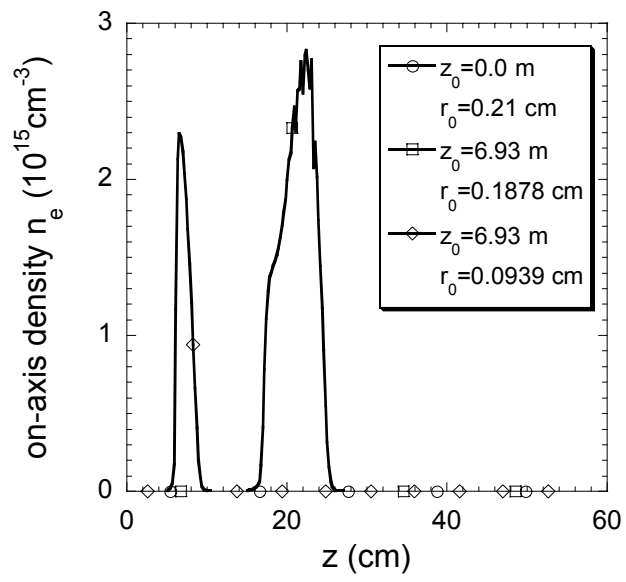


Figure 3.2: Evolution of the on-axis maximum electron density.

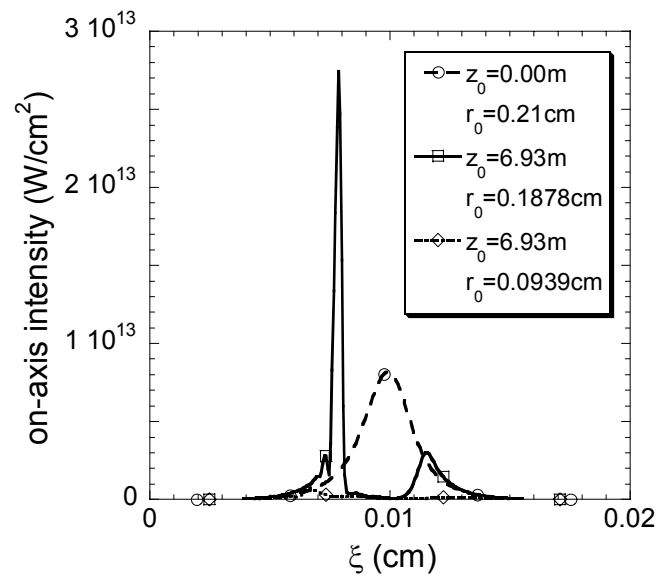


Figure 3.3: On-axis intensity distribution in the laser frame at  $z = 27.71$  m.

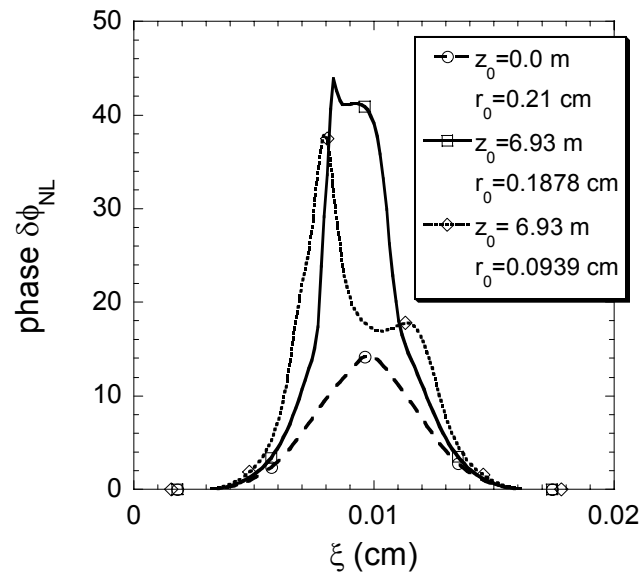


Figure. 3.4 (a): Nonlinearity-induced phase changes at  $z = 27.71$  m. The dashed, solid, and dotted lines correspond to the case  $z_0 = 0.00$  m,  $r_0 = 0.21$  cm, the case  $z_0 = 6.93$  m,  $r_0 = 0.1878$  cm, and the case  $z_0 = 6.93$  m,  $r_0 = 0.0939$  cm respectively.

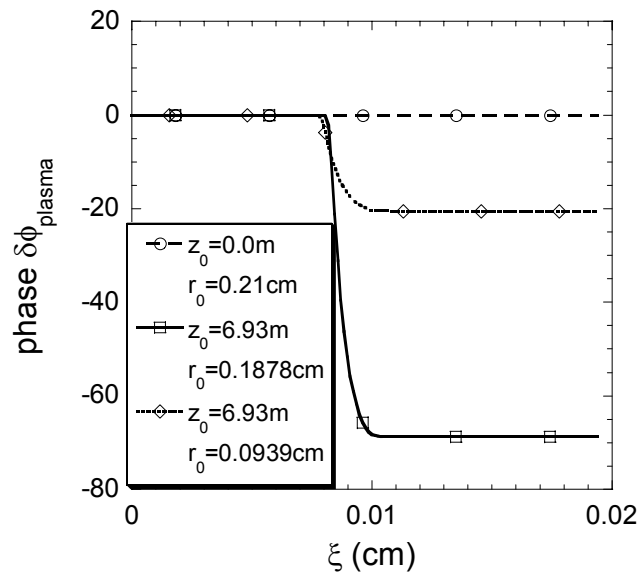


Figure. 3.4 (b): Plasma-induced phase changes at  $z = 27.71$  m. The dashed, solid, and dotted lines correspond to the case  $z_0 = 0.00$  m,  $r_0 = 0.21$  cm, the case  $z_0 = 6.93$  m,  $r_0 = 0.1878$  cm, and the case  $z_0 = 6.93$  m,  $r_0 = 0.0939$  cm respectively.

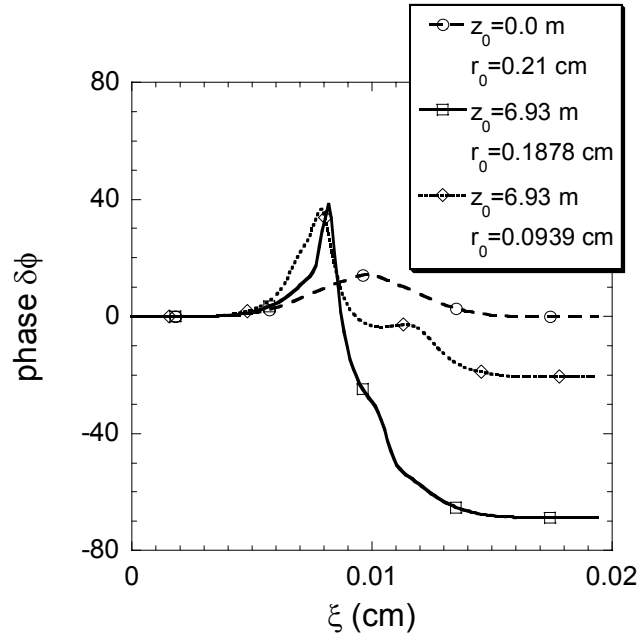


Figure. 3.4 (c): The sum of the nonlinearity-induced and the plasma-induced phase changes at  $z = 27.71$  m. The dashed, solid, and dotted lines correspond to the case  $z_0 = 0.00$  m,  $r_0 = 0.21$  cm, the case  $z_0 = 6.93$  m,  $r_0 = 0.1878$  cm, and the case  $z_0 = 6.93$  m,  $r_0 = 0.0939$  cm respectively.

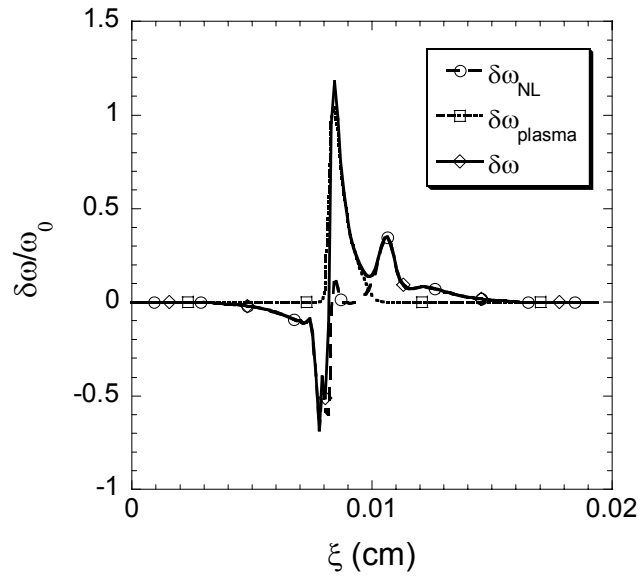


Figure 3.5: Normalized nonlinearity-induced (circle), plasma-induced (square) instantaneous frequencies and their sum (diamond) at  $z = 27.71$  m for the case  $z_0 = 6.93$  m,  $r_0 = 0.1878$  cm.

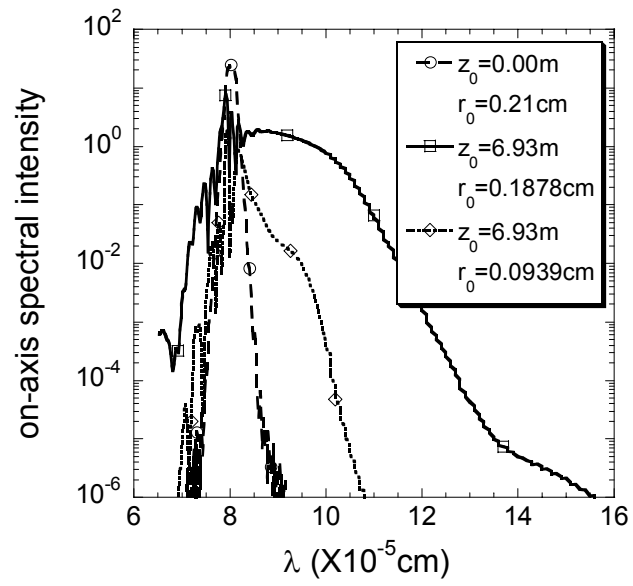


Figure 3.6: On-axis spectral intensity for the previous three cases at  $z = 27.71$  m.

The slight focusing case (solid line) has the most broadening spectrum compared with the tight focusing case (dotted line) and non-focusing case (dashed line).



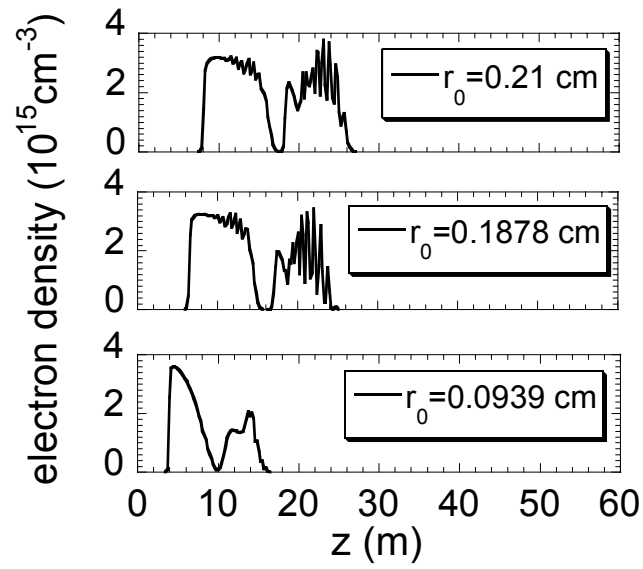


Figure 3.7: Evolutions of the maximum on-axis electron density when the input power increases to  $2.28 P_{cr}$ .

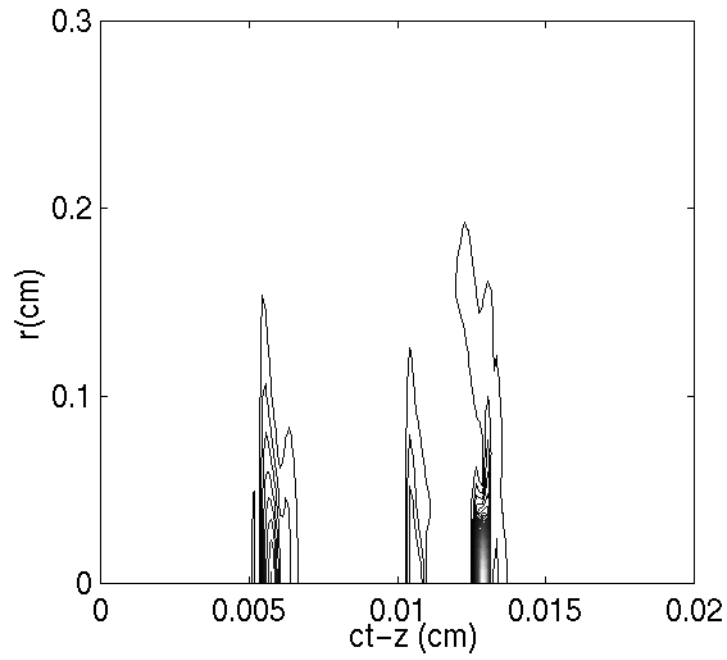


Figure 3.8: Contour of the laser intensity at  $z = 27.71$  m for the case  $r_0 = 0.21$  cm with input power  $P_{in} = 2.28P_{cr}$ . Pulse refocus at the trailing edge.

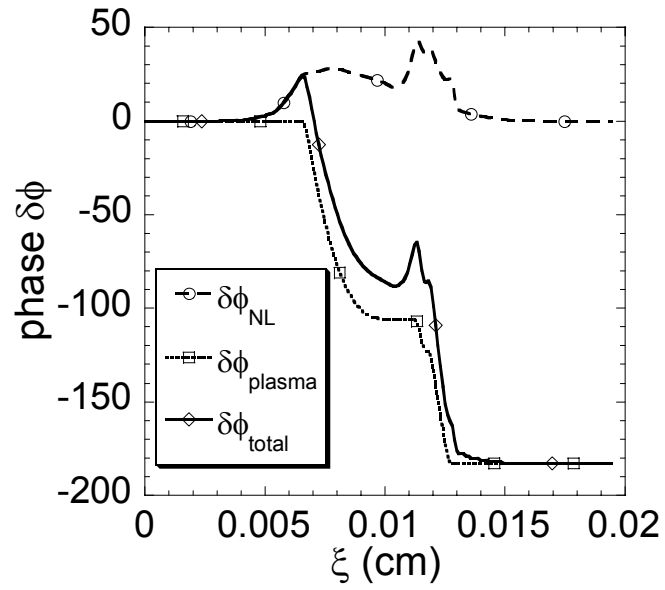


Figure 3.9: Distributions of the nonlinear phase change (dashed line), plasma induced phase change (dotted line), and the summation of them (solid line) at  $z = 27.71$  m for the case  $r_0 = 0.21$  cm with  $P_{in} = 2.28P_{cr}$ .

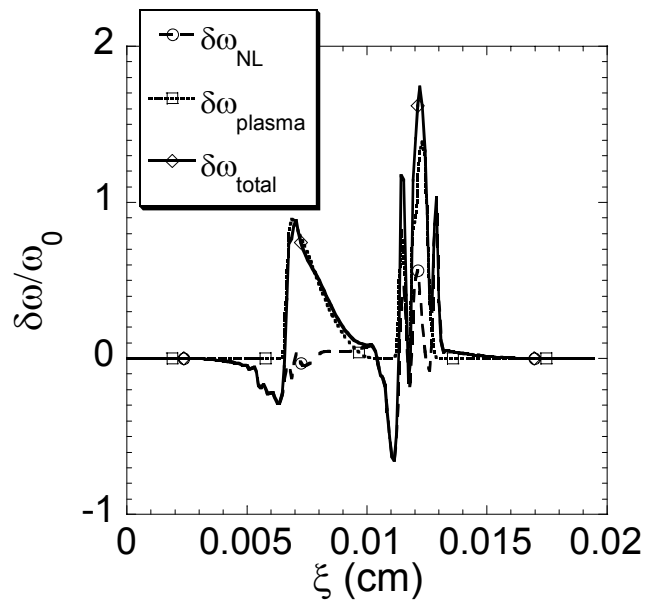


Figure 3.10: Distributions of local nonlinear frequency (dashed line), plasma induced frequency (dotted line), and the summation of them (solid line) according to Fig. 3.9.

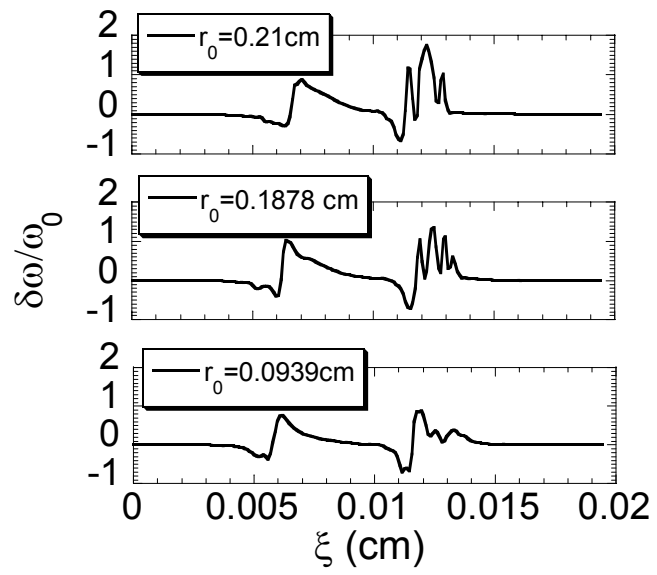


Figure 3.11: Local frequency changes at  $z = 27.71$  m when input power is  $2.28 P_{cr}$ .

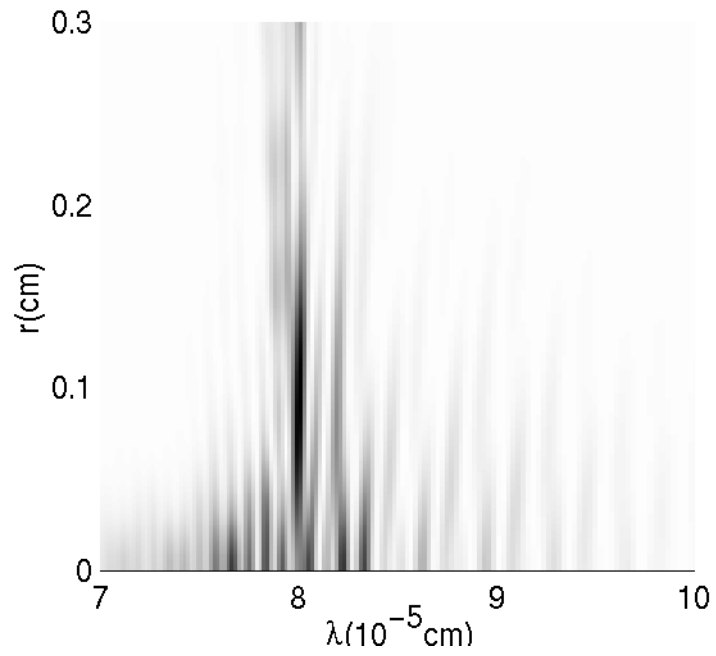


Figure 3.12: Image of spectral intensity at  $z = 27.71$  m for the case  $r_0 = 0.21$  cm when input power is  $2.28 P_{cr}$ .

# Chapter 4: Effective coupling of ultra-intense laser pulse to funnel-mouthed plasma waveguides

## 4.1 Introduction

The optical guiding of intense laser pulses has many applications, such as x-ray lasers [1], laser wake-field electron accelerators [2] and harmonic generation. Guiding of pulses is needed in these applications so as to prolong the interaction of the laser with the propagation medium. Several approaches to guiding have been studied. One approach is to use the natural self-focusing that occurs in a nonlinear medium with a positive second order refractive index. Such a nonlinearity can arise from the response of bound electrons in the atoms of a neutral gas, or from free electrons that are quivering relativistically. A second approach is to create some sort of guiding structure that confines radiation to the interaction region. Examples include high voltage capillary discharges [3], gas filled capillaries [4], and plasma channels created by thermally driven plasma expansion [5-10]. In the last approach, a waveguide formation pulse is line-focused into backfill [5-7] or gas jet targets [8-10]. Channels formed in this way have been investigated extensively and found to be effective in guiding radiation over many Rayleigh lengths [5-7].

The coupling efficiency for guiding in a preformed channel in backfill is reported to be 70% for moderate intensity ( $<10^{15}$  W/cm<sup>2</sup>) [5], and 30% for higher

intensity ( $5 \times 10^{15}$  W/cm<sup>2</sup>) [6]. Waveguide propagation of a pulse at  $\sim 10^{17}$  W/cm<sup>2</sup> is reported in a channel preformed in gas jet clustered gases [10]. Injection of pump pulses with intensity  $> 10^{17}$  W/cm<sup>2</sup> into axicon formed waveguides is hindered by poor coupling of the laser pulse to the waveguide entrance in both gas jet and backfill gases [6,8]. The poor coupling is a result of both waveguide taper at the entrance (the channel radius decreases as the end of the channel is approached) and ionization induced refraction of the laser pulse there. One potential solution to this problem is to “graft” a plasma funnel onto the preformed waveguide using an auxiliary formation pulse [10]. This funnel formation pulse can precede or follow the waveguide generation pulse such that different funnel shapes can be selected. This “grafted” funnel eliminates the neutral gas near the channel entrance and provides a focusing element to funnel the high intensity laser pulse into the channel [10].

The dynamics of laser pulse propagation in gases is affected by diffraction and refraction. Moreover, if the peak intensity is large enough, plasma is generated, which causes a decrease in the refractive index, and refracts the pulse itself. To study the effective coupling of an ultra-short pulse into a funnel-mouthed channel, we consider in our model transverse diffraction, ionization, plasma induced refraction, relativistic self-focusing, and nonlinear self-focusing, as described in Ref. [11]. The vehicle for our studies is the simulation code WAKE which solves the two dimensional  $(r, z)$  time dependent scalar wave equation for the complex envelop of the laser field. Included in the code are modules which calculate self-consistently the



ionization of the plasma, the generation of plasma waves by the ponderomotive force, and the nonlinear modification of the dielectric constant of the background gas.

As mentioned we study the coupling process using the simulation code WAKE [12] by examining the coupling efficiency of laser pulses to funnel-mouthed guiding channels of a variety of shapes in both backfill and gas jet Helium. The initial profiles for the waveguide and funnel are generated using the waveguide formation code of Milchberg et al. [13]. This code determines time dependent radial profiles of electron and ion density and temperature. The rate of production of electrons and ions is calculated based on rate equations for tunneling and collisional ionization. The self-consistent absorption of the formation laser pulse is also determined based on profiles of electron and ion density and temperature. Parameters of the channel can be varied by varying the gas density, the formation pulse intensity, and the timing between the formation pulse and the injected pulse. The electron and ion densities taken from the formation code are then modeled with simple formulas that capture their essential features. This information is imported to WAKE, which then simulates the propagation of the short pulse laser. Properties of the funnel are generated by taking the model formulas for the channel and allowing the parameters to vary with axial distance. In this way we determined the requirements for the funnel.

Basically, we find that effective coupling can be most easily achieved in gas jet targets. This is because ionization induced refraction is so strong, that

unreasonably long entrance funnels (1~2 cm) are required in backfill targets. In gas jet targets the entrance funnel only needs to extend the short distance (1~2 mm) between the channel and edge of the gas jet to achieve high coupling efficiency.

The remainder of this chapter is organized as following. Section 4.2 gives the simulation parameters and illustrates a funnel and channel profile for a gas jet target. In section 4.3, we study the dependence of the coupling efficiency on the funnel parameters for a gas jet target. We make a similar study in section 4.4 for a backfill target. And finally in section 4.5, conclusions are summarized.

## 4.2 Laser Parameters And Funnel-Mouthed Channel Profiles

An elongated gas jet can produce longitudinally uniform gas puffs over its orifice. By focusing a formation laser pulse through an axicon to the gas puffs, one can produce a longitudinally uniform channel. Channel profiles from the 1D hydrodynamic formation code [13] are displayed in Fig. 4.1. Displayed as solid lines are the electron density  $n_e$ , and  $\text{He}^+$  and  $\text{He}^{+2}$  ion densities at  $t = 0.7$  ns. The channel formation laser pulse has a wavelength  $1.064 \mu\text{m}$ , duration 150 ps (FWHM), and peak intensity  $1.0 \times 10^{14} \text{ W/cm}^2$ , which is focused into 550 torr Helium through an axicon at an approach angle of  $15^\circ$ . As can be seen there is an expanding shock wave that has propagated out to a radius of  $30 \mu\text{m}$ , and makes a wall with thickness of about  $4 \mu\text{m}$ . The electron density at the center of the channel for  $t = 0.7$  ns is about  $1.75 \times 10^{19} \text{ cm}^{-3}$ , and reaches peak density  $3.25 \times 10^{19} \text{ cm}^{-3}$  at  $r = 30 \mu\text{m}$ . The channel

is almost fully ionized, with very low  $\text{He}^+$  density at the channel center. The  $\text{He}^{+2}$  density profile is quite flat with a drop-off inside the channel wall. The dashed lines in Fig.4.1 are fits to the solid lines that will be used in subsequent WAKE simulations.

Even though the gas density is uniform in the puff, at the edges, a drop in gas density occurs, creating a density ramp [8]. Since the collisional ionization rate is proportional to the density squared, it is difficult for the formation laser pulse to generate efficient ionization throughout this region. The neutral gas that remains in this region then hinders the entering of the injected pulse into the channel. Figure 4.2 shows radial profiles of electron and ionized Helium densities for the case of channel formed in 275 torr of Helium, which would correspond to a point in the middle of the density ramp. The same laser parameters are used as in Fig. 4.1. Here we have made the assumption that the heating and shock generation processes can be treated as being one dimensional in radius with parameters that vary with axial distance. This approximation should be valid as long as the radial size of the channel and the electron mean free path are much less than the density ramp scale length. We note that the channel radius is smaller in Fig. 4.2 than in Fig. 4.1 indicating that the plasma waveguide will taper to a close at the edge of the gas jet. In addition the center of the channel region in Fig. 4.2 is not fully ionized. Thus, a laser pulse entering the gas jet through this channel will have to further ionize the gas and be refracted in the process.

To “graft” a funnel onto the channel in the gas density ramp, an auxiliary Gaussian laser pulse is focused in this region. Figure 4.3 shows (again as solid lines) the funnel profile at the middle of the density ramp for this case. The auxiliary pulse, which leads the channel formation pulse by 0.7 ns, has a duration 100 ps (FWHM) and peak intensity  $2.5 \times 10^{14}$  W/cm<sup>2</sup>. The funnel wall expands to 45 μm at the same time as the channel has attained the parameters of Fig. 4.1. We can see that there are still significant amounts of singly ionized Helium in the funnel region, which results from the low initial gas density. This gas will be further ionized when an ultra-intense laser pulse is injected into the funnel. However, now there is a channel with a tapered opening that will counteract the effects of refraction.

The density profiles from Figs. 4.1, 4.2 and 4.3 will be modeled with simple formulas, as shown as dashed lines in the figures. These are density profiles used in our pulse propagation simulation. The preformed channel (Fig. 4.1) is defined by an inner radius (30 μm) and an outer radius (34 μm). From the axis to half the inner radius (15 μm), the transverse electron density is constant, then increases parabolically up to the inner radius (30 μm), and afterward drops linearly to zero at the outer radius (34 μm). The density of He<sup>+</sup> is flat up to half of the inner radius, then parabolically increases to the inner radius, from the inner to the outer radius it linearly drops to zero. The He<sup>+2</sup> density profile is flat initially, then parabolically decreases to zero at  $r = 25 \mu\text{m}$ .

To model a funnel at the end of the channel we take the radial profile of the electron density to have the basic form of Fig. 4.3, that is, the funnel is also described by two radii. However, rather than keep these parameters fixed, as in the channel region, we allow them to vary with axial distance. Figure 4.4 shows the variation of both radii as a function of axial distance  $z$ . They both parabolically decrease as axial distance increases from the funnel mouth ( $z = -0.1$  cm) to the channel entrance ( $z = 0.0$  cm). They remain constant in the channel region. For the inner radius (solid line), this parabolic curve is determined by three points, the inner radius at the channel entrance ( $z = 0.0$  cm), which is  $30 \mu\text{m}$  read from Fig. 4.1, the inner radius at the middle of the funnel ( $z = -0.05$  cm), which is  $45 \mu\text{m}$  read from Fig. 4.3, and the inner mouth radius at funnel mouth ( $z = -0.1$  cm), which is an adjustable input parameter ( $60 \mu\text{m}$  in this case). The curve of outer radius (dashed line) has a similar determination. Both the inner mouth radius and the outer mouth radius are adjustable in the WAKE simulations, and coupling will be optimized with respect to these variables.

We also model the axial profiles of the densities by using data from Fig. 4.1 and Fig. 4.3. Figure 4.5 shows the on-axis density profiles of neutral gas, electrons,  $\text{He}^+$ , and  $\text{He}^{+2}$  ions. The gas density starts at  $z = -0.1$  cm, linearly increases with axial distance to  $z = 0.0$  cm, and is constant afterward, with gas density ramp of the length of 1 mm as measured in the experiment [8]. The plasma channel shown in Fig. 4.1 is produced in this longitudinally uniform region ( $z > 0$  cm). Correspondingly, the on-axis electron density is constant in this region. In the funnel region

( $-0.1 \text{ cm} \leq z \leq 0 \text{ cm}$ ), the on-axis electron density increases smoothly to the channel density at the channel entrance ( $z = 0.0 \text{ cm}$ ). Its profile is modeled by  $n_e(z) = x \cdot n_0^{x+f(1-x)}$ , where  $n_0 = 1.75$  is the on-axis electron density inside the channel in the units of  $10^{19} \text{ cm}^{-3}$  (Fig. 4.1), the normalized axial distance is  $x = (z + L)/L$ , where  $L = 0.1 \text{ cm}$  is the length of the ramp. The constant factor  $f$  ( $f = 0.45$  in this case) is adjustable so that at the middle of the ramp, the on-axis electron density approaches  $0.65 \times 10^{19} \text{ cm}^{-3}$  (Fig. 4.3). The ionization rate increases with gas density, so in the funnel region, we let the  $\text{He}^{+2}$  density parabolically increase. This parabolic curve is determined by zero density at the funnel mouth ( $z = -0.1 \text{ cm}$ ), the density  $0.225 \times 10^{19} \text{ cm}^{-3}$  at the middle ramp (Fig. 4.3), and the density  $0.87 \times 10^{19} \text{ cm}^{-3}$  at the channel entrance (Fig. 4.1). The on-axis  $\text{He}^+$  density is extracted from the electron density and the  $\text{He}^{+2}$  density by considering the particle number conservation law. In this figure, the plasma funnel coincides with the gas density ramp. In our simulation, we can adjust the funnel location such that we can deal with more general cases, where the funnel may start somewhere in the ramp, such that some neutral gas is still left in front of the funnel.

We show a surface plot of electron density for a funnel mouthed channel in Fig. 4.6. The parameters describing the variation of funnel and channel are given in Fig. 4.1, 4.3, 4.4 and 4.5. The funnel mouth radius is two times the channel radius, as demonstrated by Fig. 4.4. The length of both the funnel and the gas density ramp is fixed to  $0.1 \text{ cm}$ . Its radial channel profile is shown in Fig. 4.3, and the on-axis density

profile in Fig. 4.5. For comparison, we also show a surface plot of a tapered channel corresponding to the situation of a single formation pulse in Fig. 4.7. Its on-axis and radial density profiles in the tapered region are extracted from Fig. 4.1 and Fig. 4.2 in the same way as was done for the funnel mouthed channel. The only difference is that both the inner and the outer radii parabolically increase from zero to the channel radii, so that the end of the channel is closed.

### 4.3 Gas Jet Target

We first consider the case of injection of a laser pulse into the channel in the absence of a funnel. The radial profiles of density that are selected correspond to Fig. 4.1 in the channel and Fig. 4.2 at half way point in the density ramp. The profiles are jointed as described in the previous section. The resulting electron density profile in the  $r-z$  plane is illustrated in Fig. 4.7. The injected Gaussian laser pulse has a duration 100 fs (FWHM), peak power  $7.0 \times 10^{11}$  W, and a spot size at vacuum focus of 15  $\mu\text{m}$ . Figure 4.8 shows the total energy (solid lines) and pulse radius (dotted line) as a function of propagation distance  $z$ . The radius is defined as the one through which a given percentage of the energy passes. As can be seen, at the beginning of the uniform channel ( $z = 0.0$  cm), only about 25% of the laser energy passes through a radius of 20  $\mu\text{m}$ . In Fig. 4.8 we compare the energy evolution when the plasma wave is on (solid line with circles) with that when the plasma wave is off (solid line with squares), we see that the energy loss is not due to the excitation of the plasma wave. Rather, energy is lost because the laser pulse energy is refracted outside the

channel where it leaves the simulation domain through the radial boundaries. The averaged peak intensity that is achieved on axis in this case is  $1.61 \times 10^{17} \text{ W/cm}^2$ . In comparison, the peak intensity that is obtained in vacuum for these laser parameters is  $2.09 \times 10^{17} \text{ W/cm}^2$ .

To see the beneficial effects of the funnel, we next consider a case, where radial profiles corresponding to Figs. 4.1 and 4.3 are jointed. The electron density in the  $r - z$  plane for this case is shown in Fig. 4.6, where the funnel opening is clearly visible. We again consider a 100 fs Gaussian laser pulse of 70 mJ and vacuum focus of 15  $\mu\text{m}$ . The total energy (solid line) and pulse radius (dotted line) as a function of propagation distance  $z$  are shown in Fig. 4.9. We now observe that nearly all the energy (90%) is confined inside a radius of 20  $\mu\text{m}$  at the beginning of the channel. We also observe an energy loss (solid line with round markers). To understand the reason for the energy loss, we deliberately turned off the plasma wave in the simulation and reran the simulation with the same parameters. The solid line with square markers shows the energy evolution for this latter case. By turning off the plasma wave, we note that energy is essentially conserved. Therefore, the decrease of energy observed in the original simulation is due to excitation of the plasma wave, which is desired.

The time dependence of the on-axis intensity and electron density perturbation at  $z = 0.5 \text{ cm}$  is shown in Fig. 4.10. For comparison, the on-axis intensity with the plasma wave off is also shown. We observe that the on-axis intensity has multiple



peaks even when turning off the plasma wave. This phenomenon is due to a time dependent transformation of the laser pulse shape as it passes through the funnel region where there is further ionization of Helium. This feature is enhanced by the plasma wave. The sharp intensity spikes, when the plasma wave is on, demonstrate the self-modulation instability [14]. The plasma frequency  $\omega_p$  at the channel center is 0.236/fs, which leads to the pulse duration plasma frequency product  $\omega_p\tau = 23.6$ , where  $\tau = 100$  fs is the FWHM of the pulse. At this value of the product self-modulation can occur. In this high density, non-resonant case, a plasma wave is excited, as shown by the electron density perturbation (dashed line). This excited plasma wave, in turn, causes the laser pulse to be axially modulated at the plasma frequency.

The evolution of the on-axis peak intensity is shown in Fig. 4.11. Here the peak intensity as a function of time is found for each axial location. With the plasma wave is on, the averaged on-axis peak intensity inside the channel is  $6.47 \times 10^{17}$  W/cm<sup>2</sup>, which is about 3 times higher than the peak intensity at vacuum focus,  $2.09 \times 10^{17}$  W/cm<sup>2</sup>. To achieve higher laser intensity inside the channel, we need to increase the input power. However, with higher power relativistic self-focusing and cavitation occur. The critical power  $P_{cr}$  for relativistic self-focusing in a uniform plasma with density  $1.75 \times 10^{19}$  cm<sup>-3</sup> is about  $1.71 \times 10^{12}$  W. In the simulations here, the input power is only about 0.41 times of  $P_{cr}$ . However, in the presence of the channel and funnel there is additional focusing of the laser power that

can raise the intensity on axis and lead to cavitation even for powers below the critical power. Our input power is near this limit. We find that if the peak power is raised from  $7.0 \times 10^{11}$  W to  $7.35 \times 10^{11}$  W then cavitation occurs and the fluid model that we are using breaks down. At this point a kinetic treatment should be used to simulate propagation in the channel [15]. The present model is adequate to show that the pulse energy propagates through the funnel and into the channel.

The previous simulations have shown that high coupling efficiency can be achieved for pulse and plasma channels that are realizable in existing experimental settings. The channel electron density are in the range  $2 \times 10^{19}$  cm<sup>-3</sup> on axis. This density is higher than desirable for the given laser pulse because there is excitation of the self-modulation instability due to the large value of  $\omega_p \tau$ . Unfortunately, the present formation scheme does not lend itself to forming channels at lower density due to the strong dependence of the ionization rate on density. A potential to form low density channels exists if gases of atomic clusters are used instead of gas [16]. Clusters efficiently absorb laser energy because the interaction and heating occurs at near solid density.

To explore the coupling and propagation problem in the low density (resonant) regime, we reduce the channel density by 35 times so that the channel center has a density  $5 \times 10^{17}$  cm<sup>-3</sup>, and the radial electron density profile is kept unchanged (the same as what shown in Fig. 4.1). We also assume that in the channel region ( $r \leq 30$   $\mu$ m), Helium is fully ionized so that He<sup>+2</sup> profile is the same as electron

profile. We do not consider the details of the channel formation process in this case. The plasma frequency  $\omega_p$  at the channel center is now  $3.99 \times 10^{-2}$ /fs, which leads to  $\omega_p \tau = 3.99$  for the same laser pulse duration as considered previously. For the given radial profile of electron density, the WKB approximation shows the turning point to be located at  $r = 21.5 \text{ } \mu\text{m}$  for this ideal lower density channel. Therefore, for the injected laser pulse, we keep pulse duration at 100 fs, but choose the vacuum spot size to be  $20 \text{ } \mu\text{m}$ , and increase the pulse energy from 70 mJ to 120 mJ. Figure 4.12 shows the energy and radius for this case. The constancy of the energy and radius curves implies that the laser energy has been efficiently coupled into a single mode of the plasma channel. This is confirmed by surface plots of laser intensity in the  $r - \xi$  plane (here  $\xi = ct - z$ ), which show little variation with axial distance for over 10 Rayleigh lengths of propagation.

Next we consider the variation in the peak intensity on-axis. These are displayed in Fig. 4.13. There are less than  $\pm 10\%$  variations of the on-axis peak intensity, unlike the high density case of Fig. 4.11. The basic eigenmode is flatter than a Gaussian mode. Because the channel density profile is not parabolic, the incident pulse expands initially in the channel, which causes the decrease of the peak intensity. To see that the optimal channel parameters do not depend on the input peak intensity, we vary the input energy. The line with squares shows the case where input energy is doubled. Although the absolute variation increases, the ratio remains about  $\pm 10\%$ . This relation breaks down with the occurrence of cavitation when the input

energy reaches 1.8 J, the corresponding peak power is  $0.3 P_{cr}$ , where the critical power for the relativistic self-focusing for this channel is  $P_{cr} = 6.0 \times 10^{13}$  W.

For gas jet targets, the gas density ramp extends only a short distance (1 ~ 2 mm). It is possible to make a funnel that length in an experiment, such that little neutral gas is left in front of the funnel. The pulse then avoids severe ionization induced refraction prior to entering the channel. With almost all the energy entering the channel, a high intensity can be obtained. However, if more gas present in front of the funnel, the amount of energy that can enter into the channel is reduced. Unlike the gas jet target, where only a limited amount of neutral gas is outside the funnel, there is always uniform neutral gas in front of the funnel for backfill. This is independent of the length of the funnel. Consequently, before the laser pulse can enter the funnel and then the channel, it always encounters uniform neutral gas. To avoid excessive ionization, and consequently severe refraction, the laser intensity prior to entering the funnel should be as low as possible. This requires the laser pulse to focus into the funnel. In the next section, by varying the funnel mouth radius, funnel length, and vacuum focus location, we study what a funnel can do in the case of backfill.

#### 4.4 Backfill Target

Figure 4.14 shows the evolution of the total energy with axial distance and the dependence of the radii through which various percentage of the power pass for a

particular case of a pulse incident on a funnel in backfill. For this simulation, the inner funnel mouth radius is 10 times the inner channel radius, which is fixed to be 30  $\mu\text{m}$ . The funnel entrance is located at  $z = -2.0$  cm. Funnel and channel connect at  $z = 0.0$  cm, which leads to a two centimeter long funnel. The channel has an on-axis electron density of  $5 \times 10^{18} \text{ cm}^{-3}$  with a similar transverse profile as in the previous section. The simulation starts at an axial point ( $z = -4.5$  cm) where no ionization occurs. From that point on, the pulse propagates toward its vacuum focus, which is located at  $z = 0.0$  cm. To reduce the simulation distance, we bring down the pulse energy to 95 mJ, and keep the laser spot size at vacuum focus at 30  $\mu\text{m}$ . The pulse, funnel and channel parameters were selected because they allow for a non negligible amount of energy ( $\sim 40\%$ ) to be coupled into the channel. Shorter funnels resulted in substantially lower coupling efficiencies.

Before the pulse enters the funnel ( $z < -2$  cm), it experiences ionization and refraction. Then the funnel forces the pulse to focus ( $-2 < z < 0$  cm). However, less than 50% of the energy is confined in the funnel and channel, the rest is refracted. We also observe that we lose energy quickly in our simulation due to part of the pulse leaving our simulation box by refraction. The energy loss reduces the on-axis intensity obtained in the channel. For this case, the averaged on-axis peak intensity inside the channel is  $1.14 \times 10^{17} \text{ W/cm}^2$ , which is less than two times the intensity at vacuum focus ( $8.55 \times 10^{16} \text{ W/cm}^2$ ). After 2 cm of propagation only about 20% of the pulse energy is contained in the simulation region.

We next study the effect of the location of the vacuum focus on the intensity inside the channel. The inner funnel mouth radius is fixed at 10 times the inner channel radius, and the funnel length is fixed at two centimeters. The vacuum focus location is shifted from the funnel entrance toward the channel. Figure 4.15 shows the dependence of the averaged on-axis peak intensity inside the channel on the vacuum focus location. The horizontal axis labels the distance of the vacuum focus from the funnel entrance. If the vacuum focus is near the funnel entrance, the laser pulse has a relatively high intensity before entering the funnel, this high intensity causes ionization, which, in turn, refracts the laser pulse and hinders it from entering the funnel. On the other hand, if the vacuum focus is located far inside the channel, the laser spot size at the funnel mouth may be larger than the mouth radius. This results in the deflection of the laser pulse by the inner funnel wall, and hence, the laser pulse cannot be efficiently coupled into the channel. For the parameters used in this figure, the appropriate distance between the vacuum focus and the funnel entrance is two centimeters, which is about 5.7 Rayleigh lengths based on the vacuum spot size of  $30\ \mu\text{m}$ .

The funnel mouth radius doubtlessly affects the coupling efficiency. The dependence of the averaged on-axis peak intensity on the inner funnel mouth radius can be clearly seen in Fig. 4.16, where the inner funnel mouth radius is normalized to the spot size at vacuum focus. The funnel length is fixed to two centimeters, and the vacuum focus is located at the connection of the funnel and the channel. The

intensity obtained inside the channel increases with the funnel mouth radius, and saturates at about  $1.33 \times 10^{17} \text{ W/cm}^2$ .

Finally the curve of the average on-axis peak intensity in the channel versus the funnel length is plotted in Fig. 4.17. To obtain this plot, we fix the funnel mouth radius at 10 times the channel radius. The vacuum focus is always located at the connection of the funnel and the channel. For a fixed funnel mouth radius, if the funnel is too long, the laser pulse deflects on the inner funnel wall. If the funnel is too short, the laser pulse experiences excessive ionization before entering the funnel. Both cases reduce the coupling efficiency of the laser pulse into the funnel-mouthed waveguide. For the above simulation, two-centimeter length yields the best coupling efficiency.

## 4.5 Chapter Summary

We numerically studied the coupling efficiency of laser pulses into funnel-mouthed waveguides. Initially, the waveguide formation code is used, which provides the parameters for formation laser pulses and gas pressure to make an efficient funnel mouthed channel. The simulations show that a funnel can be made in the gas density ramp, and an almost fully ionized channel can be obtained as long as the Helium pressure is more than 550 torr in the center of the gas puff. We then import this funnel and channel information to the code WAKE, and simulate the propagation of a laser pulse with a duration of 100 fs. We find that the funnel in this case provides for 90% efficient coupling of laser energy into the channel. We also

determine that cavitation occurs for pulse energies above 73 mJ. In addition, in a channel of this density a 100 fs, 70 mJ pulse is subject to the self-modulation instability.

We also study propagation in an ideal low density channel. We find that the funnel mouth radius and the location of the gas density ramp are two critical factors that affect the laser pulse as it enters into the channel. For the optimal case, where no neutral gas is in front of the funnel, the funnel mouth radius is two times the spot size at vacuum focus, and an averaged peak intensity of  $9.16 \times 10^{17} \text{ W/cm}^2$  is realized for a 120 mJ, 100 fs pulse. By varying the vacuum spot size, the fundamental mode is excited for this low density channel. For the backfill cases, we cannot eliminate neutral gas in front of the funnel, and we must consider long funnels. To avoid excessive ionization prior to the laser pulse entering the funnel, the vacuum focus should be located several Rayleigh lengths inside the channel from the funnel entrance. Then the laser spot size at the funnel mouth should be several times the spot size at focus. To avoid deflection and refraction at the funnel wall, the funnel mouth radius should be considerably greater than the spot size at vacuum focus. All of these require the funnel to be several centimeters long and the mouth radius to be several centimeters large. These requirements make realization of an effective funnel on backfill unlikely.



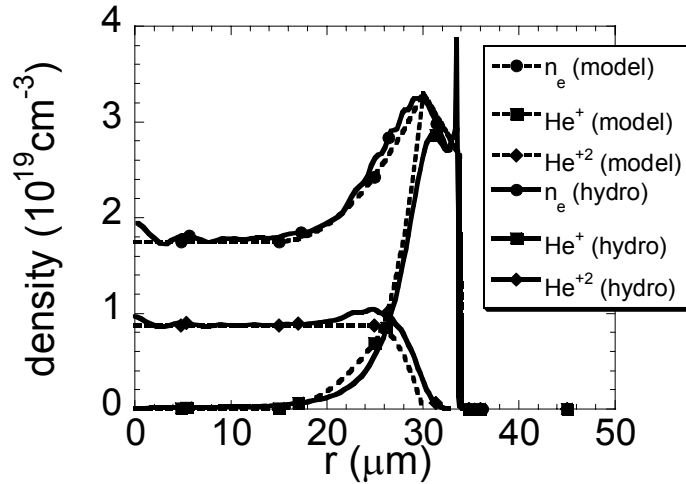


Figure 4.1: Channel density profiles at  $t = 0.7$  ns from the 1D hydrodynamic formation code. The formation pulse is focused into longitudinally uniform 550 torr Helium with duration 150 ps (FWHM) and peak intensity  $1 \times 10^{14}$  W/cm<sup>2</sup> through an axicon at an approach angle of 15°. The solid lines are densities output by the 1D hydrodynamic formation code. The dashed lines are densities used in the propagation simulation. In simulation, two radii determine the electron distribution. From the on-axis to the half of the inner radius (15  $\mu\text{m}$ ), electron density is constant. Then it parabolically increases until reaching the inner radius (30  $\mu\text{m}$ ). Afterward, it linearly decreases to zero at the outer radius (34  $\mu\text{m}$ ). The density of He<sup>+2</sup> is constant up to  $r = 25$   $\mu\text{m}$ , then parabolically decreases to zero at the inner radius. The density of He<sup>+</sup> is extracted by using the particle number conservation law.

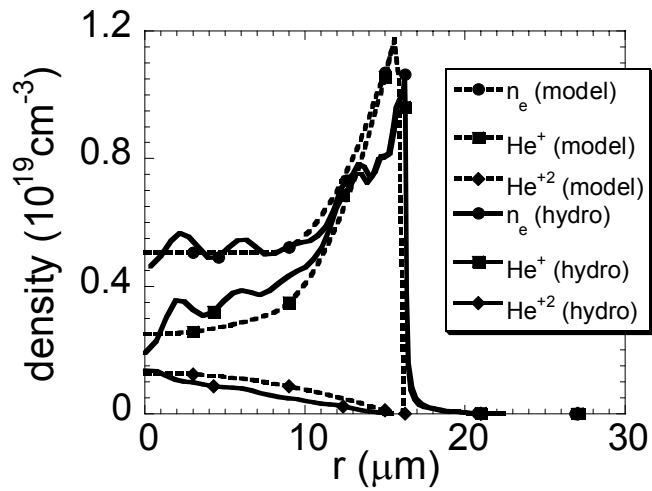


Figure 4.2: Tapered channel profiles produced at the half way of the gas density ramp (275 torr Helium) using the same formation pulse and at the same time as in Fig. 4.1. The solid lines are densities output by the 1D hydrodynamic formation code. The dashed lines are densities used in the propagation simulation.

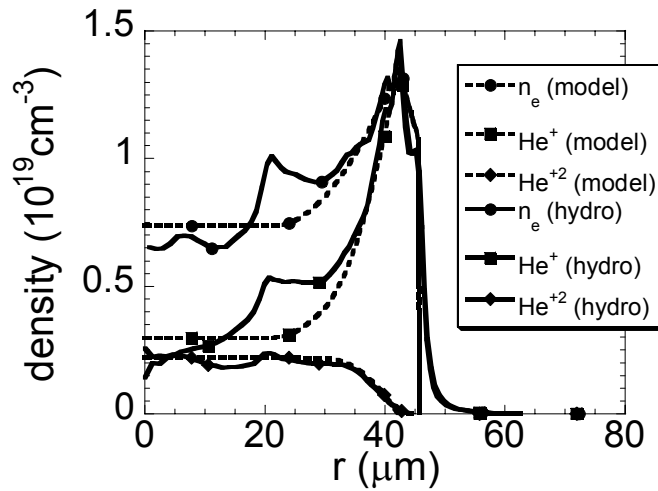


Figure 4.3: The funnel profiles produced at the half way of the gas density ramp (275 torr Helium). The auxiliary funnel formation pulse (Gaussian) leads the channel formation pulse by 0.7 ns with a duration 100 ps and peak intensity  $2.5 \times 10^{14} \text{ W/cm}^2$ . The solid lines are densities output by the 1D hydrodynamic formation code. The dashed lines are densities used in the propagation simulation.

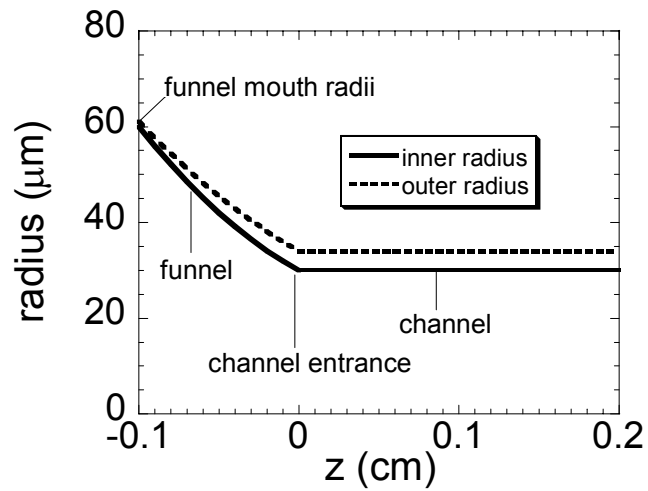


Figure 4.4: Schematic plots of the inner and outer funnel and channel radii. The inner funnel radius parabolically decreases from an inner mouth radius ( $60 \mu\text{m}$ ) at  $z = -0.1 \text{ cm}$  to a constant inner channel radius ( $30 \mu\text{m}$ ) at the channel entrance  $z = 0.0 \text{ cm}$ . This parabolic curve is determined by the inner channel radius at the channel entrance, the inner funnel radius at the half way of the density ramp, and the adjustable inner funnel mouth radius. The outer funnel radius has a similar variation from  $61 \mu\text{m}$  to  $34 \mu\text{m}$ .

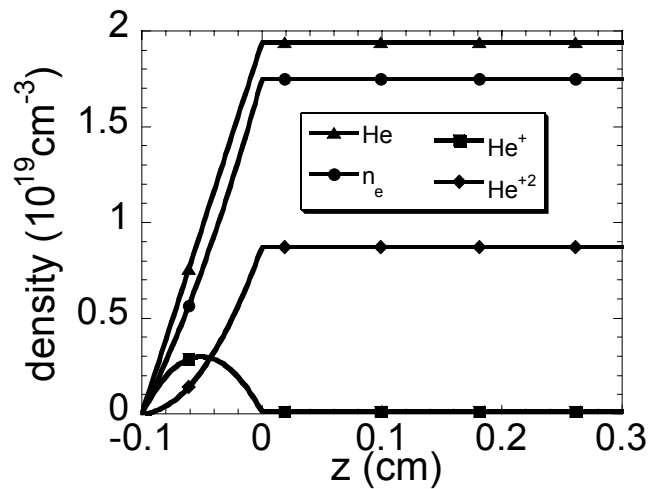


Figure 4.5: On-axis densities by jointing Fig.4.1 and Fig. 4.3. The electron density curve is selected so that it reaches the on-axis density at the half way of the ramp shown in Fig. 4.3, and reaches on-axis density at the channel entrance shown in Fig. 4.1. The  $\text{He}^{+2}$  density parabolically increases from zero to the half way density in Fig. 4.3 and finally reaches the channel  $\text{He}^{+2}$  density in Fig. 4.1. The  $\text{He}^+$  density is extracted by obeying the particle number conservation law. The gas density ramp starts at  $z = -0.1$  cm, ends at  $z = 0.0$  cm with a length of 0.1 cm.

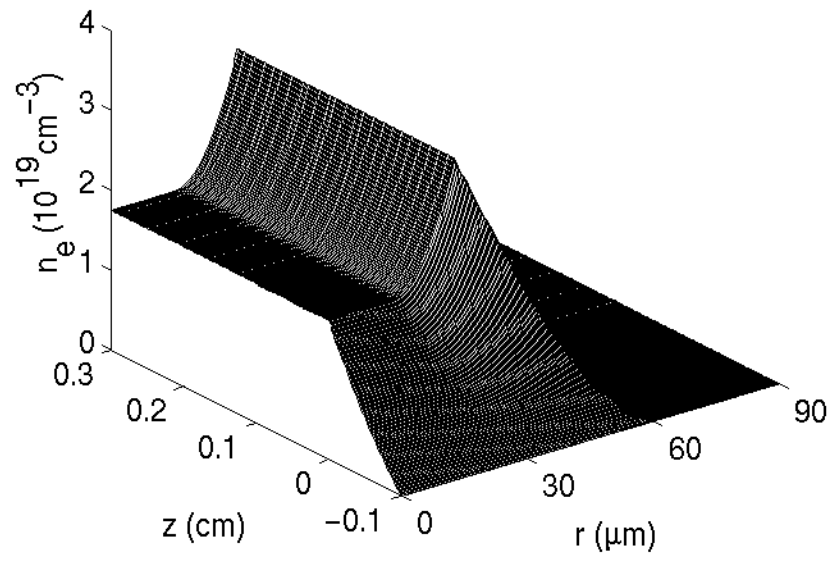


Figure 4.6: Surface plot of a funnel mouthed channel by jointing Fig. 4.1 and 4.3 using method stated in Fig. 4.4 and 4.5.

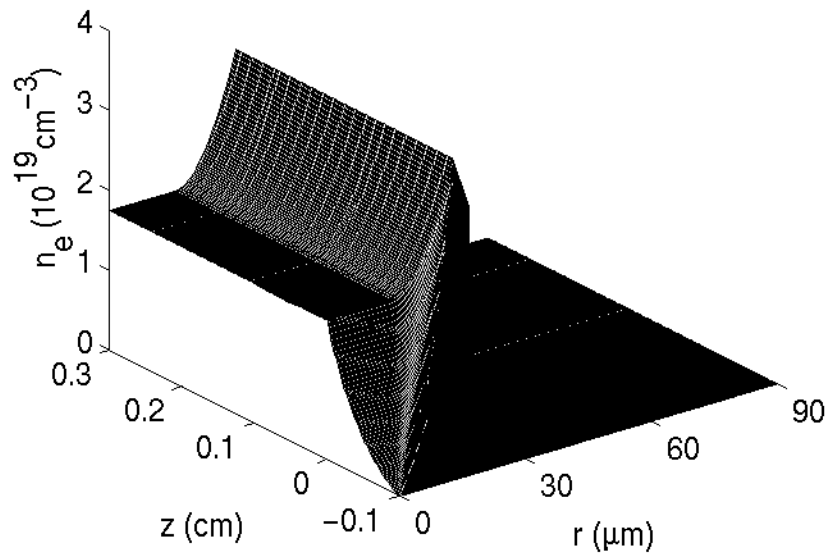


Figure 4.7: Surface plot of a tapered channel by jointing Fig. 4.1 and 4.2 using similar method stated in Fig. 4.4 and 4.5.

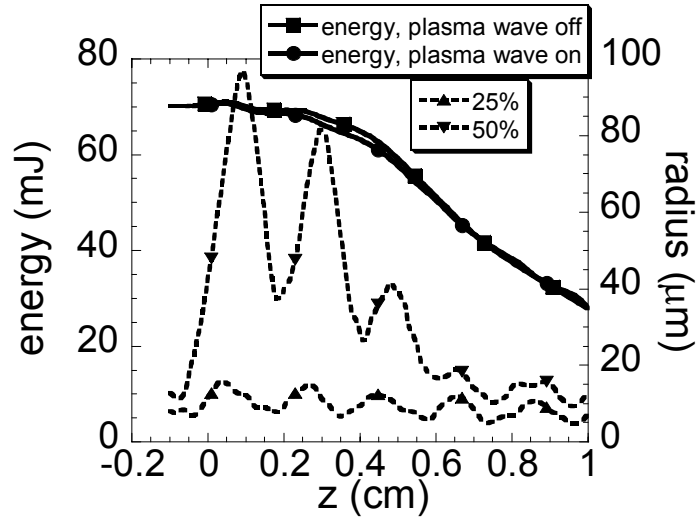


Figure 4.8: The evolution of the total laser energy and radius of percentage energy confined for a laser pulse propagation in the tapered channel shown in Fig. 4.7. The injected pulse has a vacuum spot size of  $15\ \mu\text{m}$ , duration of  $100\ \text{fs}$ , and energy of  $70\ \text{mJ}$ .



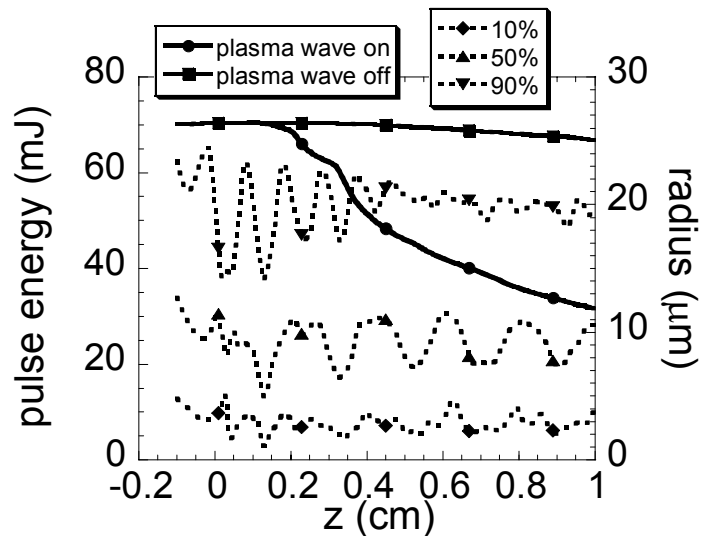


Figure 4.9: The evolution of the total laser energy and radius of percentage energy confined for a laser pulse propagation in the funnel mouthed channel shown in Fig. 4.6. Same injected pulse is used as in Fig. 4.8. The solid line with squares demonstrates the evolution of pulse energy when the plasma wave is turned off. The solid line with circles is that when the plasma wave is on.

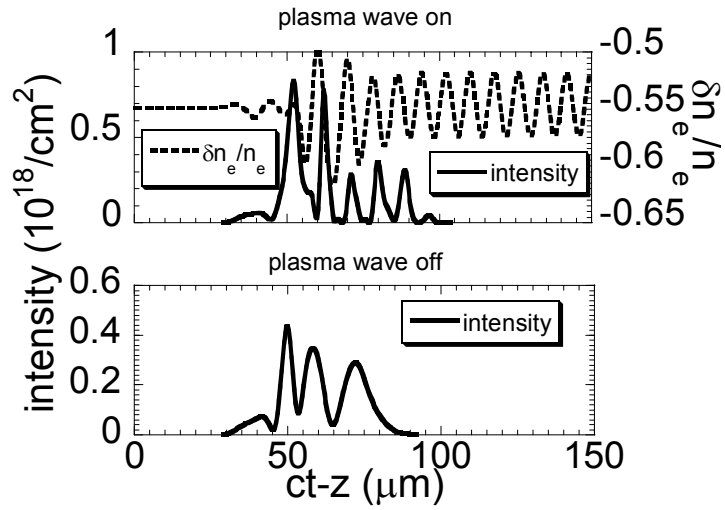


Figure 4.10: The fine dependences of the on-axis intensity and electron density perturbation at  $z = 0.5$  cm . The bottom figure shows the on-axis intensity with the plasma wave off. The upper figure shows both the on-axis intensity (solid line) and electron density perturbation (dashed line).

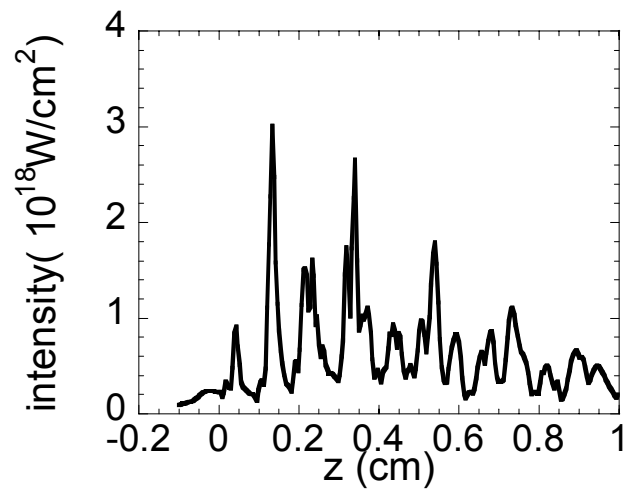


Figure 4.11: The evolution of the on-axis peak intensity in the funnel and channel.

The same channel and laser pulse are used as those in Fig. 4.9.

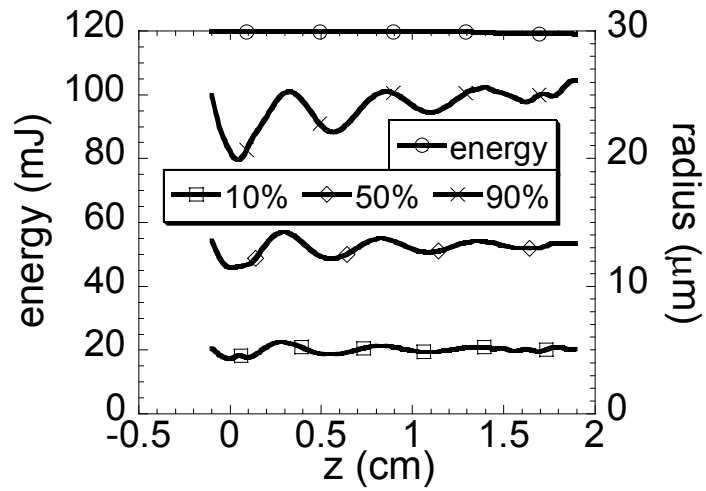


Figure 4.12: The evolution of the total laser energy and radius of percentage energy confined for a laser pulse propagation in an ideal optimal low density channel, which has a similar profile shown in Fig. 4.6, but has a low on-axis electron density of  $5 \times 10^{17} \text{ cm}^{-3}$ . The injected pulse has a vacuum spot size of  $20 \text{ } \mu\text{m}$ , duration of  $100 \text{ fs}$ , and energy of  $120 \text{ mJ}$ .

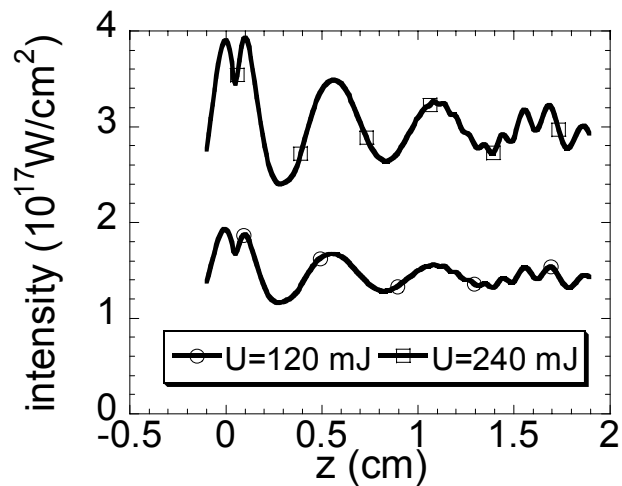


Figure 4.13: The variation in the peak intensity on-axis for the pulse propagation in Fig. 4.12. A  $\pm 10\%$  variation of the on-axis peak intensity is observed (solid line with circles) even when the input energy is doubled (solid line with squares).

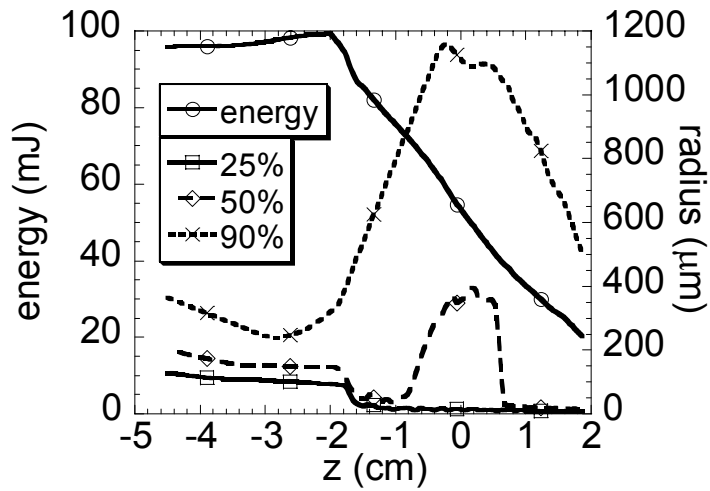


Figure 4.14: The evolution of the total laser energy and radius of percentage energy confined for backfill. The funnel mouth radius is 10 times the channel radius. The laser pump enters the funnel at  $z = -2.0$  cm and the channel at  $z = 0.0$  cm. The vacuum focus is located at channel entrance.

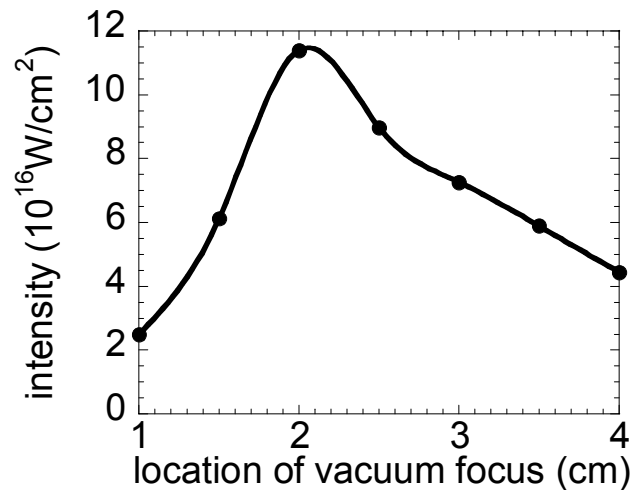


Figure 4.15: The dependence of the averaged on-axis peak intensity inside the channel on the location of the vacuum focus for backfill. The funnel mouth radius is fixed to ten times the channel radius, and funnel length fixed to two centimeters.

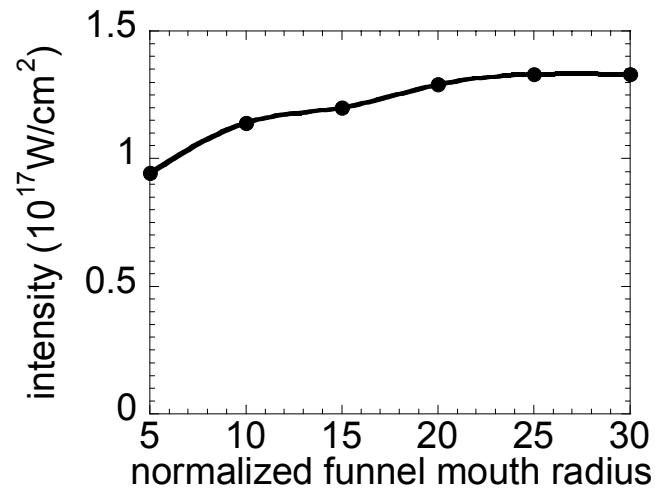


Figure 4.16: The relation between the averaged on-axis peak intensity inside the channel and the normalized funnel mouth radius for backfill. The funnel length is fixed to two centimeters, and the vacuum focus is located at the channel entrance.



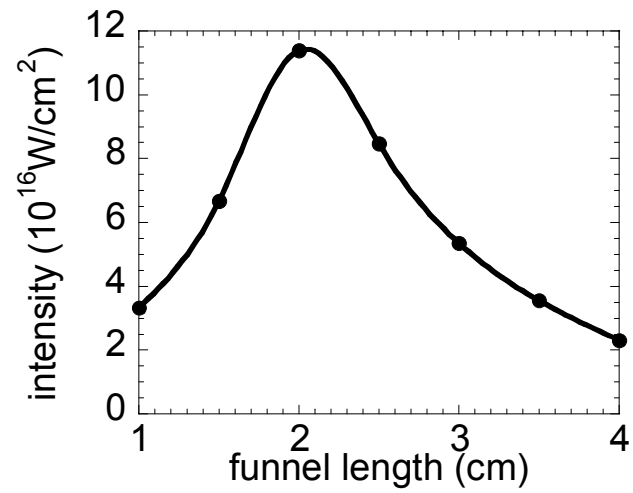


Figure 4.17: Varying of the averaged on-axis peak intensity inside the channel with the funnel length for backfill. The funnel mouth radius is fixed to 10 times the channel radius, the vacuum focus is always located the connection of the funnel and the channel.

## Chapter 5: Conclusion

In this dissertation, we have numerically studied the propagation of high power, initially large spot size, laser pulses in tenuous gases. Propagation is affected by gas ionization, plasma defocusing, nonlinear self-focusing, and group velocity dispersion (GVD). The instantaneous electronic response and time delayed Raman response of the gas are also considered. The propagation properties have been studied at different input power levels. For peak input power near the critical power for nonlinear self-focusing, the pulse behavior is dominated by nonlinear self-focusing and GVD. No plasma or very tenuous plasma is generated in this regime. The nonlinear response of the gas makes the pulse self-focus very quickly, however, it is effectively stopped by GVD. Group velocity dispersion spreads the pulse, lowers the power, and arrests the self-focusing collapse. For moderate input power, plasma is generated and plasma defocusing overwhelms GVD. The peak region of the pulse is refracted due to the high gradient of plasma. The trailing part of the pulse is then trapped just outside the plasma region, and it can be off-axis guided for a remarkably long distance. For higher input power, the pulse behavior is dominated by plasma defocusing. However, part of the pulse is initially trapped in the plasma. Filaments then appear as pulse energy is refracted from the plasma and interference with the part of the laser pulse not trapped occurs. At higher levels of power we can expect three dimensional effects to be important. These will be studied in more detail in the future.

In this dissertation, we have also numerically studied the spectral broadening of laser pulse in tenuous gases. Several factors affect the spectral broadening. Among them are self-phase modulation, nonlinear self-focusing, plasma generation, and group velocity dispersion. In tenuous gases, self-phase modulation, coupled with nonlinear self-focusing, accounts for the near infrared spectrum in the critical power regime. However, if group velocity dispersion arrests the nonlinear self-focusing at an earlier time, spectrum broadening will be limited. At higher input power, plasma generation introduces blue shifted components. The maximum blue shift is determined by both the maximum value of the electron density, and the distance over which the plasma extends

Finally, we numerically studied the coupling efficiency of laser pulses into funnel-mouthed waveguides. The waveguide formation code is used to provide the parameters for formation laser pulses and gas pressure to make an efficient funnel mouthed channel. The simulations show that, as long as the Helium pressure is more than 550 torr in the center of the gas puff, a funnel can be made in the gas density ramp, and an almost fully ionized channel can be obtained. We import this funnel and channel information to the code WAKE, and simulate the propagation of a laser pulse with a duration of 100 fs. We find that the funnel in this case provides for 90% efficient coupling of laser energy into the channel. We also determine that cavitation occurs for pulse energies above 73 mJ. In addition, in a channel of this density a 100 fs, 70 mJ pulse is subject to the self-modulation instability.

For the backfill cases, we cannot eliminate neutral gas in front of the funnel, and we must consider long funnels. To avoid excessive ionization prior to the laser pulse entering the funnel, the vacuum focus should be located several Rayleigh lengths inside the channel from the funnel entrance. Then the laser spot size at the funnel mouth should be several times the spot size at focus. To avoid deflection and refraction at the funnel wall, the funnel mouth radius should be considerably greater than the spot size at vacuum focus. All of these require the funnel to be several centimeters long and the mouth radius to be several centimeters large. These requirements make realization of an effective funnel on backfill unlikely.

## Bibliography:

### Chapter 1:

- [1] J. E. Rothenberg, *Opt. Lett.* **17**, 583 (1992); Q. Feng, J. V. Moloney, A. C. Newell, E. M. Wright, K. Cook, P. K. Kennedy, D. X. Hammer, B. A. Rockwell and C. R. Thompson, *IEEE J. Quantum Electron.* **33**, 127 (1997).
- [2] S. C. Rae and K. Burnett, *Phys. Rev. A* **46**, 1084 (1992).
- [3] W. P. Leemans, C. E. Clayton, W. B. Mori, K. A. Marsh, P. K. Kaw, A. Dyson, C. Joshi, and J. M. Wallace, *Phys. Rev. A* **46**, 1091 (1992); P. Sprangle, E. Esarey and J. Krall, *Phys. Rev. E* **54**, 4211 (1996).
- [4] S. C. Rae, *Opt. Commun.* **97**, 25 (1993); C. D. Decker, D. C. Eder, and R. A. London, *Phys. Plasmas* **3**, 414 (1996).
- [5] T. M. Antonsen, Jr. and P. Mora, *Phys. Fluids B* **5**, 1440 (1993).
- [6] J. K. Ranka, R. W. Schirmer and A. L. Gaeta, *Phys. Rev. Lett.* **77**, 3783 (1996).
- [7] A. Brodeur, C. Y. Chien, F. A. Ilkov, S. L. Chin, O. G. Kosareva and V. P. Kandidov, *Opt. Lett.* **22**, 304 (1997); H. R. Lange, G. Grillon, J.-F. Ripoche, M. A. Franco, B. Lamouroux, B. S. Prade, A. Mysyrowicz, E. T. J. Nibbering and A. Chiron, *Opt. Lett.* **23**, 120 (1998).
- [8] P. Mora and T. M. Antonsen, Jr., *Phys. Plasmas* **4**, 217 (1997).
- [9] M. Mlejnek, E. M. Wright and J. V. Moloney, *Phys. Rev. E* **58**, 4903 (1998).
- [10] M. Mlejnek, E. M. Wright, and J. V. Moloney, *Opt. Lett.* **23**, 382 (1998).
- [11] A. A. Zozulya, *Phys. Rev. Lett.* **82**, 1430 (1999).
- [12] T. Tajima and J. M. Dawson, *Phys. Rev. Lett.* **43**, 267 (1979).

- [13] N. H. Burnett and P. B. Corkum, *J. Opt. Soc. Am. B* **6**, 1195 (1989).
- [14] H. M. Milchberg, C. G. Durfee III, and T. J. McIlrath, *Phys. Rev. Lett.* **75**, 2494 (1995).
- [15] R. R. Alfano and S. L. Shapiro, *Phys. Rev. Lett.* **24**, 584 (1970).
- [16] Y. R. Shen, *The Principles of Nonlinear Optics* (Wiley, NY, 1984).
- [17] L. V. Keldysh, *Sov. Phys. JETP* **20**, 1307 (1965); M. D. Perry, O. L. Landen, A. Szöke, and E. M. Campbell, *Phys. Rev. A* **37**, 747 (1988).
- [18] A. Braun, G. Korn, X. Liu, D. Du, J. Squirer, and G. Mourou, *Opt. Lett.* **20**, 73 (1995); P. Monot, T. Auguste, P. Gibbon, F. Jakober, G. Mainfray, A. Dulieu, M. Loius-Jacquet, G. Malka, and J. L. Miquel, *Phys. Rev. Lett.* **74**, 2953 (1995).
- [19] E. T. J. Nibbering, P. F. Curley, G. Grillon, B. S. Prade, M. A. Franco, F. Salin, and A. Mysyrowicz, *Opt. Lett.* **21**, 62 (1996); B. La Fontaine, F. Vidal, Z. Jiang, C. Y. Chien, D. Comtois, A. Desparois, T. W. Johnston, J.-C. Kieffer, H. Pepin, and H. P. Mercure, *Phys. Plasmas* **6**, 1615 (1999).
- [20] M. Mlejnek, E. M. Wright, and J. V. Maloney, *Opt. Express* **4**, 223 (1999).
- [21] T. M. Antonsen and Z. Bian, *Phys. Rev. Lett.* **82**, 3617 (1999); Z. Bian and T. M. Antonsen, Jr., *Phys. Plasmas* **8**, 3183 (2001).
- [22] C. E. Max, J. Arons, and A. B. Langdon, *Phys. Rev. Lett.* **33**, 209(1974); P. Sprangle, E. Esarey, and B. Hafizi, *Phys. Rev. Lett.* **79**, 1046(1997); P. Sprangle, B. Hafizi, and J. R. Penano, *Phys. Rev. E* **61**, 4381 (2000).
- [23] A. Penzkofer, A. Laubereau, and W. Kaiser, *Phys. Rev. Lett.* **31**, 863 (1973); A. Penzkofer, A. Seilmeier, and W. Kaiser, *Opt. Commun.* **14**, 363 (1975); A. Penzkofer

and W. Kaiser, *Opt. Quantum Electron.* **9**, 315 (1977); M. Wittman and A. Penzkofer, *Opt. Commun.* **126**, 308 (1996).

[24] N. Bleombergen, *Opt. Commun.* **8**, 285 (1973); E. Yablonovitch, *Phys. Rev. A* **10**, 1888 (1974); W. L. Smith, P. Liu, and N. Bloembergen, *Phys. Rev. A* **15**, 2369 (1977).

[25] R. L. Fork, C. V. Shank, C. Hirlimann, R. Yen, *Opt. Lett.* **8**, 1 (1983).

[26] G. Yang and Y. R. Shen, *Opt. Lett.* **9**, 510 (1984).

[27] P. B. Corkum, C. Rolland and T. Srinivasan-Rao, *Phys. Rev. Lett.* **57**, 2268 (1986); P. B. Corkum, C. Rolland, *IEEE J. Quantum Electron.* **25**, 2634 (1989).

[28] J. H. Glowia, J. Misewich and P. P. Sorokin, *J. Opt. Soc. Am. B* **3**, 1573 (1986).

[29] F. A. Ilkov, L. Sh. Ilkova and S. L. Chin, *Opt. Lett.* **18**, 681 (1993).

[30] A. Brodeur and S. L. Chin, *J. Opt. Soc. Am. B* **16**, 637 (1999).

[31] R. R. Alfano, ed., *The Supercontinuum Laser Source* (Springer-Verlag, New York, 1989).

[32] K. R. Wilson and V. V. Yakovlev, *J. Opt. Soc. Am. B* **14**, 444 (1997).

[33] E. N. Glezer, Y. Siegal, L. Huang, and E. Mazur, *Phys. Rev. B* **51**, 6959 (1995).

[34] W. L. Smith, P. Liu, and N. Bloembergen, *Phys. Rev. A* **15**, 2396 (1977).

[35] T. Tajima and J. M. Dawson, *Phys. Rev. Lett.* **43**, 267 (1979).

[36] E. Esarey, P. Sprangle, J. Krall, and A. Ting, *IEEE Trans. Plasma Sci.* **24**, 252 (1996).

[37] P. Chen, J. J. Su, J. M. Dawson, K. L. F. Bane, and P. B. Wilson, *Phys. Rev. Lett.* **56**, 1252 (1986); J. B. Rosenzweig, D. B. Cline, B. Cole, H. Figueroa, W. Gai, R. Konecny, J. Norem, P. Schoessow, and J. Simpson, *Phys. Rev. Lett.* **61**, 98 (1988);

J. Krall, G. Joyce, and E. Esarey, *Phys. Rev. A* **44**, 6854 (1991); J. Krall and G. Joyce, *Phys. Plasmas* **2**, 1326 (1995).

[38] C. Joshi, W. B. Mori, T. Katsouleas, J. M. Dawson, J. M. Kindel, and D. W. Forslund, *Nature* **311**, 525 (1984); C. E. Clayton, K. A. Marsh, A. Dyson, M. Everett, A. Lal, W. P. Leemans, R. Williams, and J. Joshi, *Phys. Rev. Lett.* **70**, 37 (1993); N. A. Ebrahim, *J. Appl. Phys.* **76**, 7645 (1994); M. J. Everett, A. Lal, D. Gordon, C. E. Clayton, W. B. Mori, T. W. Johnston, and C. Joshi, *Phys. Rev. Lett.* **74**, 2236 (1995).

[39] P. Sprangle, E. Esarey, A. Ting, and G. Joyce, *Phys. Rev. Lett.* **53**, 2146 (1988); P. Sprangle, E. Esarey, J. Krall, and G. Joyce, *Phys. Rev. Lett.* **69**, 2200 (1992).

[40] D. Strickland and G. Mourou, *Opt. Commun.* **56**, 219 (1985); P. Maine, D. Strickland, P. Bado, M. Pessot, and G. Mourou, *IEEE J. Quantum Electron.* **QE-24**, 398 (1988).

[41] Y. Erlich, C. Cohen, A. Zigler, J. Krall, P. Sprangle, and E. Esarey, *Phys. Rev. Lett.* **77**, 4186 (1996).

[42] S. Jackel, S. Burris, J. Grun, A. Ting, C. Manka, K. Evans, and J. Kosakowskii, *Opt. Lett.* **20**, 1086 (1995).

[43] C. G. Durfee, and H. M. Milchberg, *Phys. Rev. Lett.* **71**, 2409 (1993); C. G. Durfee, J. Lynch, and H. M. Milchberg, *Phys. Rev. E* **51**, 2368 (1995).

[44] S. P. Nikitin, T. M. Antonsen, T. R. Clark, Y. Li, and H. M. Milchberg, *Opt. Lett.* **22**, 1787 (1997).

[45] E. W. Gaul, S. P. Le Blanc, A. R. Rundquist, R. Zgadzaj, H. Langhoff, and M. C. Downer, *Appl. Phys. Lett.* **77**, 4112 (2000).



- [46] S. P. Nikitin, I. Alexeev, J. Fan, and H. M. Milchberg, *Phys. Rev. E* **59**, R3839 (1999).
- [47] P. Volfbeyn, E. Esarey, and W. P. Leemans, *Phys. Plasma* **6**, 2269 (1999).
- [48] K. Y. Kim, I. Alexeev, J. Fan, E. Parra, and H. M. Milchberg, *AIP Conference Proceedings* **647**, 646 (2002).
- [49] H. M. Milchberg, S. J. McNaught, and E. Parra, *Phys. Rev. E* **64**, 056402 (2001).

## Chapter 2:

- [1] J. E. Rothenberg, *Opt. Lett.* **17**, 583 (1992); Q. Feng, J. V. Moloney, A. C. Newell, E. M. Wright, K. Cook, P. K. Kennedy, D. X. Hammer, B. A. Rockwell and C. R. Thompson, *IEEE J. Quantum Electron.* **33**, 127 (1997).
- [2] S. C. Rae and K. Burnett, *Phys. Rev. A* **46**, 1084 (1992).
- [3] W. P. Leemans, C. E. Clayton, W. B. Mori, K. A. Marsh, P. K. Kaw, A. Dyson, C. Joshi, and J. M. Wallace, *Phys. Rev. A* **46**, 1091 (1992); P. Sprangle, E. Esarey and J. Krall, *Phys. Rev. E* **54**, 4211 (1996); C. D. Decker, D. C. Eder, and R. A. London, *Phys. Plasmas* **3**, 414 (1996).
- [4] T. M. Antonsen, Jr. and P. Mora, *Phys. Fluids B* **5**, 1440 (1993).
- [5] J. K. Ranka, R. W. Schirmer and A. L. Gaeta, *Phys. Rev. Lett.* **77**, 3783 (1996).
- [6] A. Brodeur, C. Y. Chien, F. A. Ilkov, S. L. Chin, O. G. Kosareva and V. P. Kandidov, *Opt. Lett.* **22**, 304 (1997); H. R. Lange, G. Grillon, J.-F. Ripoche, M. A. Franco, B. Lamouroux, B. S. Prade, A. Mysyrowicz, E. T. J. Nibbering and A. Chiron, *Opt. Lett.* **23**, 120 (1998).
- [7] P. Mora and T. M. Antonsen, Jr., *Phys. Plasmas* **4**, 217 (1997).

- [8] M. Mlejnek, E. M. Wright and J. V. Moloney, Phys. Rev. E **58**, 4903 (1998).
- [9] M. Mlejnek, E. M. Wright, and J. V. Moloney, Opt. Lett. **23**, 382 (1998).
- [10] A. A. Zozulya, Phys. Rev. Lett. **82**, 1430 (1999).
- [11] T. Tajima and J. M. Dawson, Phys. Rev. Lett. **43**, 267 (1979).
- [12] N. H. Burnett and P. B. Corkum, J. Opt. Soc. Am. B **6**, 1195 (1989).
- [13] H. M. Milchberg, C. G. Durfee III, and T. J. McIlrath, Phys. Rev. Lett. **75**, 2494 (1995).
- [14] Y. R. Shen, *The Principles of Nonlinear Optics* (Wiley, NY, 1984).
- [15] A. Braun, G. Korn, X. Liu, D. Du, J. Squirer, and G. Mourou, Opt. Lett. **20**, 73 (1995); P. Monot, T. Auguste, P. Gibbon, F. Jakober, G. Mainfray, A. Dulieu, M. Loius-Jacquet, G. Malka, and J. L. Miquel, Phys. Rev. Lett. **74**, 2953 (1995).
- [16] M. Mlejnek, E. M. Wright, and J. V. Maloney, Opt. Express **4**, 223 (1999).
- [17] A. Brodeur and S. L. Chin, J. Opt. Sci. Am. B **16**, 637 (1999).
- [18] Z. Bian and T. M. Antonsen, Jr., Phys. Plasmas **8**, 3183 (2001).
- [19] L. V. Keldysh, Sov. Phys. JETP **20**, 1307 (1965).
- [20] M. D. Perry, O. L. Landen, A. Szöke, and E. M. Campbell, Phys. Rev. A **37**, 747 (1988).
- [21] R. D. Richtmyer and K. W. Morton, in *Interscience Tracts in Pure and Applied Mathematics*, edited by L. Bers, R. Courant and J. J. Stoker, *Number 4--Difference Methods for Initial-value Problems* (Wiley, NY, 1967).
- [22] S. C. Wilks, J. M. Dawson, and W. B. Mori, Phys. Rev. Lett. **61**, 337 (1988).
- [23] R. W. Hellwarth, A. Owyong and N. George, Phys. Rev. A **4**, 2342 (1971).

[24] M. Mlejnek, M. Kolesik, J. V. Moloney and E. M. Wright, Phys. Rev. Lett. **83**, 2938 (1999).

### Chapter 3:

[1] R. R. Alfano and S. L. Shapiro, Phys. Rev. Lett. **24**, 584 (1970); R. R. Alfano, ed., *The Supercontinuum Laser Source* (Springer-Verlag, New York, 1989).

[2] A. Penzkofer, A. Laubereau, and W. Kaiser, Phys. Rev. Lett. **31**, 863 (1973); A. Penzkofer, A. Seilmeier, and W. Kaiser, Opt. Commun. **14**, 363 (1975); A. Penzkofer and W. Kaiser, Opt. Quantum Electron. **9**, 315 (1977); M. Wittman and A. Penzkofer, Opt. Commun. **126**, 308 (1996).

[3] N. Bloembergen, Opt. Commun. **8**, 285 (1973); E. Yablonovitch, Phys. Rev. A **10**, 1888 (1974); W. L. Smith, P. Liu, and N. Bloembergen, Phys. Rev. A **15**, 2369 (1977).

[4] R. L. Fork, C. V. Shank, C. Hirlimann, R. Yen, Opt. Lett. **8**, 1 (1983).

[5] G. Yang and Y. R. Shen, Opt. Lett. **9**, 510 (1984).

[6] P. B. Corkum, C. Rolland and T. Srinivasan-Rao, Phys. Rev. Lett. **57**, 2268 (1986); P. B. Corkum, C. Rolland, IEEE J. Quantum Electron. **25**, 2634 (1989).

[7] J. H. Glowina, J. Misewich and P. P. Sorokin, J. Opt. Soc. Am. B **3**, 1573 (1986).

[8] S. C. Rae and K. Burnett, Phys. Rev. A **46**, 1084 (1992).

[9] F. A. Ilkov, L. Sh. Ilkova and S. L. Chin, Opt. Lett. **18**, 681 (1993).

[10] A. Brodeur and S. L. Chin, J. Opt. Soc. Am. B **16**, 637 (1999).

[11] K. R. Wilson and V. V. Yakovlev, J. Opt. Soc. Am. B **14**, 444 (1997).

- [12] J. H. Marburger and W. G. Wagner, IEEE J. Quantum Electron. **QE-3**, 415 (1967).
- [13] P. Mora and T. M. Antonsen, Jr., Phys. Plasmas **4**, 217 (1997).
- [14] L. V. Keldysh, Sov. Phys. JETP **20**, 1307 (1965); M. D. Perry, O. L. Landen, A. Szoke, and E. M. Campbell, Phys. Rev. A **37**, 747 (1988).
- [15] J. Wu and T. M. Antonsen, Jr., Phys. Plasmas **10**, 2254 (2003).
- [16] Y. R. Shen, *The Principles of Nonlinear Optics* (Wiley, New York, 1984).
- [17] G. P. Agrawal, *Nonlinear Fiber Optics*, 2nd ed. (Academic, New York, 1994).

#### Chapter 4:

- [1] H. M. Milchberg, C. G. Durfee III, and J. Lynch, J. Opt. Soc. Am. B **12**, 731 (1995);
- [2] T. Tajima and J. M. Dawson, Phys. Rev. Lett. **43**, 267 (1979); P. Sprangle, E. Esarey, A. Ting, and G. Joyce, Appl. Phys. Lett. **53**, 2146 (1988).
- [3] Y. Erlich, C. Cohen, A. Zigler, J. Krall, P. Sprangle, and E. Esarey, Phys. Rev. Lett. **77**, 4186 (1996).
- [4] S. Jackel, S. Burris, J. Grun, A. Ting, C. Manka, K. Evans, and J. Kosakowski, Opt. Lett. **20**, 1086 (1995).
- [5] C. G. Durfee, and H. M. Milchberg, Phys. Rev. Lett. **71**, 2409 (1993); C. G. Durfee, J. Lynch, and H. M. Milchberg, Phys. Rev. E **51**, 2368 (1995).
- [6] S. P. Nikitin, T. M. Antonsen, Jr., T. R. Clark, Yuelin Li, and H. M. Milchberg, Opt. Lett. **22**, 1787 (1997).

- [7] E. W. Gaul, S. P. Le Blanc, A. R. Rundquist, R. Zgadzaj, H. Langhoff, and M. C. Downer, *Appl. Phys. Lett.* **77**, 4112 (2000).
- [8] S. P. Nikitin, I. Alexeev, J. Fan, and H. M. Milchberg, *Phys. Rev. E* **59**, R3839 (1999).
- [9] P. Volfbeyn, E. Esarey, and W. P. Leemans, *Phys. Plasma* **6**, 2269 (1999).
- [10] K. Y. Kim, I. Alexeev, J. Fan, E. Parra, and H. M. Milchberg, *AIP Conference Proceedings* **647**, 646 (2002).
- [11] J. Wu and T. M. Antonsen, Jr., *Phys. Plasmas* **10**, 2254 (2003).
- [12] P. Mora, and T. M. Antonsen, Jr., *Phys. Plasmas* **4**, 217 (1997).
- [13] H. M. Milchberg, S. J. McNaught, and E. Parra, *Phys. Rev. E* **64**, 056402 (2001).
- [14] E. Esarey, J. Krall, and P. Sprangle, *Phys. Rev. Lett.* **72**, 2887 (1994); N. E. Andreev, V. I. Kirsanov, and L. M. Gorbunov, *Phys. Plasmas* **2**, 2573 (1995); P. Sprangle, B. Hafizi, and J. R. Penano, *Phys. Rev. E* **61**, 4381 (2000).
- [15] P. Mora and T. M. Antonsen, Jr., *Phys. Rev. E* **53**, R2068 (1996).
- [16] T. Taguchi, T. M. Antonsen, Jr., H. M. Milchberg, *Phys. Rev. Lett.* **92**, 205003 (2004); K. Y. Kim, I. Alexeev, V. Kumarappan, E. Parra, T. M. Antonsen, Jr., T. Taguchi, A. Gupta, H. M. Milchberg, *Phys. Plasmas* **11**, 2882 (2004).